Gas-phase kinetic study of soot precursors with variable hydrogen contents using a shock tube with high-repetition-rate time-of-flight mass spectrometry

Von der Fakultät für Ingenieurwissenschaften,
Abteilung Maschinenbau und Verfahrenstechnik
der

Universität Duisburg-Essen

zur Erlangung des akademischen Grades
eines

Doktors der Ingenieurwissenschaften

Dr.-Ing.

genehmigte Dissertation

von

Mohammad Aghsaee

aus

Teheran, Iran

Gutachter: Prof. Dr. rer. nat. Christof Schulz

Prof. Dr. rer. nat. Ravi Fernandes

Tag der mündlichen Prüfung: 25.1.2016

Table of Contents

Abstract

Carbon nanoparticles play an important role both as combustion-generated pollutants and important industrial products. The detailed understanding of carbon particle formation is of high interest for both, the suppression of unwanted soot emissions and the generation of tailored highly-specific nanomaterials. Soot formation in hydrocarbon combustion is to a large extent determined by the effect of hydrogen and also, the properties of soot are strongly influenced by the presence of hydrogen, most obviously seen by comparing "conventional" soot with soot formed in hydrogen-free systems. Quantitative knowledge about the influence of hydrogen, however, is missing despite its crucial impact on soot formation pathways.

In the present study, pyrolysis of carbon tetrachloride (CCl_4), carbon suboxide (C_3O_2), and acetylene (C_2H_2) was investigated in the gas phase before the inception of the soot particles. Previous studies were focused on the final soot product but in the current study the kinetics of pre-soot species was studied to determine the underlying chemical reaction channels that are relevant for soot formation. This study was based on experiments in a shock tube coupled to a high-repetition rate time-of-flight mass spectrometer (TOF-MS) and supported with detailed kinetics modeling. The TOF-MS enables simultaneous time-resolved concentration measurements of multiple species after initiation of the reaction through the shock wave and therefore is a powerful tool to unravel the gas-phase chemistry of complex hydrocarbons systems.

The experimental data were compared to simulations using selected reaction mechanisms. In CCl_4 pyrolysis, it was identified that the reaction sequence $CCl_4 \rightarrow CCl_2 \rightarrow C_2Cl_2 \rightarrow$ chlorinated polyynes $\rightarrow C_n$ is the main route towards the formation of carbonaceous material. During the pyrolysis of carbon suboxide (C_3O_2) an increase in the C/C_2 concentration ratio with temperature was observed which provides evidence for the importance of the C_2 dimer for the growth of larger carbon clusters. In the thermal decomposition of acetylene, besides C_2H_2, higher polyacetylenes ($C_{2n}H_2$, n = 2–4) were detected as products. Measured concentration-time profiles were compared with simulated ones and reasonable agreement was found between the experiments and the model predictions for C_2H_2, C_4H_2, C_6H_2, and C_8H_2. Addition of H_2 led to a depletion of the important precursors for particle formation.

Kurzfassung

Kohlenstoff-Nanopartikel entstehen nicht nur als unerwünschte Nebenprodukte von Verbrennungsprozessen, sie werden auch gezielt im Industriemaßstab hergestellt und gehören zu den Schlüsselmaterialen des 21. Jahrhunderts. Daher ist ein detailliertes Verständnis der Kohlenstoff-Partikelbildung nicht nur für Herstellung maßgeschneiderter Nanomaterialien von hohem Interesse, sondern auch bei der Verringerung der Rußemission bei der Verbrennung fossiler Brennstoffe. Die Bildung von Ruß bei der Verbrennung kohlenwasserstoffhaltiger Brennstoffe und dessen Eigenschaften werden zu einem erheblichen Maße vom anwesenden Wasserstoff beeinflusst. Dies lässt sich besonders gut beim Vergleich der konventionellen Verbrennung mit Wasserstoff und bei der wasserstofffreien Verbrennung beobachten. Trotz des enormen Einflusses von Wasserstoff auf die Rußbildung sind bisher nur wenige quantitative Daten verfügbar.

In der vorliegenden Arbeit wurde die Pyrolyse von Tetrachlorkohlenstoff (CCl_4), Kohlenstoffsuboxid (C_3O_2) und Ethin (C_2H_2) in der Gasphase, vor der Entstehung der Rußpartikel, untersucht. Frühere Studien konzentrierten sich vor allem auf die Untersuchung des entstehenden Rußes, daher liegt der Fokus dieser Arbeit auf der Kinetik der Zwischenprodukte, mit dem Ziel die dominierenden chemischen Reaktionskanäle zu bestimmen. Die Experimente wurden an einem Stoßwellenrohr, das mit einem hoch repetitiven Flugzeitmassenspektrometer (HRR-TOF-MS) gekoppelt ist, durchgeführt und mit Simulationen auf Basis von detaillierten Reaktionsmechanismen verglichen. Das HRR-TOF-MS ermöglicht die simultane, zeitaufgelöste Konzentrationsmessung mehrerer Spezies nach Beginn der Reaktion, die durch die Stoßwelle initiiert wird. Somit ist es ein leistungsfähiges Werkzeug zur Untersuchung der Gasphasenchemie komplexer kohlenwasserstoffhaltiger Systeme.

Die experimentell gewonnen Daten wurden mit den Simulationen ausgewählter Reaktionsmechanismen verglichen. Bei der CCl_4-Pyrolyse wurde festgestellt, dass die Reaktionsfolge $CCl_4 \rightarrow CCl_2 \rightarrow C_2Cl_2 \rightarrow$ chlorierte Polyine $\rightarrow C_n$ der bedeutendste Reaktionspfad bei der Bildung kohlenstoffhaltiger Materialien ist. Während der Pyrolyse von Kohlensuboxid konnte eine Erhöhung des C/C_2-Konzentrationsverhältnisses in Abhängigkeit von der Temperatur beobachtet werden. Diese Beobachtung beweist die Bedeutung des C_2-Dimers für das Wachstum größerer Kohlenstoff-Cluster. Beim thermischen Zerfall von C_2H_2, wurden neben C_2H_2 selbst auch höhere Polyacetylene ($C_{2n}H_2$, n = 2–4) als Produkte nachgewiesen. Die Konzentrations-Zeit-Profile wurden mit Simulationen für C_2H_2, C_4H_2, C_6H_2 und C_8H_2 verglichen. Die Zugabe von H_2 führte zu einer Verarmung an Prekursoren für das Partikelwachstum.

Symbols and abbreviations

Symbols

A_{Nozzle}	*Area of the nozzle*
A	Pre-exponential factor
$\bar{c}$	Mean molecule velocity
c_x	Concentration of species x
c_p	Heat capacity at constant pressure
c_v	Heat capacity at constant volume
d	Length of the flight tube
D	Nozzle diameter
D_s	Skimmer diameter
e	Electronic charge
E_a	Activation energy
E_K	Kinetic energy
E_P	Potential energy
f	Frequency of the ionization
h	Enthalpy
h	Planck constant
I	Electrical current
I_x	Intensity of species x
k	Rate coefficient
Kn	Knudsen number
m	Mass
m_e	Mass of electron
$\dot{m}$	Mass flow
M	Mach number
M	Molar mass
M_S	Local Mach number at skimmer tip
N	Particle number
N_A	Avogadro number
p	Pressure

p_b	Pressure in expansion field
p_x	Partial pressure of species x
R	Universal gas constant
R_{gas}	Radius of collision partners
t	Time
T	Temperature
u	Velocity
U	Electric potential difference (Voltage)
v	Velocity
v_{cs}	Contact surface velocity
v_{iw}	Incident shock wave velocity
V	Acceleration voltage
V	Volume
W	Average molecular weight
x	Distance
x_e	Freezing distance
z	Number of electron charges

Greek symbols

α	Liepmann factor
δ	Length of thermal boundary layer
γ	Heat capacity ratio
κ	Thermal diffusivity
Λ	Mean free path between two collisions
λ	Wave length
μ	Dynamic viscosity
ρ	Density
τ	Ignition delay time

Abbreviations and acronyms

ARAS	Atomic resonance absorption spectroscopy
CI	Chemical ionization
EI	Electron impact

FI	Field ionization
HACA	Hydrogen abstraction, acetylene addition
HRR-TOF-MS	High repetition-rate time-of-flight mass spectrometer
LIF	Laser-induced fluorescence
LII	Laser induced incandescence
MALDI	Matrix-assisted laser desorption ionization
MBS	Molecular-beam sampling
MCP	Microchannel plate
MS	Mass spectrometry
PAH	Polycyclic aromatic hydrocarbons
RRKM	Rice-Ramsperger-Kassel-Marcus
SACM	Statistical adiabatic channel model
TBL	Thermal boundary layer
TEM	Transmission electron microscope
TOF	Time of flight

Acknowledgements

I would like to express my gratitude to my dearest supervisor Prof. Dr. Christof Schulz for giving me the opportunity to work in his group and finish my dissertation. I would like to thank him for his warm encouragement, thoughtful guidance and countless help and support to make this thesis possible. He is a true source of knowledge and an excellent role model for my future.

I would like to thank my current and former group leaders Dr. Mustapha Fikri, Dr. Steffen H. Dürrstein, and Dr. Oliver Welz for their instructions, continuous supports, sharing their experience and also providing good suggestions during my work in IVG. Their expertise, genuine advices and positive attitudes are one of a kind.

Many thanks go to my colleague Siavash Zabeti with whom we shared the office during the last years and we had so many interesting discussions about shock tube and chemical kinetics. I want to acknowledge my colleague Bo Shu for assisting me in acetylene experiments. Further I want to acknowledge my current and former colleagues in kinetics group: Dr. Heidi Böhm, Dr. Metehan Bozkurt, Michaela Hartmann, Dr. Jürgen Herzler, Philip Niegemann, and Paul Sela. Thanks for the nice working atmosphere and the fruitful discussions in many scientific and non-scientific problems.

I deeply thank Dr. Ralf Starke for organizational and personal guidance. I would like to acknowledge Dieter Hermanns for his technical assistance, safety seminars and also non-scientific discussions. I humbly acknowledge Ludger Jerig for his engagement in doing lots of construction and modification on my shock tube and for vacuum seminars. I sincerely thank our outstanding laboratory and workshop assistants: Birgit Nelius, Natascha Schlösser, Beate Endres, and Jörg Albrecht for their continuously kind supports in the lab. I deeply thank Barbara Nota and Barbara Graf for managing the administrative tasks.

I would like to express my grateful appreciations to whole IVG for the prosperous collaboration. It was a pleasure for me to work with you in a very friendly and familiar atmosphere.

I would like to take this opportunity to thank my parents Mohsen and Rita, my brother Dr. Payam Aghsaee and my lovely sister Roya for loving and supporting me endlessly. I am grateful to them for their confidence in me and encouraging me to push myself beyond the limits.

Last but not least, I would like to thank my wife Maneli, for her love, support, motivation and patience. She has stood beside me from the very beginning of my time at IVG, and I owe more smiles, laughs, joy, and good memories to her than to anyone else.

1. Introduction

Soot formation has always been of great interest for combustion researchers. In flames, soot contributes to light emission and radiative heat transfer. Flames have also been used for manufacturing carbon black for a long time [1]. In the early 1970s negative health effects of soot were recognized and soot was categorized as an unwanted pollutant formed in combustion. It was understood that soot particles can adsorb toxic polycyclic aromatic hydrocarbons (PAH) on to their surfaces [2].

Under stoichiometric conditions the combustion of hydrocarbons leads mainly to carbon dioxide and water. But in practice, combustion processes such as in internal combustion engines often deviate from stoichiometric conditions. When there is not enough oxygen to fully convert the fuel, products of incomplete combustion such as carbon monoxide, hydrogen, partially-oxidized hydrocarbons and soot are produced [3]. Even if there is globally enough oxygen, inhomogeneity, such as locally rich areas, can cause incomplete combustion and therefore soot formation.

The understanding of soot formation on the basis of chemical kinetics and modeling of these processes is of crucial interest in optimization of the above mentioned issues. It is clear that the conversion of hydrocarbons with few carbon atoms into carbonaceous agglomerates with millions of carbon atoms is a complicated process. The gas-phase to solid-phase transition leads to particles with nonuniform chemical and physical structure. Soot formation includes various chemical and physical processes. The rate determining reaction in soot formation is the formation of first aromatic rings. By further growth of these aromatic rings, polycyclic aromatic hydrocarbons (PAH) are formed. From a certain size of the PAHs the nucleation of soot particles starts and the soot particles continue to grow through surface reactions. The particle formation continues with the coagulation and agglomeration [3]. Figure 1.1 gives an overview of the conversion of burning hydrocarbon fuels to polycyclic aromatics hydrocarbons (PAHs) and soot.

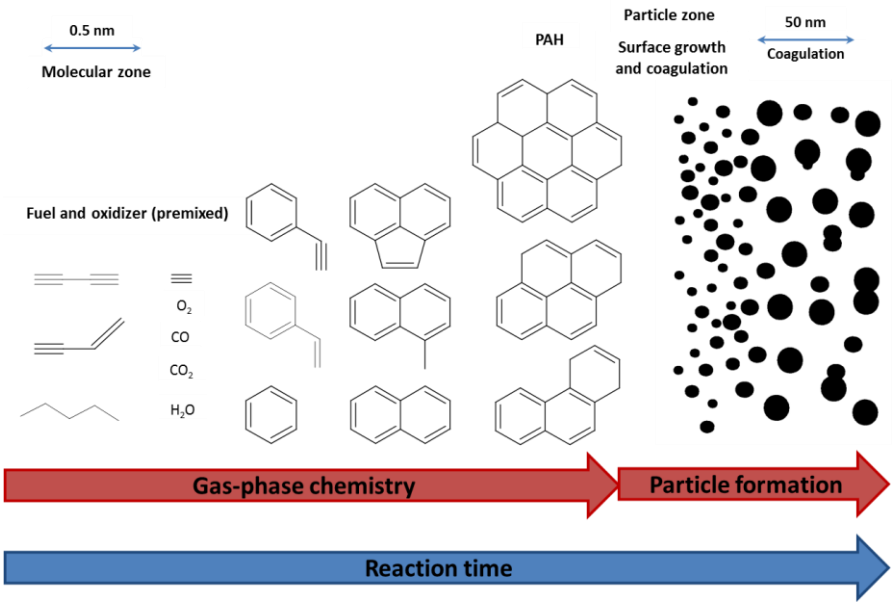

Figure 1.1: Schematics of soot formation [3].

Figure 1.1 shows that the hydrocarbon fuel first decomposes to smaller hydrocarbon radicals and from which small hydrocarbon molecules, especially acetylene, are formed. In the presence of an excess of fuel molecules, free radicals initiate chain branching which lead to the formation of larger hydrocarbons. Larger aromatic rings are mainly formed via acetylene addition.

Soot formation has been studied by several groups and various pathways have been proposed to describe the soot particle formation. Different species are considered as soot producing precursors. Among them: Polyynes [4-7] and polycyclic aromatic hydrocarbons (PAH) [8-10]. Several studies have been published about formation reactions of the first aromatic rings, i.e., benzene or phenyl radical, from aliphatic components. Frenklach summarized the main result of these studies in a review paper [11] and discussed that the reaction pathways of the first aromatic ring formation can occur through molecules with even or odd numbers of carbon atoms. Among the reactions with an even-carbon-atom numbers, the most important ones are the addition of C_2H_2 to n-C_4H_3 and n-C_4H_5 [5, 8, 12-14].

$$\text{n-}C_4H_3 + C_2H_2 \rightarrow \text{Phenyl} \qquad \text{(R1.1)}$$

$$\text{n-}C_4H_5 + C_2H_2 \rightarrow \text{Benzene} + H \qquad \text{(R1.2)}$$

But Miller and Melius [15] discussed that n-C_4H_3 and n-C_4H_5 could not have the high concentrations required and that they are rapidly transformed into their stable isomers, iso-C_4H_3

and iso-C_4H_5. Instead, they introduced a pathway involving species with an odd number of carbon atoms, e.g., combination of propargyl radicals [16-18].

$$C_3H_3 + C_3H_3 \rightarrow \text{Phenyl} + H \quad \text{(R1.3)}$$

$$C_3H_3 + C_3H_3 \rightarrow \text{Benzene} \quad \text{(R1.4)}$$

The surfaces of carbon nanoparticles from hydrocarbons are expected to be partially saturated with hydrogen. Thus, current models describing the formation and growth of soot particles rely on description of reactions that involve hydrogen. This forms the background for the often-used HACA (hydrogen abstraction, acetylene addition) mechanism of aromatics growth [5]. The term HACA was first used by Frenklach and Wang [8] and refers to a repetitive reaction sequence of two main steps:

1. Abstraction of a hydrogen atom from the reacting hydrocarbon by a hydrogen atom:

$$A_i + H \rightarrow A_{i-} + H_2 \quad \text{(R1.5)}$$

2. Addition of gaseous acetylene molecule to the formed radical site:

$$A_{i-} + C_2H_2 \rightarrow A_iC_2H_2 \quad \text{(R1.6)}$$

Here, A_i is an aromatic molecule and A_{i-} is its radical. The $A_iC_2H_2$ radical can produce a stable aromatic molecule via H abstraction.

There is, however, still some controversy about the best way to model soot formation. Experiments under conditions with different type of hydrocarbons exhibiting variable C/H ratios or hydrogen concentrations provide an excellent way to shed light on these questions and to test and develop chemical kinetics mechanisms. The influence of hydrogen and the influence of various fuels on the soot yield have been studied in several experimental and theoretical studies [5, 19-21]. Hydrogen was added to selected fuels to study its influence on the overall combustion or pyrolysis process; but the main aim was to investigate the influence of hydrogen on the soot yield [22-26].

Soot formation is based on a complex sequence of sub-processes from formation of molecular precursors, inception of particles from PAH to coagulation and carbonization. To clarify the role of hydrogen on soot formation, literature studies focused on measuring the soot yield, the optical density, and the particle diameter in flames [4]. Although there is a consensus about benzene formation as a clue towards the formation of particle precursors, the dominant pathway is not well understood.

This study focusses on the formation of molecular precursors of soot by elucidating the reaction channels responsible for soot particles formation up to formation of aromatics and to investigate the influence of hydrogen on soot formation. The measurements are performed in a shock tube connected to a high-repetition-rate time-of-flight mass spectrometer (HRR-TOF-MS) which enables time-resolved concentration measurements of multiple species simultaneously at the expense of reduced sensitivity (~5×10^{15} cm^{-3}) in comparison to spectroscopic techniques. To study the role of hydrogen in soot formation, two hydrogen-free hydrocarbons with systematically different initial decomposition path (CCl_4 and C_3O_2) are studied. Additionally the thermal decomposition of C_2H_2 and effect of molecular hydrogen addition in soot formation is studied.

The thesis is organized as follows: First the principles of chemical kinetics, shock tubes, and time-of-flight mass spectrometry behind shock waves are given (chapter 2). Chapter 3 introduces the experimental setup that was used for this study. Experimental results are presented in chapter 4. The pyrolysis of the carbon tetrachloride (CCl_4), carbon suboxide (C_3O_2) and acetylene (C_2H_2) behind the reflected shock wave is investigated. The effect of molecular hydrogen addition in acetylene pyrolysis is also investigated. Chapter 5 and 6 close the thesis with an outlook and a summary.

2. Theoretical and experimental background

2.1. Reaction kinetics

The experiments that are performed in the framework of this thesis will be compared to results of simulations based on chemical kinetics models. Therefore, it is necessary to describe the theory of the chemical kinetics modeling. Chemical kinetics deals with the mechanisms of chemical processes and the rates of the individual elementary reactions. The chemical reactions that proceed in time should be expressed in terms of mathematical equations.

Chemical reactions can be described through the collision theory where the reactant atoms or molecules collide with each other. Collision with sufficient energy leads to the breaking of bonds which initiates the reaction. Alternatively, unimolecular reactions can proceed via thermal activation.

2.1.1. Reaction mechanisms

Any complex chemical reaction mechanism can be broken down into a series of one or more single-step reactions called elementary reactions. Elementary reactions are either dissociation/isomerization of a single reactant molecule which is called a unimolecular reaction. Unimolecular reactions occur when a molecule rearranges itself to produce one or more products. Examples include the thermal decomposition, ring opening, and racemization. The following reaction is an example of the unimolecular reaction that the molecule of ozone decomposes to a molecule of oxygen and an atom of oxygen.

$$O_3 \rightarrow O_2 + O \qquad \text{(R2.1)}$$

Another type of the elementary reaction is the bimolecular reaction, which is a single reactive collision between two molecules. Reaction of ozone and hydrogen is a good example of the bimolecular reaction.

$$O_3 + H \rightarrow O_2 + OH \qquad \text{(R2.2)}$$

Elementary reactions can also be termolecular which incorporates three reactants. This type of reactions usually describes recombination reactions.

One of the simplest combustion reaction systems is the oxygen-hydrogen mechanism [27]. The overall reaction can be written in the following general form.

$$2H_2 + O_2 \rightarrow H_2O \quad \text{(R2.3)}$$

On a microscopic level, the oxidation of hydrogen is more complicated and includes many species that are produced and consumed during the combustion and involves a sequence of elementary reactions.

An elementary reaction is the chemical reaction in which one or more chemical species react directly to form products in a single reaction step and cannot be further broken down into individual reactions. Two typical elementary reactions during the oxidation of hydrogen are the following chain branching reactions of the molecular oxygen with the atomic hydrogen and molecular hydrogen with atomic oxygen which produce large amount of OH radicals.

$$O_2 + H \rightarrow OH + O \quad \text{(R2.4)}$$

$$O + H_2 \rightarrow OH + O \quad \text{(R2.5)}$$

A reaction mechanism for combustion modeling consists of several elementary reactions and many species and in the ideal case is valid for all temperatures and all compositions. Considering that the chemical mechanism includes *R* reactions and *N* species, the rate law for species X_i is calculated by summing the rate law of all elementary reactions, in which the species X_i is involved [28].

$$\frac{d[X_i]}{dt} = F_i(X_1, \dots, X_N; k_1, \dots, k_R) = \sum_{j=1}^{R} \left(\nu_{i,j}^{p} - \nu_{i,j}^{e}\right) R_j; i = 1, 2, \dots, N \quad (2.1)$$

R_j defines the rate of species conversion in forward and backward direction and is calculated with the following equation

$$R_j = k_j \prod_{i=1}^{N} [X_i]^{\nu_{i,j}^{e}} - k_{-j} \prod_{i=1}^{N} [X_i]^{\nu_{i,j}^{p}}; i = 1, 2, \dots, N. \quad (2.2)$$

Here $[X_i]$ is the concentration of species i, $\nu_{i,j}^{e}$ and $\nu_{i,j}^{p}$ are respectively the stoichiometric coefficients of educts and product, respectively and k_j and k_{-j} are rate coefficients of forward and backward reactions, respectively.

The equilibrium constant of a reaction is calculated from the following equation:

$$K_C = \frac{k_f}{k_r} \quad (2.3)$$

Modern theoretical methods such as Rice-Ramsperger-Kassel-Marcus (RRKM) theory [29, 30] based on transition-state theory [31] and statistical adiabatic channel model (SACM) [32, 33] provide computational estimates for rate coefficients. However, kinetics experiments are necessary to determine underlying rate coefficients. Spectroscopic techniques like absorption spectroscopy combined with shock tube provide strong tool to investigate fast elementary reactions with high spectral and time resolution.

2.1.2. Temperature dependence of the rate coefficients

A rate coefficient is characteristics of chemical reaction and helps to understand the chemical reaction on a molecular level. Rate coefficient usually depend on the temperature and increases with increasing the temperature. The relation between the rate coefficient of the reaction and its temperature dependence can often be expressed by the empirical Arrhenius equation

$$k = A \exp\left(-\frac{E_a}{RT}\right). \tag{2.4}$$

Here, $k(T,\mathrm{p})$ is the rate coefficient for the reaction, A is the pre-exponential factor, and E_a is the activation energy. R is the universal gas constant.

The plot of ln k against $1/T$ should be a straight line and its slope is equal to $-E_a/R$. This plot is called Arrhenius plot. Accurate measurements revealed the additional temperature dependence of the pre-exponential factor and the Arrhenius equation is written in the modified form as

$$k = A\, T^n \exp\left(-\frac{E_a}{RT}\right). \tag{2.5}$$

It should be noted that the rate coefficients that can be calculated from the Arrhenius equation are valid in the temperature range that was used to determine the parameters A, m and E_a and they cannot be extrapolated to temperatures outside this range.

2.1.3. Pressure dependence of the rate coefficient

The pressure dependence of the rate coefficient of unimolecular reactions is defined using the Lindemann mechanism [34]. According to Lindemann theory, reactants obtain the necessary energy through collision with other molecules, M. The excited molecule can deactivate through another collision or decompose into the products.

The Lindemann mechanism [34] defines the behavior of the reaction rate with concentration, but it does not explain precisely how the energy transfer takes place. More details about the unimolecular reactions pressure dependence are available from theory of unimolecular reactions [35, 36]. The theory of unimolecular reactions yields fall-off curves that describe the pressure dependence of *k* for different temperatures. For instance, typical fall-off curves for the unimolecular reaction of ethane dissociation ($C_2H_6 \rightarrow CH_3 + CH_3$) obtained by Warnatz [37, 38] are shown in Figure 2.1, which describe the pressure dependence of *k* for different temperatures.

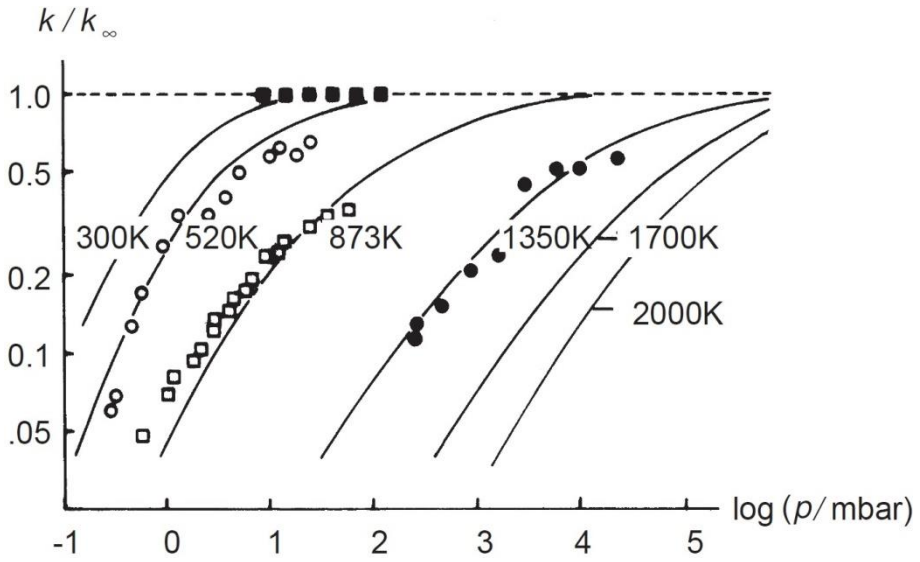

Figure 2.1: Fall-off curves for the unimolecular reaction: $C_2H_6 \rightarrow CH_3 + CH_3$ [28].

While at low pressure, *k* strongly increases with pressure, high pressures, $p \rightarrow \infty$, k reaches a limiting value k_∞. At low pressures the rate coefficient k is proportional to [M] (and thus, pressure) and results in a linear dependence. The fall-off curves strongly depend on temperature. Therefore, the rate coefficients of unimolecular reactions show different temperature dependencies at different pressures.

2.1.4. Kinetics of complex reaction system

Complex reaction mechanisms that describe the overall combustion process typically consist of series of elementary reactions incorporating the corresponding educts, intermediates and products. The reaction mechanism includes a series of elementary reactions and their formation and consumption rate coefficients. Mechanisms are validated regarding to global parameters such as ignition delay times and laminar flame speeds and concentration-time

profiles of different species [27]. For combustion of hydrocarbon fuels, the complexity increases exponentially with the chain length and therefore more elementary reactions are required to completely describe the process. The reactions are directly measured, or calculated using quantum calculations, or estimated based on analogy. But it should be noticed that even in a complex reaction mechanism, only few numbers of reactions are rate-determining for the overall process.

2.2. Shock-tube theory

Shock tubes are widely used to study the kinetics of ultra-fast gas-phase reaction at high temperatures [39-43]. The importance of shock tubes for combustion studies is evident from some several studies where large amounts of data were drawn by using a variety of diagnostics methods [44-46]. The instantaneous and homogeneous heat-up of the test gas through gas-dynamic effects within a time of 1 µs in shock tubes enables the investigation of fast gas-phase kinetics without influences of transport processes. The uniform temperature distribution and the homogeneous mixture together permit a rigorous decoupling of the physical (e.g., diffusion) and chemical processes (kinetics) within the timescale of the experiment. The shock tube offers the typical condition of temperature ranging from 600 to 4000 K and the pressure ranging from 0.1 to 1000 bar. These properties have proven and established shock tubes as versatile tools to study chemical processes under combustion conditions.

In general, shock tubes are thick-walled tubes made of stainless steel with circular, square or rectangular cross sections with a very smooth inner surface [47]. A diaphragm, normally from aluminum, separates the low-pressure part of the shock tube from the high-pressure section. The low-pressure part is referred to as the driven section, which is filled with the test-gas mixture including precursor and is subjected to the shock wave. The high-pressure part of the shock tube is called driver section and is filled with the driver gas. The driver gas is always chosen to have low heat capacity ratios (γ) and high speed of sound. For these reasons, a low-molecular-weight gas such as H_2 or He is most frequently used as a driver gas. The driver section is filled with the driver gas until the diaphragm bursts and the high-pressure driver gas instantaneously expands into the driven section. A shock wave forms in front of the expanding driver gas and propagates through the test gas. The compression of the gas by the shock wave increases the pressure and temperature of the test gas behind the incident shock wave. The shock wave reflects at the end wall of the driven section back towards the driver section, passes the test gas again and causes the second sudden increase in pressure and temperature. The gas mixture behind the reflected wave has zero velocity.

When the diaphragm bursts, the rarefaction wave expands towards the driver section's end flange. After reaching the end flange, the rarefaction wave is reflected and moves towards the driven section. The high temperature and pressure conditions after the reflected shock wave are stable up to a few milliseconds. When the reflected rarefaction wave reaches the test section close to the end flange of the driven section, it causes the decrease in pressure and the test time – which is the phase with nearly constant conditions in the test section – is over. A second reason that can limit the test time in shock tube experiments is the interaction between the reflected shock wave and the surface between the driver and the driven gases which is referred to as contact surface. This test time of typically 1–2 ms is sufficient to study many elementary reactions. Figure 2.2 shows the schematics of the shock tube.

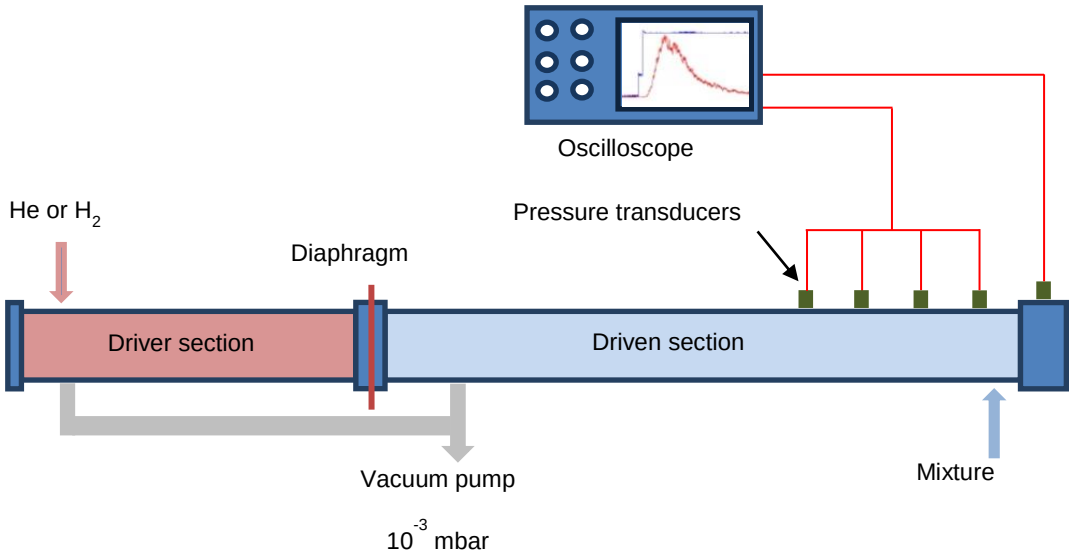

Figure 2.2: Schematics of a shock tube.

The pressure and temperature distributions before and after bursting of the diaphragms are shown schematically in Figure 2.3. The following subscripts are used to define the shock waves parameters conditions.

1: Initial condition in driven section (before the shock front)

2: Condition behind the incident shock wave

4: Initial condition in the driver section (before the diaphragm bursts)

5: Condition behind the reflected shock wave

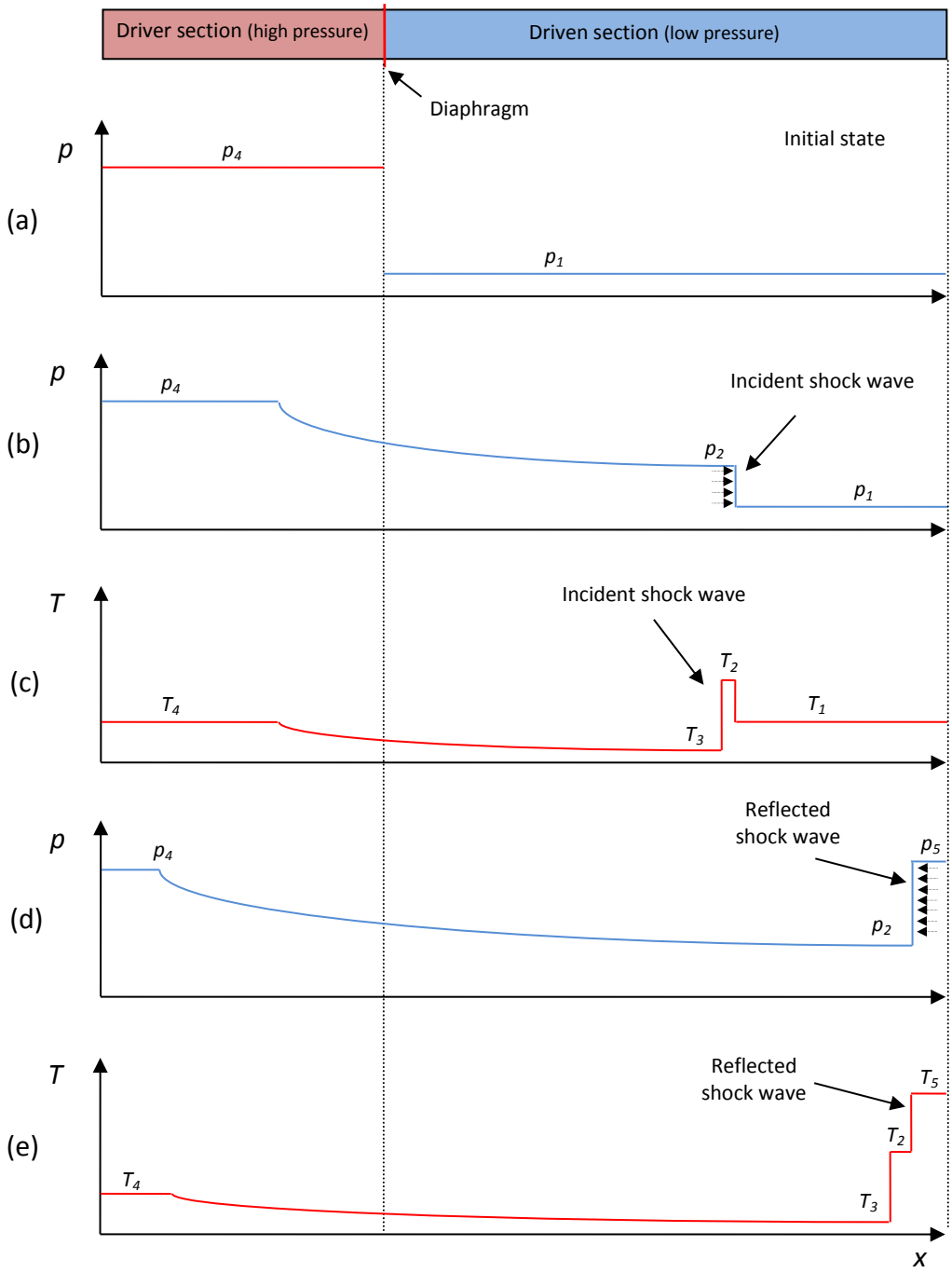

Figure 2.3: Operation principle of a shock tube [48, 49].

The driven section is filled with the test gas at the initial condition of T_1 and p_1. The driver section is filled with the driver gas until the diaphragm bursts at T_4 and p_4. The incident shock wave propagates at supersonic velocity into the driven section and compresses the test gas adiabatically. Figure 2.3b and Figure 2.3c show the pressure and temperature before arrival

of the incident shock wave to the end wall of the tube. The incident wave is reflected after reaching the end wall and the test gas is compressed again and experiences the second increase in pressure and temperature. The conditions behind the reflected shock wave are p_5 and T_5 and are respectively shown in Figure 2.3d and Figure 2.3e.

The above stated process can be shown in an *x*-*t* diagram (Figure 2.4). At $t = 0$ the diaphragm bursts and a shock wave propagates into the driven section. At the interface between the driver and driven gases the contact surface forms behind the incident wave. Simultaneously in the driver section, a set of rarefaction waves propagate in the opposite direction and are reflected after arrival the end wall of the driver section. The arrival of the reflected wave to the contact surface disturbs the test to be unsteady. The time interval between the reflection of the wave and arrival of the reflected wave to the contact surface defines the available test time, Δt. In the present study, according to the shock tube design, the test time is about 2 ms.

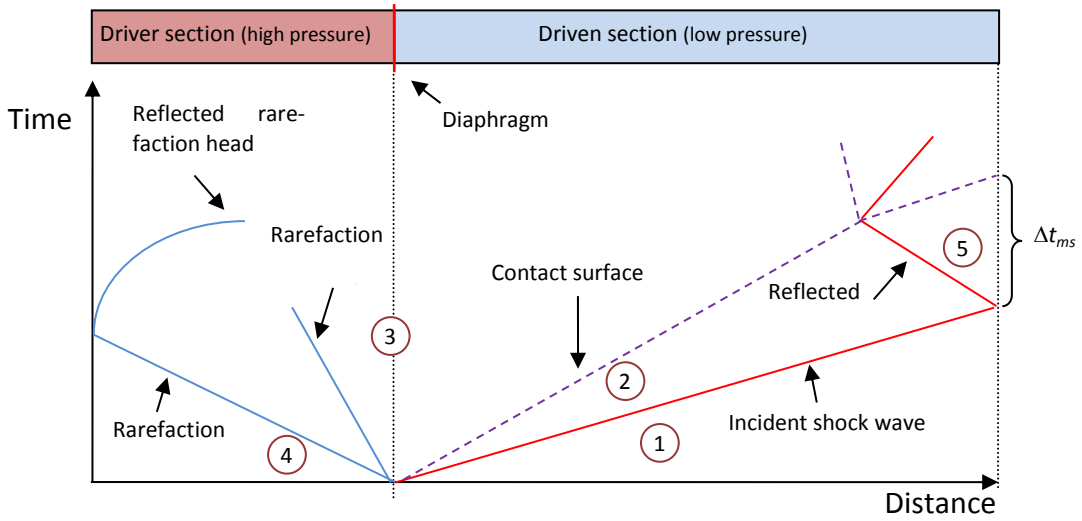

Figure 2.4: Distance-time diagram in a shock tube. Adapted from Zeldovich et al. [48].

Figure 2.4 shows five different regions. Region 1 is in front of the propagating shock wave. The pressure, density, and temperature are the initial condition of the driven section. Region 2 is behind the incident shock wave. The pressure, density, and temperature have incident shock wave. Region 3 is the part of the driver gas behind the rarefaction waves. Its pressure, density, and temperature have been influenced by the reflected rarefaction wave. Region 4 is the part of the driver gas in front of rarefaction waves. The pressure, density, and temperature correspond to the filling conditions of the driver section at the instance when the diaphragm bursts. Region 5 is behind the reflected shock wave.

The thermodynamic variables pressure (*p*), temperature (*T*) and density (*ρ*) behind the incident and reflected shock waves can be calculated using gas dynamics equations. These calculations rely on the conservation of mass, momentum, and energy (equations (2.6) to (2.8)). For the first step increase in pressure, temperature and density for an ideal gas behind the incident shock wave are given respectively by the following equations. These conservation equations are called Rankine-Hugoniot equations [50-52].

$$\rho_1 u_1 = \rho_2 u_2 \tag{2.6}$$

$$\rho_1 u_1^2 + p_1 = \rho_2 u_2^2 + p_2 \tag{2.7}$$

$$\frac{1}{2}u_1^2 + h_1 = \frac{1}{2}u_2^2 + h_2 \tag{2.8}$$

Here, *u* and *h* are velocity and enthalpy of the wave, respectively. This is a system with three equations and six unknowns. Treating the gas in the shock tube as an ideal gas with constant heat capacity ratio (γ), allows using the thermal and caloric equations of state:

$$p_2 = \rho_2 R T_2 \tag{2.9}$$

$$h_2 - h_1 = c_p(T_2 - T_1) = \frac{\gamma}{\gamma - 1} R(T_2 - T_1) \tag{2.10}$$

Substituting equations (2.9) and (2.10) in equations (2.6) to (2.8), we have three equations with four unknowns ($u_1, u_2, p_2,$ and ρ_2). Because the velocity of shock front (u_1) can be measured, pressure, density and temperature behind the incident shock wave can be calculated:

$$\frac{p_2}{p_1} = \frac{2\gamma M_1^2 - (\gamma - 1)}{\gamma + 1} \tag{2.11}$$

$$\frac{\rho_2}{\rho_1} = \frac{(\gamma + 1)M_1^2}{(\gamma - 1)M_1^2 + 2} \tag{2.12}$$

$$\frac{T_2}{T_1} = \frac{p_2}{p_1}\frac{\rho_1}{\rho_2} \tag{2.13}$$

The Mach number M_1 for an ideal gas can be determined from the velocity of incident shock wave using the following equation

$$M_1 = \frac{u_1}{\sqrt{\gamma \frac{R}{M} T_1}}. \tag{2.14}$$

Here, *M* is the molar mass of the test gas. Pressure, density, and temperature behind the reflected shock wave can be obtained from equations (2.15) – (2.17)

$$\frac{p_5}{p_1} = \left[\frac{\left(\frac{3\gamma-1}{\gamma-1}\right)M_1^2 - 2}{M_1^2 + \frac{2}{\gamma-1}}\right]\left[\frac{\left(\frac{2\gamma}{\gamma-1}\right)M_1^2 - 1}{\left(\frac{\gamma+1}{\gamma-1}\right)}\right] \tag{2.15}$$

$$\frac{\rho_5}{\rho_1} = \left[\frac{M_1^2\left(\frac{\gamma+1}{\gamma-1}\right)}{M_1^2 + \frac{2}{\gamma-1}}\right]\left[\frac{\left(\frac{2\gamma}{\gamma-1}\right)M_1^2 - 1}{2M_1^2 + \frac{3-\gamma}{\gamma-1}}\right] \tag{2.16}$$

$$\frac{T_5}{T_1} = \frac{p_5}{p_1}\frac{\rho_1}{\rho_5} \tag{2.17}$$

2.3. Mass spectrometry

Mass spectrometry is extensively applied in analytical chemistry [53-58]. It is based on the generation of ions from a gaseous samples that are accelerated in an electric field and that are then separated according to their mass-to-charge ratio (*m*/*z*) and recorded by an ion detection system [53]. In general, each mass spectrometer consists of the following parts: A probe inlet, an ion source to generate the ions, an acceleration unit for the ions, a mass analyzer, and a detector. In the ion source, sampled molecules are ionized. Different ionization techniques are used in mass spectrometry. The important parameters that should be considered are the internal energy transfer during the ionization process and the ionization cross section of the molecule that should be ionized. Some ionization techniques generate ions from energized molecular species. Electron impact ionization, chemical ionization, and field ionization are applicable for the ionization of gas-phase samples. For liquid and solid samples, molecules must be transferred from the condensed phase into the gas-phase [55]. Electrospray, atmospheric pressure chemical ionization and atmospheric pressure photoionization are suitable for liquid-phase ionization. Matrix-assisted laser desorption ionization (MALDI), secondary ion mass spectrometry, plasma desorption, and field desorption are the common ionization types in solid-state ionization. Depending on the excess energy, molecules might form a large variety of fragments. On the one hand this fragmentation is useful because it provides a pattern that is used to determine the structural information of the molecules for many applications, but on the other hand fragmentation can produce overlap-

ping signals from different species so that a clear assignment could be impossible. Routinely, appropriate ionization energies are chosen to minimize the fragmentation without too much decreasing the signal-to-noise ratio.

2.3.1. Electron impact ionization

The first step in mass spectrometry is to ionize the sampled molecules. In the present work electron-impact ionization was used that works well for the gas-phase molecules. The schematic of electron-impact ionization is shown in Figure 2.5.

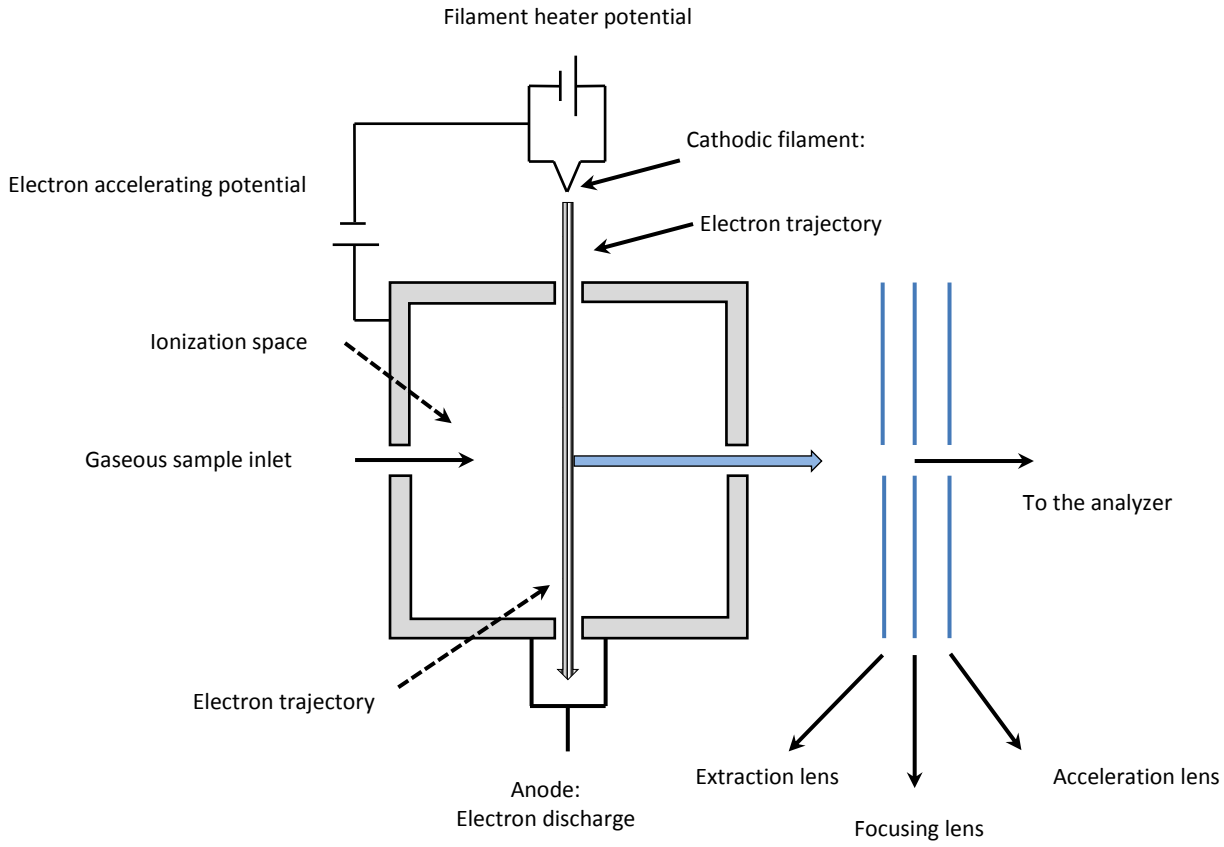

Figure 2.5: Schematics of an electron-impact ionization source [55].

This type of ion generation in mass spectrometry was introduced by Dempster [59] in 1918. By applying a heating voltage on a wire filament, electrons are emitted from the filament. The electrons are accelerated in the direction of the anode and collide with atoms and molecules of the probed gas. The generated ions then are accelerated to the analyzer. Each electron is associated with a wavelength λ given by the equation (de Broglie) (2.18):

$$\lambda = \frac{h}{m_e v} \tag{2.18}$$

Here m_e is the mass of electron, v is its velocity and h is Planck's constant. When λ has a value similar to the bond lengths of the sampled molecules, the wave is disturbed and becomes complex [60]. If the kinetic energy of the electron is larger than the ionization energy of a species molecule, an anion ($M^{\cdot+}$) can be formed:

$$M + e^- \rightarrow M^{\cdot+} + 2e^- \tag{R2.6}$$

If the energy of electrons is above 10^4 eV, i.e., the wavelength is too small, no interaction between electrons and molecules takes place and hence the molecules become 'transparent' to these electrons [55]. Therefore, normally kinetic energies of 20 to 70 eV are used, which correspond to wavelengths between 0.27 and 0.14 nm. On average at 70 eV, one ion of every 1000 molecules entering the ion source is generated [55]. A kinetic energy of 10 to 20 eV is enough for ionization of most organic molecules. During ionization, excess energy leads to excited ions and hence, fragmentation. On the one hand these fragmentation patterns can be useful because they provide information about the isomeric nature of ionized molecules. On the other hand they make the interpretation of the obtained mass spectra more complicated: When analyzing mixtures of gases, fragments from individual species can overlap with parent or fragment ions of other species. Therefore, in the current study the attempt has been made to keep the ionization energy as low as possible to minimize the extent of fragmentation. Because the number of generated ions increases with increasing ionizing energy and therefore leads to increased signal intensities, a compromise between the intensity and fragmentation is necessary. In the current study electron impact energy between 45 to 60 eV was used.

Another method for gas-phase ionization is chemical ionization (CI). This method produces ions with little excess energy through the collision of the molecule to be studied by the primary ions available in the ion source. This method yields a spectrum with less fragmentation which helps to detect the molecular species easily.

Other method of ionization for gas-phase molecules is field ionization (FI). This technique uses an intense electric field to produce ions from the molecule. The energy transfer in the FI ionization is around 1 eV and therefore, the ionization process generates ions with very low excess of internal energy and inhibits any fragmentation process. This method is appropriate to produce ions from organic molecules and also molecules with complex mixtures. This technique is in fact complementary to electron ionization and chemical ionization methods.

2.3.2. Time-of-flight mass spectrometry (TOF-MS)

In the current study, for separation of the ions according to their *m*/*z*, a time-of-flight mass spectrometer was used. In TOF-MS the generated ions are accelerated in an electric field and they then drift in a vacuum tube towards the detector. The ions with different *m*/*z* but identical kinetic energy have different velocities and therefore reach the detector at different times after pulsed formation or pulsed acceleration. The ions with the lowest *m*/*z* reach the detector first. The TOF-MS can detect multiple species simultaneously. The TOF-MS was introduced by Stephens in 1946 [61]. He proposed the linear TOF-MS with the fixed Faraday cage to collect the ions. In 1955, Wiley and McLaren [62] designed and constructed the first linear TOF-MS which was also commercialized. TOF-MS systems have been modified in the end of the 1980s through improved electronics which simplified the handling of large amounts of data. The ability of time-resolved measurements of multiple species using TOF-MS with high-repetition-rate ionization has made it a powerful instrument for gas-phase studies of chemical kinetics. Especially in combustion studies [63-65], using HRR-TOF-MS coupled to shock tubes is a strong tool to study the kinetics of complex systems behind reflected shock waves and measure species concentrations.

The relationship between the flight time or velocity and *m*/*z* can be expressed by an energy balance equation. Independent of the ionization type, the potential energy of the charged particles in the electric field is

$$E_{\mathrm{P}} = qU = e\ z\ U. \tag{2.19}$$

Here, E_{p} is the potential energy, *e* is the electron charge, *z* is the number of charges and *U* is the acceleration voltage. The kinetic energy E_{k} of an accelerated ion with mass of *m* is then

$$E_{\mathrm{k}} = \frac{1}{2}mv^2, \tag{2.20}$$

where *m* is the mass of the ion and *v* its velocity. As in the acceleration field, the potential energy of ions is converted to the kinetic energy according to

$$e\ z\ U = \frac{1}{2}mv^2 \tag{2.21}$$

As the ions enter the field-free flight tube after the acceleration, their velocity is remains constant. Therefore, the velocity can be written in term of the flight time of the ions (*t*) and length of the flight tube (*d*).

$$e\ z\ U = \frac{1}{2} m \left(\frac{d}{t}\right)^2 \tag{2.22}$$

Equation (2.22) can be rearranged to

$$t = \frac{d}{\sqrt{2e\ U}} \sqrt{\frac{m}{z}} \tag{2.23}$$

In equation (2.23), the term $\frac{d}{\sqrt{2eU}}$ contains the factors that are all related to the instrument settings. Therefore, this term can be written as a constant *c*,

$$t = c \sqrt{\frac{m}{z}} \tag{2.24}$$

showing that the ion flight time depends on the square root of its *m/z*. The relation between the *m*/*z* and the time-of-flight can be written as

$$\frac{m}{z} = a(t - b)^2. \tag{2.25}$$

The constant *b* was added to equation to correct for the measured time zero. In other words, it takes into account the uncertainties in the starting time of an ion [55]. Therefore, the conversion from flight time to mass requires the calculation of constants *a* and *b*. Thus, a calibration with species (standards) of known masses is necessary. In this study we use Xe and CCl_4 as standards. Xe has several isotopes with known distribution and CCl_4 has also many fragments according to different isotopes of chlorine. This trend is shown in Figure 2.11 and Figure 2.12.

2.3.2.1. Linear TOF-MS

The principle of TOF-MS is to accelerate the generated ions in an electric field and then measure their flight time after passing a field-free region. In the acceleration region all ions gain the same amount of kinetic energy. As all the ions acquire the same kinetic energy, they are separated in the flight tube according to their respective velocities. It means heavier ions accelerate to a lower velocity than the lighter ones. This velocity difference leads to different flight times for different *m*/*z*, thus, they can be sequentially detected by detector for real-time mass resolution. In linear TOF-MS the detector is placed in the other side of the flight tube. Figure 2.6 shows the simplified principle of linear time-of-flight mass spectrometry.

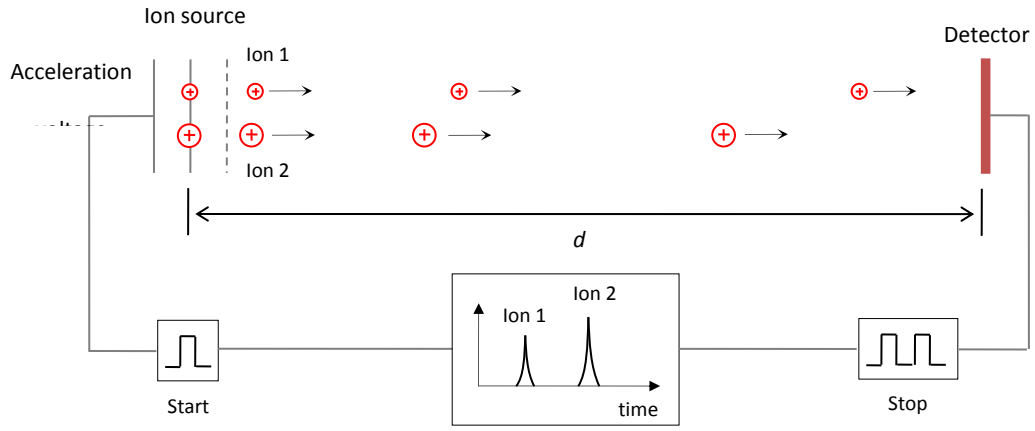

Figure 2.6: Principle of a linear TOF-MS [49, 55].

From equation (2.25) follows that all the ions exhibit the same initial kinetic energy after acceleration in the extraction field and then drift along the field-free zone where they are separated so that all ions of the same *m*/*z* arrive at the detector at the same time. In practice, however, during ionization the ions are generated at different locations in the ionization chamber. Ions that have been closest to the extraction grid are slower than the farthest ones. This variation in the velocity of the ions called the energy distribution and this energy spread of ions with the same *m*/*z* lowers the mass resolution resulting in a different time-of-flight distribution for each *m*/*z*. It means the ions with the same *m*/*z* but the different kinetic energy will arrive at the detector at slightly different times. To overcome this problem, the delayed pulsed extraction was introduced by Wiley and McLaren in 1950s [62]. In this method the ions are first separated in a field-free region according to their kinetic energy. The ions with the same *m*/*z* ratio but higher kinetic energy move further to the detector than the ones with lower initial energy. An extraction pulse then applied after a certain delay time and the less energetic ions achieve more kinetic energy and reach the detector quasi-simultaneously with the ones that have higher initial energy. For better focusing, both delay and amplitude of the pulse can be adjusted. This method is also called pulsed ion extraction or dynamic extraction.

The above stated method of focusing, delayed pulse extraction increases the mass resolution but has some limitations. In fact, delayed extraction complicates the mass calibration process and is valid just for a part of the mass range and is especially suited for low masses. For higher mass this kind of focusing is less effective and accuracy will be affected.

2.3.2.2. Reflectron time-of-flight mass spectrometry

In 1973, Mamyrin [66] introduced a way to improve the mass resolution (correct the initial kinetic energy distributions) by using an electrostatic reflector or reflectron. Figure 2.7 shows the schematics of the principle of a reflectron.

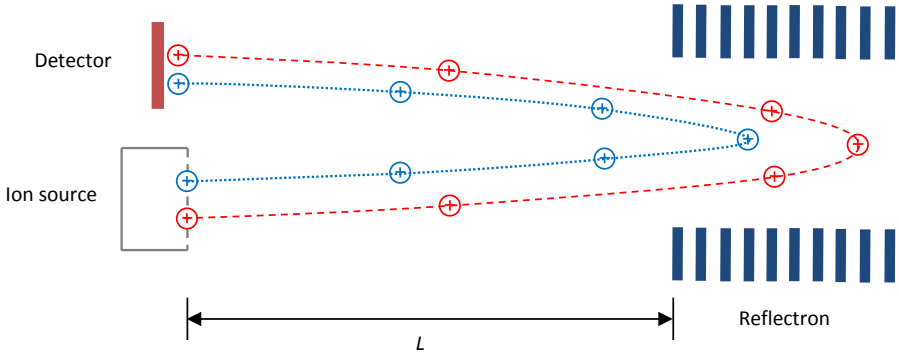

Figure 2.7: Schematics of a reflectron TOF-MS [55].

The reflectron is located at the end of the flight tube opposed to the ion source. The simplest type of the reflectron is the single-stage reflectron and consists of a series of equally spaced grid electrodes or ring electrodes with linearly increasing voltage up to a voltage slightly more than the voltage of the ion source. This produces an opposing field, in which the entering ions are reflected. The reflectron corrects the kinetic energy dispersion of the ions with the same *m/z*. The ions penetrate reflectron until they reach a (kinetic) energy level of zero, then they are accelerated again and leave the reflectron with a kinetic energy identical to the value when entering the reflectron but with the velocities in the opposite direction. The ions with higher kinetic energies, i.e., ions with higher velocities penetrate deeper and have a longer flight path, arrive at the detector almost simultaneously with the less energetic ions with the same *m/z* ratios. In the scheme in Figure 2.7 the red and blue ions have the same mass but the blue ion have a lower kinetic energy.

The flat surface of the detector (normally micro channel plate, MCP) is positioned in the side of the ion source to capture the reflected ions. The detector is either positioned coaxial with the direction of extracted ion beam or positioned off-axis with initial direction of ion beam considering the angle of reflectron. The latter one is the most common geometry in the conventional mass spectrometer.

The reflectron mode has several advantages compared to the linear mode: it corrects the effect of energy distribution of the ions at the instance of ionization on the arrival time to the detector for the ions with the identical *m/z* ratios. Moreover, a reflectron has a longer

flight path, which makes it applicable for detection of species with larger masses. The reflectron thus improves the mass resolution by decreasing the peak width (Δt) and increasing the time-of-flight [67].

The performance of the reflectron has been studied in detail by de Hoffmann [55]. The precise choice of the electric field strength, acceleration voltage and length of the field-free region yield the correct compensation, it means all the ions sharing the same *m/z* ratios but different kinetic energy have the same flight time.

Figure 2.8 shows the simplified schematic of the TOF-MS used in this study with two-stage reflectron.

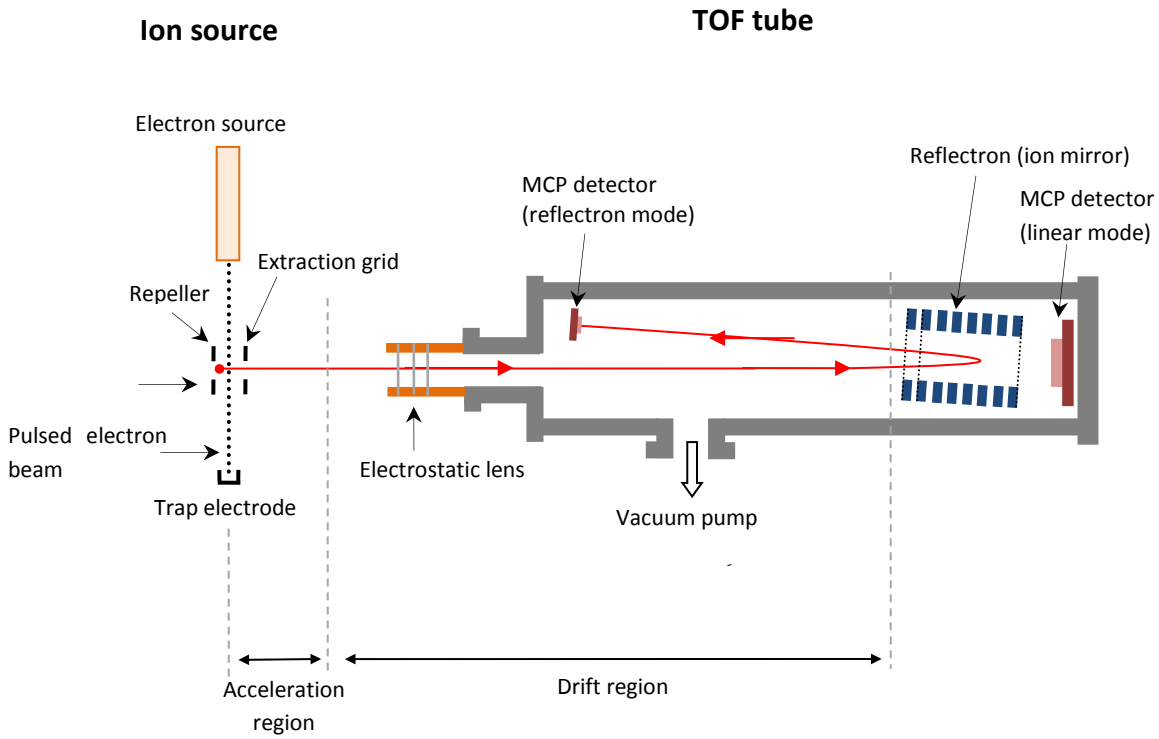

Figure 2.8: Schematics of the time-of-flight mass spectrometer [49].

In a two-stage reflectron, ions penetrate the first grid, which has the potential of the flight tube. The second grid is placed at 10% of the depth of the reflectron and its potential is two-thirds of the acceleration potential. The first stage is responsible for the strong deceleration of the ions through which they lose almost two-thirds of their kinetic energy. The third grid has the voltage slightly above the acceleration voltage. The second stage is the weaker one and is responsible to provide different penetration depths over the longer stage. The third grid also permits to place the detector on its location and use the mass spectrometer in line-

ar mode. The advantage of the two-stage reflectron is that according to the strong deceleration the device is more compact [67]. In this study, the two-stage reflectron operation was used.

2.4. Free jet sampling

One of the challenges in mass spectrometry behind the reflected shock wave is to obtain reproducible and well-defined gas sampling. Molecular-beam sampling (MBS) has been studied extensively by several groups [68-72]. The zone behind the reflected shock wave acts as a reservoir of high temperature, high pressure gases. A conical nozzle is placed on the end flange of the shock tube and the gas expands from the shock tube into the vacuum chamber of the ion source of the mass spectrometer. The shape of the nozzle, the pressure in the driven section of the shock tube and the pressure in the vacuum chamber are important parameters influencing the supersonic jet expansion downstream of the nozzle. Rapid cooling of the gas mixture is necessary to stop all the reactions while gas flows through the nozzle in the ion source.

A directed molecular beam can propagate in the diluted gases or in vacuum, when the mean free path (Λ) is larger than the distance travelled during the beam observation path [73]. In 1903, Knudsen showed that molecules from a chamber filled with gas with the pressure p_0 and mean free path of (Λ_0) that flow through a nozzle with diameter of D_0 into the vacuum chamber, propagate completely collision-free and smoothly if $\Lambda_0 > D_0$ [74]. To characterize the molecular beam, the Knudsen number Kn is introduced:

$$\mathrm{Kn} = \frac{\Lambda}{D} \tag{2.26}$$

The mean free path length is calculated according to the kinetic theory of gases assuming spherical elastic colliding gas molecules with the following equation [73].

$$\Lambda = \frac{1}{4\sqrt{2}n\pi R_{\mathrm{gas}}^2} \tag{2.27}$$

Here the n is the particle number density and R_{gas} the radius of the gas molecules. This equation is valid for molecules that are in are in the thermal equilibrium and obey a Maxwell-Boltzmann velocity distribution. Flows are classified according to their Knudsen number into three regimes [75].

- $\mathrm{Kn} > 0.5$ (Molecular flow): The mean free path of the molecules is larger than the size of the vessel or of the object under test and molecular interaction virtually no

longer occurs. The collision between the molecules and wall is dominant. This type of flow is for the regimes with the pressure less than 10^{-3} mbar. The gas particles are considered to move collision-free and smoothly.

- $\mathrm{Kn} < 10^{-2}$ (Viscous flow): The viscous flow is a type of fluid flow in which there is a continuos steady motion of the molecules and the motion at a fixed point always remaining constant. In this flow, the distance between the gas molecules is smaller than the size of the vessel and there are frequent collision between gas molecules and less frequent collision with the walls of the vessel. The collision between the molecules is dominant and the pressure is generally greater than 0.1 mbar. Viscous flow can be either laminar or turbulent depending on the flow velocity.
- $10^{-2} < \mathrm{Kn} < 0.5$ (Knudsen flow): This flow is in a transition regime between molecular and viscous flow.

The pressure increase in the molecular beam source leads to molecular collision after leaving the nozzle and creates a flow which is dominated by the hydrodynamic continuum laws [71, 73]. In the current study, the typical Knudsen number for the conditions prior to the experiment (T_1 = 298 K, p_1 = 30 mbar, D_{Nozzle}= 60 µm) is $Kn < 0.5$. The typical Knudsen number for the experiment condition (T_5 = 1500 K, p_5 = 1.5 bar, D_{Nozzle}= 60 µm) is $Kn < 10^{-2}$. The estimation of Knudsen numbers shows that none of the flows in this study are molecular flow. Therefore, in the present work, the term free jet and not the term molecular beam is used.

For performing the experiment, the driven section shock tube is first filled with the reactive mixture (test gas) of gases up to the pressure of p_1 and before performing the experiment the gas continuously leaks through the nozzle into the ion source of the mass spectrometer and subsequently the pressure drops. Thus in order to calculate the conditions behind the reflected shock wave, the corrected pressure should be considered. In our experimental setting given the small diameter of the nozzle (60 µm), this drop is around 0.1 mbar which has almost no effect on the calculation of T_5 and corresponds to the error less than 0.5% in calculation of p_5. The gas that flows into the ion source also induces a small flow in the gas in the driven section that can affect the shock velocity and hence the temperature and pressure behind the reflected shock wave [63, 76]. This induced velocity can be calculated using the following equation which has been proposed by Davies [76].

$$v_i = \left(\frac{2}{\gamma+1}\right)^{(\gamma+1)/2(\gamma-1)} \frac{A_{\mathrm{Nozzle}}}{A_{\mathrm{Plate}}} \sqrt{\frac{\gamma R T_5}{W}} \tag{2.28}$$

Here, A_{Nozzle} is the area of the nozzle entrance, A_{Plate} is the area of the plate on which the nozzle is placed; T_5 is the temperature behind the reflected shock wave and W is the average molecular weight of the gas mixture. The induced velocity was calculated for our typical experimental condition and it turned out to be around 3×10^{-4} m/s, which is negligible.

In shock-tube and time-of-flight mass-spectrometer experiments it is necessary that the shock-heated gas entering the ion source of the mass spectrometer precisely represents the gas from the zone behind the reflected shock wave. Two problems can interfere with the probe sampling from the shock tube: First, if the sampled gases are not rapidly cooled, the reactions will continue while the beam enters the ion source of the mass spectrometer. Second, after contact of the incident shock wave with the cold end wall of the tube, a thermal boundary layer develops at the end flange of the tube that has a temperature much lower than the temperature behind the reflected shock wave (T_5). If the sampled gas is contaminated with gases from the thermal boundary layer, rate coefficients of the thermal dissociation of the reactant and formation of the products appear to be lower than the ones that have been calculated based on T_5.

2.4.1. Quenching of the free jet

The ratio of the pressure behind the reflected shock wave to the pressure of the ion source of the mass spectrometer in typical experiments is large enough ($>10^5$) that the assumption of a supersonic jet expansion through the nozzle is fulfilled. To make sure that the supersonic jet is quenched fast enough to a low temperature that prevents any further reaction after entering the ion source, a reliable estimation of the free jet variables and their change during the expansion in the ion source is required [70, 71, 77]. All the important centerline properties of the jet have been discussed in details by Scoles [71] and Ashkenas and Sherman [77].

To calculate the thermodynamic variables of the free jet, an ideal gas expansion with constant heat capacity (c_p) was considered and the viscous and heat conduction effects were neglected [71]. The calculation of state variables of the free jet starts with the determination of the Mach number calculation of the flow (M) as a function of the distance from the nozzle (x). Once M is known, other thermodynamic variables of the flow such as velocity, temperature, pressure and density can be calculated. It should be noted that this Mach number is the Mach number of the free jet that flows through the nozzle into the ion source of the mass spectrometer and is different from the Mach number of the shock wave that was dis-

cussed in section 2.2. The Mach number of the flow into the ion source is analytically calculated with the following equation [71].

$$M(x) = \left(\frac{x}{D}\right)^{\frac{\gamma-1}{j}} \cdot \left[C_1 + \frac{C_2}{\left(\frac{x}{D}\right)} + \frac{C_3}{\left(\frac{x}{D}\right)^2} + \frac{C_4}{\left(\frac{x}{D}\right)^3}\right] \tag{2.29}$$

For distances (x) less than the diameter of the nozzle ($\frac{x}{D} < 1$) the following equation is proposed by Scoles [71]:

$$M = 1.0 + A\left(\frac{x}{D}\right)^2 + B\left(\frac{x}{D}\right)^3 \tag{2.30}$$

Here, x is the distance from the nozzle, D is the diameter of the nozzle, and γ is the heat capacity ratio of the expanded gas mixture. The parameters j, C_1 to C_4, A, and B are tabulated by Scoles [71] for different heat capacity ratios of different gas mixtures. The values that were used in this study are given in Table 2.1.

Table 2.1: Parameters for the calculation of the Mach number on the beam axis according to equations (2.29) and (2.30) for monoatomic gas mixtures with a adiabatic coefficient (γ) of 5/3 [71]

Expansion	J	γ	C_1	C_2	C_3	C_4	A	B
Axisymmetric (3D)	1	5/3	3.232	−0.7563	0.3937	−0.0729	3.337	−1.541

By solving the energy equation for the free jet expansion and considering an isentropic, ideal gas expansion with the constant heat capacity ratio (γ), the velocity, temperature, pressure, and density are calculated along the free jet with the equations (2.31) to (2.34) as a function of Mach number (M). The subscript '0' in the following equations is for the condition in the source (e.g behind the reflected shock wave at the interface at the nozzle entrance).

$$v = M\sqrt{\frac{\gamma R T_0}{W}} \cdot \left(1 + \frac{\gamma-1}{2}M^2\right)^{-0.5} \tag{2.31}$$

$$\left(\frac{T}{T_0}\right) = \left(1 + \frac{\gamma-1}{2}M^2\right)^{-1} \tag{2.32}$$

$$\left(\frac{p}{p_0}\right) = \left(\frac{T}{T_0}\right)^{\frac{\gamma}{\gamma-1}} = \left(1 + \frac{\gamma-1}{2}M^2\right)^{-\frac{\gamma}{\gamma-1}} \tag{2.33}$$

$$\left(\frac{\rho}{\rho_0}\right) = \left(\frac{n}{n_0}\right) = \left(\frac{T}{T_0}\right)^{\frac{1}{\gamma-1}} = \left(1 + \frac{\gamma-1}{2}M^2\right)^{-\frac{1}{\gamma-1}} \tag{2.34}$$

Where the R is universal gas constant, W is the average molecular weight of the gas mixture and T_0, p_0, and ρ_0 are respectively the temperature, pressure and density behind the reflected shock wave. It is obvious from above equations that all important parameters of the free jet depend on the Mach number, the conditions behind the reflected shock wave, and the nature of the gas.

The maximum or terminal velocity of the beam is calculated using the following equation.

$$v_\infty = \sqrt{\frac{2R}{W}\left(\frac{\gamma}{\gamma-1}\right)T_0} \tag{2.35}$$

The flow reaches at the narrowest point of the nozzle speed of sound (M = 1) and then expands along radially divergent flow lines as a supersonic flow into the surrounding vacuum. The gas density is decreased and finally the particle density is so low that no further collisions take place and the supersonic expansion turn into a free molecular beam. This distance from the nozzle where the molecular beam is formed is called the freezing distance (X_E). The place of X_E defines the maximum achievable cooling. Indeed, X_E is the location on which the last collision takes place and from that the state variables can be considered constant. X_E is:

$$\frac{X_E}{D} = 0.15(\gamma-1)^{0.5}\frac{D}{\lambda} \tag{2.36}$$

Figure 2.9 shows the estimation of state variables along the axis of free jet according to the equations (2.31) to (2.34) for typical conditions behind the reflected shock wave (T_5 = 1800 K, p_5 = 1.5 bar). The diameter of nozzle was 60 µm. The average molecular weight of the mixture was set to 20.3 g/mol which typical for mixtures used in this work (which constitutes mostly of the bath gas Neon) and γ = 5/3 was chosen. The maximum distance to nozzle diameter ratio (x/D) in this figure corresponds for the freezing distance X_E**.** The temperature, pressure and density were normalized to the condition behind the reflected shock wave (T_5, p_5, and ρ_5). The velocity was normalized to the final velocity of the free jet.

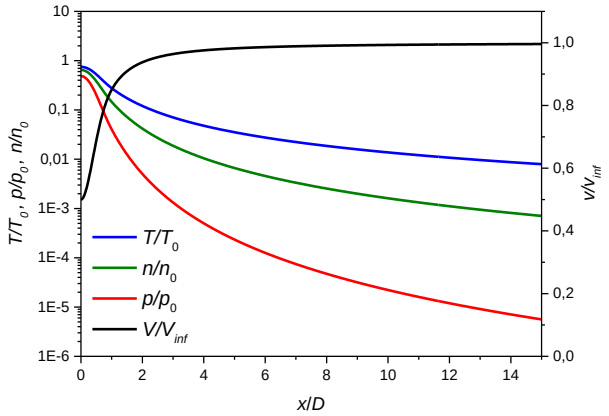

Figure 2.9: Normalized state variables of the free jet along the beam axis for 60 µm nozzle, T_0 = 1800 K and p_0 = 1.5 bar. The mixture contains 2% C_2H_2 and 1% Ar in Ne.

As it can be seen in Figure 2.9 at $x/D \approx 5$, the velocity of the jet is almost equal to the final velocity. The temperature (T), pressure (p), and density (ρ) also drop rapidly to values that guarantee freezing of the gas composition. Therefore, the concentrations of the free jet reflect the composition of the gas behind the reflected shock wave.

2.4.2. Influence of the thermal boundary layer

The sampled beam in the TOF-MS should represent the gas in zone behind the reflected shock wave. After contact of the incident shock wave with the cold end wall of the tube, a thermal boundary layer (TBL) develops at the end flange of the tube that has a temperature much lower than the temperature behind the reflected shock wave (T_5). If the sampled gas is contaminated with gases from the thermal boundary layer, rate coefficients of the thermal dissociation of the educts and formation of the products appear to be lower than the ones that have been measured based on T_5. The formation and growth of the TBL on the end flange of the shock tube and its effect on the sampled gas with the mass spectrometer have been studied by different groups [78-83]. Dove and Moulton [79] assumed that the sampling takes place from a hemisphere with the radius of R centered on the nozzle and the TBL expands one-dimensionally with the length δ from the end flange of the shock tube into the shock heated gases. The fraction of gases that is contaminated with the gases from the TBL increases with time. When $\delta > R$ all the samples are drawn from the TBL. In order to delay the time until $\delta > R$ and consequently to minimize the effect of the TBL on the sampling, Dove and Moulton suggested using a conical nozzle, which is centered on the end flange with the cone pointing into the tube. Voldner and Trass [83] studied the formation of the

TBL in a shock tube more in detail. They extended the studies of Dove and Moulton by considering the effect of the nozzle size on the time until $\delta > R$. They also considered the structure of the supersonic jet. Most importantly, Voldner and Trass found that the time until $\delta = R$ is proportional to the fourth power of the nozzle diameter r:

$$t = \frac{\beta^6 r^4 T_5}{(2.7)^6 \kappa_5^3} \tag{2.37}$$

Here, T_5 is the temperature behind the reflected shock wave, κ is the thermal diffusivity of the gas mixture behind the reflected shock wave, and β is calculated using the equation (2.38).

$$\beta = \left[\frac{3\alpha}{2}\left(\frac{2}{\gamma+1}\right)\frac{\gamma+1}{2(\gamma-1)}\left(\frac{\gamma RT}{W}\right)^{\frac{1}{2}}\right]^{\frac{1}{3}} \tag{2.38}$$

Here, α is the Liepmann correction factor [84] (0.81 for monatomic gases), R is the universal gas constant. . In the experiments of this study we used the conical nozzle with the diameter of 60 µm. According to equation (2.37) the characteristic time for the layer growth was calculated for our typical conditions, T_5 = 1800 K, p_5 = 1.5 bar, W = 20.3 kg/mol and D_{Nozzle} = 60 µm, and was found to be around 5 ms. As the sampling time in our experiment is around 2 ms, the TBL effect is negligible. Moreover, the Knudsen number (Kn) at the nozzle for the typical conditions behind the reflected shock wave in our experiments is less than 0.01. For the flows with the Kn < 0.02, the flow is continuum and boundary layer effects are negligible [63, 68].

Voldner and Trass also placed a skimmer behind the nozzle and studied its effect on sampling. They showed that the outer edges of the supersonic jet downstream of the nozzle are contaminated with gases from the TBL. By placing the skimmer between the nozzle and the mass spectrometer on the center of the free jet can prevent entering the contaminated gases from TBL on the periphery of the jet in the mass spectrometer. The tip of the skimmer should be placed between the nozzle and the Mach disk (shock diamond) that is formed in downstream of the jet in the ion source to prevent backflow into the jet. The space between the nozzle and the Mach disk is called “zone of silence” [71, 85]. The distance of the Mach disk from the nozzle is calculated according to equation (2.39).

$$\frac{x}{D} = 0.67\left(\frac{p_0}{p_b}\right)^{0.5} \tag{2.39}$$

Here, p_0 is the pressure in the source, here the pressure behind the reflected shock wave, and the p_b is the pressure in the expansion field. For the typical shock tube/TOF-MS experiments, the Mach disk forms at around $x/D \approx 400$, which is by far more than the distance between the nozzle and the tip of the skimmer in our experimental setup ($x/D \approx 30$).

Voldner and Trass also calculated the fraction of the free jet from the nozzle that passes through the skimmer according to:

$$f = \frac{\dot{m}_s}{\dot{m}} = \frac{M_s}{\alpha}\left(\frac{D_s}{D}\right)^2 \left\{\frac{\gamma+1}{2}\left[1+\frac{(\gamma-1)M_s^2}{2}\right]\right\}^{-(\gamma+1)/2(\gamma-1)} \tag{2.40}$$

Here $\dot{m}_s$ is the mass flow rate through the skimmer, $\dot{m}$ the mass flow rate through the nozzle, M_s the local Mach number at of the jet at the tip of the skimmer, D_s the diameter of the skimmer, and α the Liepmann correction factor.

For the skimmer location adopted in this work and by considering our skimmer diameter (500 µm), according to equation (2.40), less than 1% of the nozzle flow passes through the skimmer into the mass spectrometer. This corresponds to an angle with respect to the centerline of less than 3°, which means that the sampled gas is not affected by the cold wall.

2.5. Time-resolved mass spectrometry behind reflected shock waves

In 1961, Bradley and Kistiakowsky [78] introduced a technique to study chemical reactions at high temperatures behind reflected shock waves. They used TOF-MS, which was coupled to the end plate of the shock tube collinearly and sampled and analyzed the gas through the flat nozzle with the diameter of 125 µm and in time intervals of either 50 or 100 µs. Their instrument was equipped with electron impact ionization and generated ions were detected by an ion-multiplier detector. Successive mass spectra were displayed on an oscilloscope recorded by photographing individual mass spectra with a rotating-drum camera. They studied the thermal decomposition of nitrous oxide (N_2O), pyrolysis and oxidation of acetylene (C_2H_2), and thermal decomposition of nitromethane (CH_3NO_2) [78, 86, 87]. They showed reasonable agreements between their experimental data and model simulations for all studied compounds.

In 1963, Diesen and Felmlee [88] introduced a similar setup that could analyze the gas every 25 µs with the time resolution less than 1 µs. To sample the beam from the shock tube they used the flat nozzle with the diameter of 50 µm and a conical diverging nozzle with the diameter of 75 µm. The mass spectrum of each analysis was displayed on an oscilloscope and the complete mass spectra were recorded by a high-speed drum camera. Moreover, the

time-intensity profiles of two individual peaks were displayed on a dual-beam oscilloscope and were recorded on Polaroid film by intensity modulating the peak of interest. They studied the thermal dissociation of chlorine (Cl_2), hydrazine (N_2H_4), and fluorine (F_2) [89, 90]. They observed fair agreement between their measurements and simulations.

In 1965 Dove and Moulton [79] studied the oxidation of acetylene and methane in a shock tube using TOF-MS. Compared to the system of Bradley and Kistiakowsky, they made major modifications. For sampling from the shock tube they used a conical nozzle with the opening diameter of 1.1 mm, an apex diameter of 80 µm and a height of 0.3 mm. The sampled gas was ionized using electron impact ionization and was analyzed every 20 µs. They improved the pumping speed in the ion source and also increased the volume of the ion source to slow down the pressure increase in the ion source after arrival of the shock wave. Their mass spectrometer was equipped with a new recording system which permitted the recording of mass spectrum peaks on a stationary film. Furthermore, they found out that ions formed by chemical reactions inside the shock tube during the oxidation of the hydrocarbon entered the mass spectrometer together with the sampled gas and caused unresolved noise in the mass spectrum. They also investigated the growth of thermal boundary layer and calculated the time where the TBL becomes dominant inferring a sampling of the gas completely from the TBL. They used a conical nozzle to reduce the portion of the gas drawn from the TBL. They studied the oxidation of acetylene and proposed the reaction mechanism for that.

In 1965, Modica [80] investigated the decomposition of nitrous oxide in a shock tube at high temperatures with a time-of-flight mass spectrometer. He studied the effect of the cold end wall on the temperature of the sampled gas with two different gas-sampling techniques. For the gas sampling from the shock tube, he first used simple pinholes with diameters of 51 and 76 µm. Later, he used a conical nozzle protruding into the reflected shock wave region with an opening diameter of 254 µm, an apex diameter of 76 µm and a height of 4.75 mm. To ionize the sampled gas molecules, electron impact ionization with an interval of 10 to 50 µs was used. The generated ions were detected by an ion-multiplier detector. He investigated the oxidation of nitrous oxide (N_2O) behind reflected shock waves. For temperatures below 3000 K, both methods yielded almost identical results. For temperatures above 3000 K, the experiments with the conical nozzle showed less error.

In 1979, Krizancic et al. introduced a setup of shock tube and TOF-MS to study nitrous oxide thermal dissociation. For sampling the gas from the shock tube, they used a combination of a conical nozzle with an entrance diameter of 76 µm and a skimmer with an apex diameter of 510 µm. The sampled beam was ionized using electron impact ionization. In their setup

the mass spectrometer was oriented at 90° to the shock tube. The 90° configuration allowed only the ionized portion of the beam to be accelerated into the drift tube of the TOF-MS and hence minimized the pressure build-up. They were the first to use the combination of nozzle and skimmer in the beam sampling part. They also constructed special equipment that amplified the signal of the TOF-MS and integrated each mass peak that was suitable for rapid data recording. Their instrument could be used to select up to eight peaks of each mass spectrum and to store the data up to 128 mass spectra. The gas could be sampled and analyzed with the time intervals of 10–100 μs and had the estimated mass resolution of 100.

Kern et al. have also studied the pyrolysis of variety of hydrocarbons with the shock tube and time-of-flight mass spectrometer [81, 91-93]. To sample the gas from the shock tube into the TOF-MS they used a conical nozzle with a diameter of 100 μm and the sampled beam was ionized using electron impact ionization and was analyzed every 30 μs. In 1997, they investigated the unimolecular dissociation of allene and propyne [94]. They reported that because of limited mass resolution of the mass spectrometer they were not able to separate the peaks of C_3H_4 (m/z = 40) and the C_3H_3 radical (m/z = 39). Thus, the experimental results were compared with the sum of C_3H_3 and C_3H_4 simulations.

Tranter et al. [63] has introduced a shock tube with TOF-MS that has been constructed for the study of elementary reactions at high temperatures. Their shock tube and the mass spectrometer were coupled by a differentially-pumped molecular-beam sampling interface containing a nozzle (D_{Nozzle} = 400 μm) and a skimmer ($D_{Skimmer}$= 320, 480, and 790 μm). The interface ensured that the samples entering the mass spectrometer were not contaminated by gases from the thermal boundary layer. Moreover, this interface allowed operating shock experiments at elevated pressure (p > 1.5 bar) behind the reflected shock wave because the arrangement reduces the mass flow in the TOF-MS. The extracted beam from the shock tube was ionized using electron-impact ionization and the generated ions were detected using a micro-channel plate (MCP) detector with the rates of 50 to 105 kHz. They investigated the thermal dissociation of cyclohexene (C_6H_{10}) and trifluoroethane ($C_2H_3F_3$) [63, 64]. They also constructed a new diaphragm-less shock tube combined with the time-of-flight mass spectrometer. This shock tube with HRR-TOF-MS gave reproducible experiments because the signal could be averaged for multiple experiments to improve the signal-to-noise ratio. Validation of this new apparatus was achieved by investigating the thermal unimolecular dissociation of fluoroethane (C_2H_5F) [95, 96].

The Olzmann group developed a new shock tube and TOF-MS setup [97, 98]. In their setup they just used a conical nozzle with the diameter of 30–140 μm to sample the gas molecules

from the shock tube. The sampled gas was ionized using the electron impact ionization and the generated ions were detected using a MCP with the rate up to 150 kHz. They studied the thermal decomposition of ethyliodide (C_2H_5I), propyne (CH_3C_2H), trifluoroethane (CH_3CF_3), and iodbenzene (C_6H_5I). They found good agreement between their experimental data and simulations.

2.5.1. Calibration

Figure 2.10 shows an example of raw data obtained in our experiments by the TOF-MS. The raw data are for the mixture containing 5% C_2H_2 and 1% Ar in Ne. The signal trace consists of 150 successive mass spectra measured within 1.5 ms. Each 10 µs a mass spectrum is measured. These fine structures are hidden in the respective spikes of the spectra. The downward pointing peaks are the mass spectra and the upward peaks represent the timing signals captured on the digitizer. The data acquisition starts before the incident shock wave reaches the end plate of the tube and the first part of the data set is detected before the passage of the shock wave which is referred to pre-shock. The more intensive part is the signal behind the reflected shock wave refers to post-shock conditions. The steep rise in the intensity at time ~400 µs is due to the compression induced by the shock arrival at the endplate which is accompanied by strong pressure build-up in the zone behind the reflected shock wave.

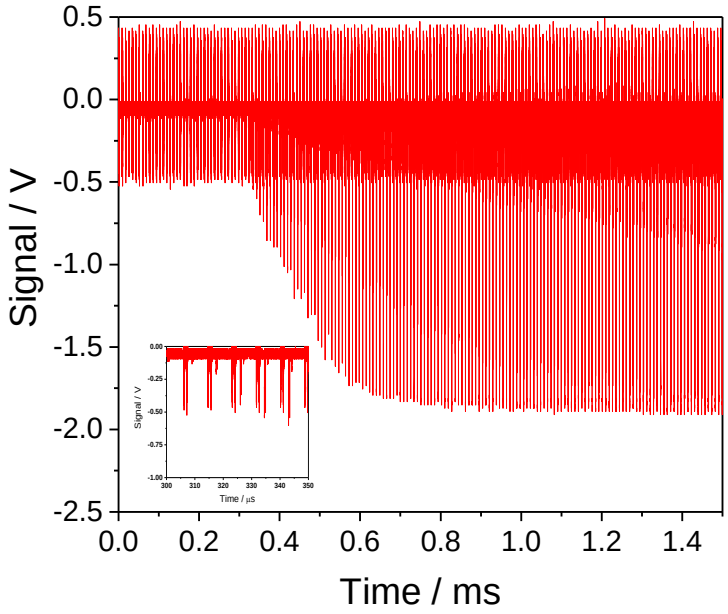

Figure 2.10: Raw HRR-TOF-MS data. The repetition rate is 100 kHz and the data are for 1.5 ms. The mixture is 5% C_2H_2 and 1% Ar in Ne, p_5 = 0.95 bar and T_5 = 2225 K.

2.5.1.1. Time to mass calibration

As explained in section (2.3.2) the assignment of the peaks requires time-of-flight to mass calibration. The corresponding *m*/*z* is calculated for each peak from its time of occurrence *t* (the flight time of each species) using the following equation.

$$\frac{m}{z} = a(t-b)^2 \tag{2.41}$$

Where *a* and *b* are the constants that are determined from calibration measurements with noble gases mixtures. A typical mass spectrum obtained with a mixture of Xe is shown in Figure 2.11. The peaks corresponding to various isotopes of Xe that differ by Δ*m*/*z* = 1 are clearly resolved.

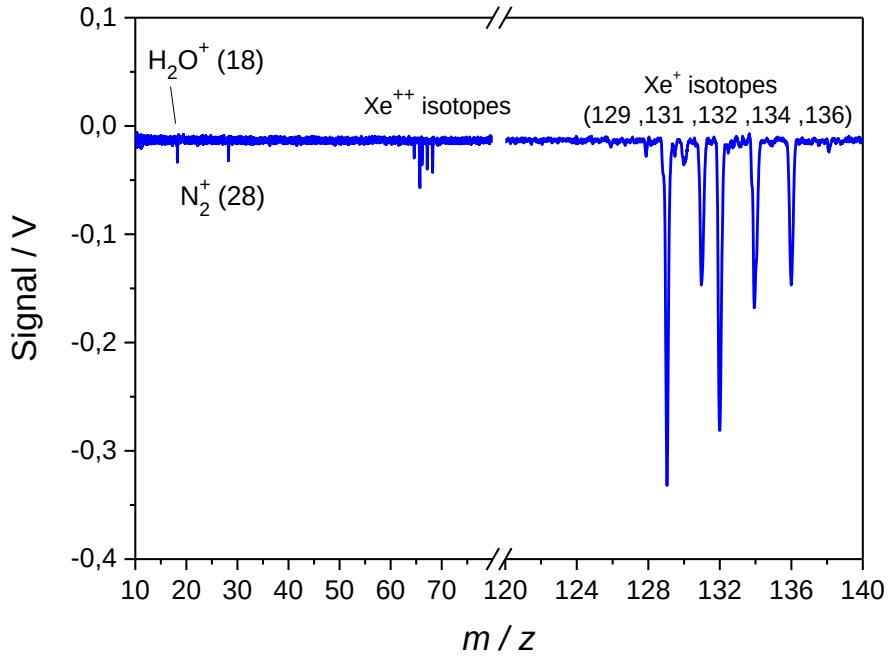

Figure 2.11: Averaged mass spectrum (accumulated from five ionization cycles) obtained in a calibration experiment at room temperature with Xe.

Figure 2.12 shows the calculated values for *a* and *b* for a typical settings of the mass spectrometer in this study. It should be noted that the electron impact energy has no influence on the flight time of the species. Increasing the electron impact energy breaks more chemical bonds and results in sharper peaks and higher intensity of fragments. It means with increasing the electron impact energy we can provide higher peaks that can be better resolved.

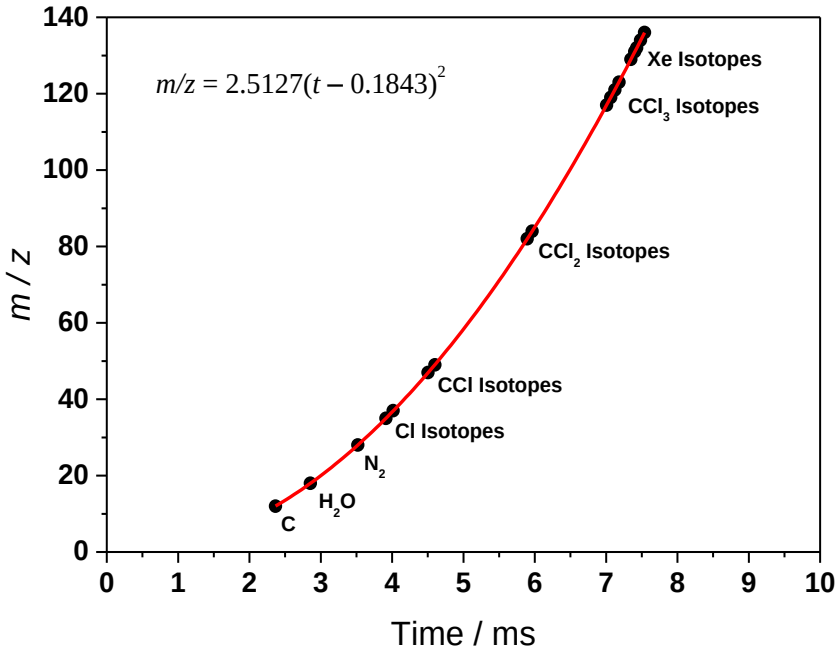

Figure 2.12: Time-to-mass calibration curve.

2.5.1.2. Intensity to concentration calibration

To measure the concentration of the different species, the respective peak area is determined by integration. The peak area is correlated to the number of the detected ions which is again linked to the concentration of the respective species for the given ionization energy. Therefore, to link the measured peak area to the concentration of the species, calibration is required. The integration is accomplished by using the software developed by Olzmann's group [98]. The next step of evaluation is the conversion of the obtained intensity profile to the concentration-time profile. For this purpose, necessary correlations are determined with calibration experiments that use gas mixtures with variable concentrations of the species to be calibrated and with constant internal standard concentration. Then, the intensity ratio (I_x/I_{Ref}) of the species is plotted versus the ratio of their partial pressures.

$$\frac{I_X}{I_{Ref}} = m_X \cdot \frac{p_x}{p_{Ref}} \tag{2.42}$$

Here I_X and I_{Ref} are the integrated peak areas of the species to be calibrated (X) and internal standard (Ref), respectively, p_X and p_{Ref} are the known partial pressures, and the m_X is the calibration factor. Figure 2.13 shows the typical calibration diagram for CO in carbon suboxide (C_3O_2) pyrolysis as an example. Krypton (Kr) was used as an internal standard.

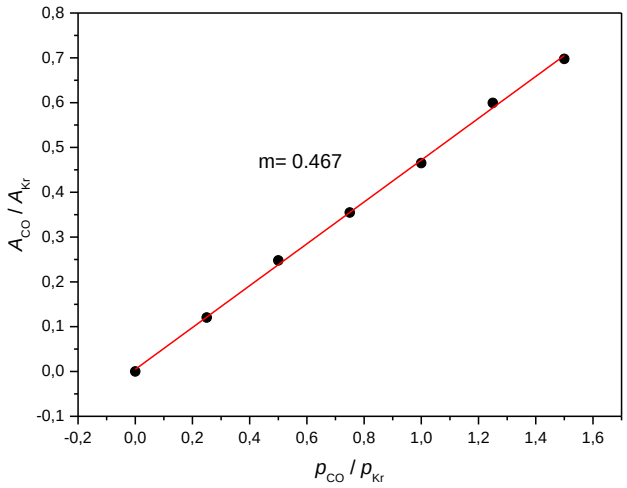

Figure 2.13: Calibration diagram for the determination of absolute CO concentration.

Considering the proportionality between pressure and concentration under ideal gas behavior, equation (2.42) can be written in the following form:

$$c_{\mathrm{X}} = \frac{1}{m_{\mathrm{X}}} \frac{I_{\mathrm{X}}}{I_{\mathrm{Ref}}} c_{\mathrm{Ref}} \tag{2.43}$$

By linear fitting, the calibration factor can be determined from slope of the line.

In all studies that have focused on shock tubes with TOF-MS, especially in the works of Kern et al. [81] and Krizancic et al. [82], the requirement of using an inert gas as an internal standard has been discussed. As shown in Figure 2.10, in TOF-MS signal behind reflected shock waves, the density in the sampled beam extracted from the jet centerline does not rise sharply in keeping with the pressure rises instantaneous (less than 1 μs) behind the reflected shock wave. Instead, a gradual rise in the signals was observed and referred to as the transient effect. In the earlier studies, this transient effect had a duration on the order of 1 ms. With the advances in the shape of the nozzle and the skimmer, with increased nozzle-skimmer separation and also with increased pressure behind the reflected shock wave, this time has been decreased. Ryason [99] reported on a transient time of around 0.25 ms and related it to the phenomena similar to the starting process in the leak similar to what experienced in shock tunnel [100]. Gay et al. [101] reported a transient period of around 0.1 ms and attributed the phenomena to an unsteady gas flow in the mass spectrometer. Krizancic et al. [82] similarly reported an irreproducible transient signal for the first 0.1–0.3 ms and associated it to the above stated reasons, as well as to the pressure build-up in the confined region behind the nozzle. Thus, there is a superposition of gas dynamic effect and also kinetics related to concentration changes on the peaks. To overcome this rise in signal and to re-

move the gas-dynamic effect from those caused by chemical reactions, an inert gas is added to the mixture as an internal standard and the intensity of all species (peak areas) of interest are normalized to the peak area of this internal standard. A noble gas such as argon is normally used for this purpose. In this study either argon (Ar) or krypton (Kr) was used as internal standard. The reactant(s) under study and the reference (Ar or Kr) are normally diluted in neon (Ne), which is often used as bath gas because of its low electron-impact ionization cross-section [102]. It was proven that Neon as bath gas has a negligible effect on the calculated rate coefficients from TOF-MS data [63].

Figure 2.14 illustrates the normalization with an internal standard. In both figures the results of the same shock wave experiment for the mixture containing 5% C_2H_2 and 1% Ar in Ne at T_5= 2225 K and p_5= 0.95 bar are shown. Figure 2.14a shows the time history of the measured peak area of Ne (blue squares) and Ar (red circles). Figure 2.14b shows profile of Ne normalized to Ar. As it can be seen that the separation of the chemical kinetic and gas dynamic effect is possible in this way and the reaction process can be correctly produced. In this study, to ensure that the signal-to-noise ratio of the signal of the internal standard (here Ar) does not deteriorate the measured signals after correction, a spline function was fitted to the measured signal of the standard and was used for normalization. To check if this spline fit affect the kinetics data that are extracted from the concentration-time profiles, cyclohexene (C_6H_{10}) decomposition was used as a benchmark because the reaction proceeds in one step and is well validated. The experiment was repeated four times at almost the same condition and then the Ar signal intensity profile was averaged to decrease the signal-to-noise ratio. The measured rate coefficient of the C_6H_{10} concentration-time profile for 3 cases (Ar profile, averaging the Ar signal, fitting the Ar with spline) did not show any significant difference.

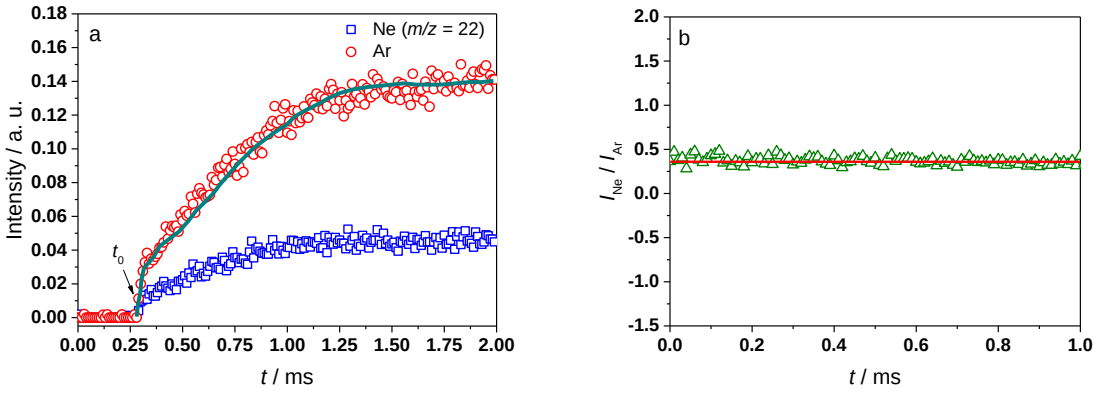

Figure 2.14a: Uncorrected time profiles of Ne (blue squares) and Ar (red circles).
b: Intensity time profile of Ne normalized to Ar.

The main question is, why the sudden change in the pressure in the shock tube (t < 1 µs) by such a lasting intensity increase in the mass spectrometer (~1 ms) reproduced and if it could be because of the rise in background pressure in the ion source. Dürrstein [98] studied these phenomena in detail and showed that the measured signal intensities achieve much earlier the constant level (around 1 ms), while the background pressure build-up establishes (100 ms) after reflection of the shock wave to reach to the constant pressure. Therefore, one can conclude that the rise in the intensity profile is independent of the background pressure rise in the ion source of the mass spectrometer.

3. Experimental

3.1. Shock tube

In this study the experiments were conducted in a conventional stainless-steel diaphragm-type shock tube. Figure 3.1 shows the schematics of the shock tube used in this study.

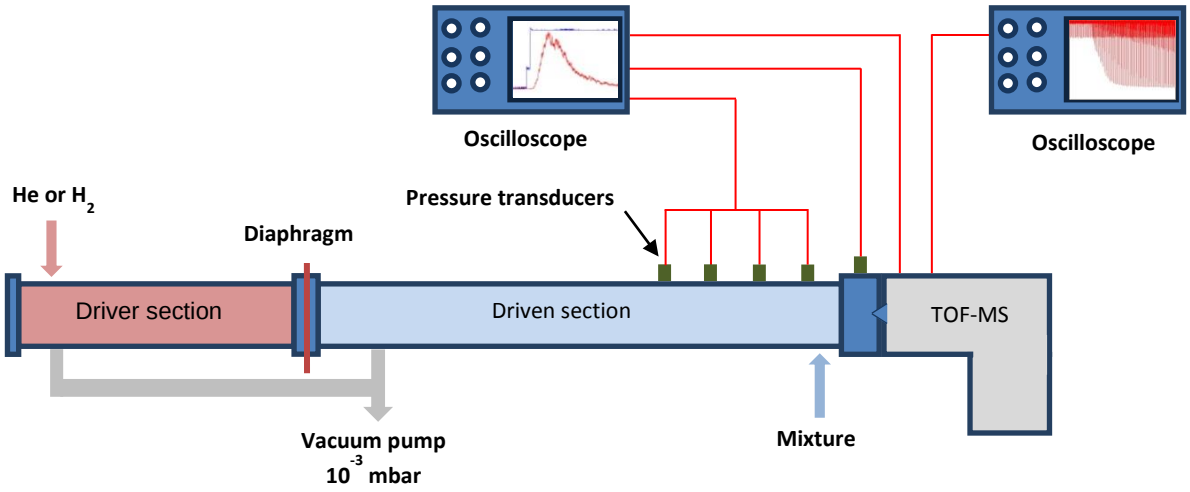

Figure 3.1: Simplified schematics of the shock tube with time-of-flight mass spectrometer.

Both the driver section (high pressure section) and the driven section (low-pressure section) have an inner diameter of 80 mm. The driver section has a length of 2.5 m and the driven section has a length of 6.3 m. The entire shock tube including the mixing vessel is equipped with heating sleeves (Tyco thermal control), which allow heating the entire apparatus up to 400 K. This enables investigation of the chemicals with low vapor pressure.

For the investigation of this work which involves the possibility of particle formation during the experiments, a particle-tolerant pumping system is used. Both shock tube sections are evacuated with a dry vacuum pump (Edwards dry star; model QDP 80) which is used for pre-pumping to achieve a pressure down to 2×10^{-2} mbar. This pump is also used to pump out the mixing vessel of the shock tube. The QDP 80 pump is supported by a roots pump which pumps down both driver and driven sections to 1.8×10^{-3} mbar. The driver and driven sections of the shock tube are separated by an aluminum sheet (diaphragm) prior to the experiment. To perform the experiment, the driven section is filled with the test gas and then to generate the shock wave the driver section filled with the driver gas until the diaphragm

bursts. Aluminum sheets with a thickness in the range 50–90 µm are used as diaphragms in this study. The temperature and pressure behind the shock wave is affected by both the thickness of the diaphragm and the filling pressure of the driven section (p_1). Varying the thickness of the diaphragm affects the pressure behind the reflected shock wave (and simultaneously the temperature, see table 3.1). For a given diaphragm thickness varying p_1 affects the temperature behind the reflected shock wave. Typical post reflected-shock temperatures (T_5) and pressures (p_5) that can be generated from the different diaphragms are shown in Table 3.1.

Table 3.1: Typical reflected shock pressures and temperatures for different diaphragm thicknesses at a filling pressure p_1 = 50 mbar.

Diaphragm	p_1 / mbar	p_5 / bar	T_5 / K
50 µm	50	1.0	1095
70 µm	50	1.5	1375
90 µm	50	1.8	1520

The adequate sealing between the two parts of the tube is guaranteed by using two Viton O-rings in both sides of the aluminum diaphragm. The driver section is located on sets of rollers that enable separating two parts of the tube after the experiment and replacing the used diaphragm with a new one.

Either helium or hydrogen can be used as the driver gas. Filling of the driver section is controlled by a magnetic valve through which the driver gas is introduced; the rupture pressure (p_4) is measured with a Keller manometer (model Mano 2000). After an experiment the shock tube is evacuated to 10^{-2} mbar and filled with nitrogen to atmospheric pressure before the diaphragm is replaced.

The filling pressure in the driven section is measured with an Edwards capacitance manometer (Trans 600 AB), which can detect absolute pressures up to 1000 mbar. The driven section of the shock tube is equipped with an equidistant set of four pressure transducers (PCB model 112A05) with a distance of 150 mm between the transducer centers. The last transducer of this set is located in a distance of 150 mm from the end plate of the driven section. A fifth pressure transducer located close to the end plate is used to measure the post-reflected-shock pressure. The signals of all pressure transducers are amplified with charge amplifiers (Kistler Kiag Swiss 5001) and read out using an oscilloscope. By measuring the time taken for the incident wave to travel between the pressure transducers the shock wave velocity and consequently the state variables behind the reflected shock wave are deter-

mined using an approach described in section 2.2. The shock tube is also equipped with a 50-liter mixing vessel, in which the test gas mixture is prepared. To ensure homogeneity the gas mixture is allowed to stand 12 hours before starting the experiments. The mixture is conducted into the driven section using a 6 mm stainless steel line which is connected to the driven section through the valve near the end plate.

3.2. Modular sampling unit

All important aspects of the molecular-beam sampling with regard to shock tube experiments and the respective gas dynamic considerations have been described in section (2.4). In this section the shock tube head and the nozzle-skimmer unit will be discussed in detail.

A 3D sketch illustrating the modular character of the measurement section is presented in figure 3.2. The end-flange separating the driven section from the TOF-MS contains a precision manufactured conical nozzle (Frey, Berlin) in the center, which allows for the extraction of a free jet. Typical nozzle diameters are 45–100 µm. When using a skimmer larger nozzles are used (e.g., 300 µm). Symmetrical pumping of the expansion chamber is crucial to prevent deflection of the sampled beam. Six tubes (separated by angles of 60°, inner diameter 25 mm) are connected to the flange holding the skimmer (see Figure 3.2). Groups of three tubes are connected to larger tubes (inner diameter 40 mm) which are connected to a joint rotary vane pump (Edwards, E2M40, 40 m^3/h) via 40-mm diameter corrugated hoses. The skimmer section is pumped down to pressures of approximately 5×10^{-2} mbar. To avoid diffusion of oil from the pump into the skimmer section an adsorption trap (Leybold) is used to separate the pump from the skimmer unit. From the skimmer section the molecular beam is led into the ion source chamber of the TOF, which is pumped with a turbo molecular pump (Pfeiffer; 520 l/s), thus resulting in a differentially pumped sampling system.

Two different skimmers (Beam Dynamics Inc.) with different diameters (100 and 500 µm) are available and each skimmer is glued to a support that can be mounted to the base plate of the skimmer unit flange (see Figure 3.2 and Figure 3.3). The drill drift tolerance of the skimmer support is 6 mm, whereas the screws that are used to mount the skimmer are only 4 mm in diameter. Thus, the skimmer support can be easily displaced with respect to the base plate which allows for a very straightforward adjustment of the skimmer position. For positioning of the skimmer a simple He/Ne laser is placed in the driver section on the centerline of the shock tube such that it irradiates the shock tube side of the nozzle. The skimmer is then aligned for maximum light transmission.

Because the position of the Mach disk in the expanding flow depends on the nozzle diameter as well as on the post-shock pressure during the experiments the skimmer position must be adjusted depending on the individual operating conditions in different sets of experiments. The variation of the skimmer-nozzle distance is achieved by spacing washers that can be placed between the skimmer support and the base plate (Figure 3.4). The minimum nozzle-skimmer distance is 2 mm. The measurement section, both sides of the skimmer unit, and the ion source chamber of the TOF-MS are equipped with ISO flanges (150 mm). Thus, either the TOF can be directly mounted to the shock tube or the skimmer section can be inserted between the shock tube and the TOF-MS. All connections use standard clamps and all flanges are sealed using Viton O-rings.

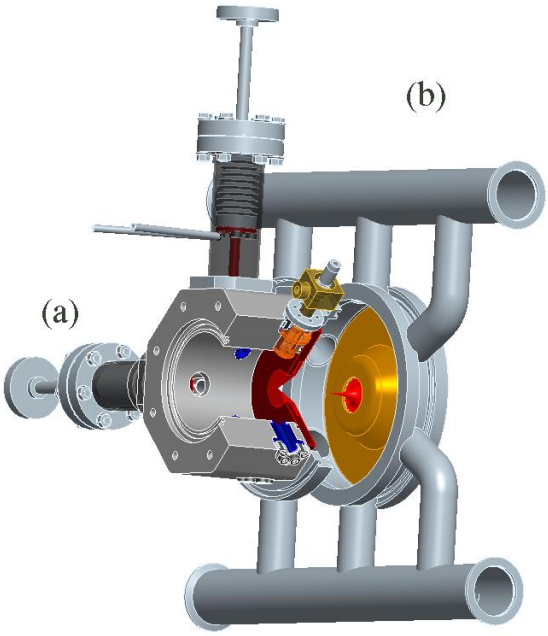

Figure 3.2: Schematic view of elements of the HRR-TOF-MS shock tube experiment. (a): Shock tube head section with end wall and nozzle. (b) Skimmer system with vacuum tubing. Note the modular character of the setup.

The blueprint of the measurement section is shown in Figure 3.3. The measurement section has an octagonal cross section and is located between the driver section and the TOF-MS. It contains two valves. One is for filling the driven section with the test mixture from the mixing chamber and the other valve is connected to a nitrogen cylinder which is used for purging the tube. The measurement section is additionally equipped with four quartz windows. The straightforward adjustment solution and the spacer plate described above are shown in the enlargement of the skimmer section presented in Figure 3.4.

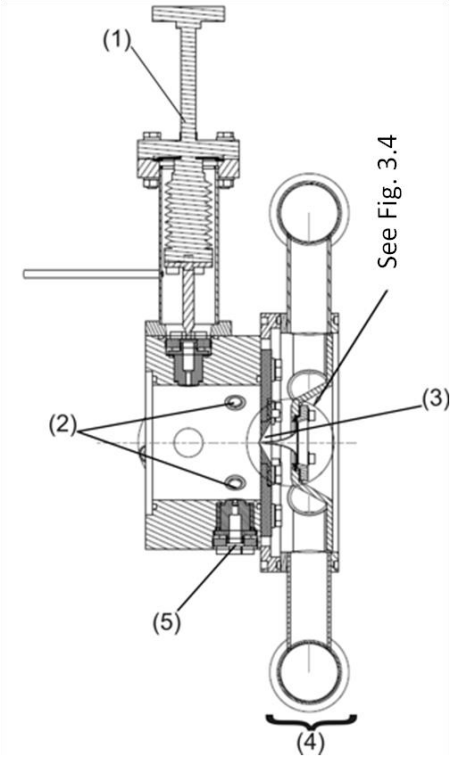

Figure 3.3: Blueprint of the measurement section. (1): Gas inlet and valve (N_2), an identical valve (pointing into the page) is used to fill the shock tube with the test gas. (2): Optical windows. (3): End plate with nozzle. (4): Skimmer section. (5): Pressure transducer.

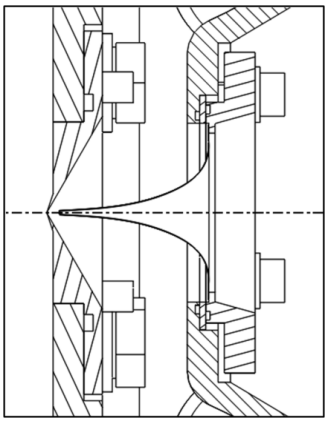

Figure 3.4: Enlargement of the nozzle and skimmer section mounted with the smallest spacer washer.

The nozzle opening is 1 mm over the end plate of the shock tube; it means that the tip of nozzle protrudes into the driven section. As it was discussed earlier it prevents contamination of the sampled gas with the gas from the cold thermal boundary layer. The inner opening angle of the nozzle is 70° and the outer angle between the end flange and surface of the

cone is 135°. In this study nozzles with diameters of 45 or 60 µm are used and no skimmer is used. Figure 3.5 shows a schematic of the nozzle used in this study.

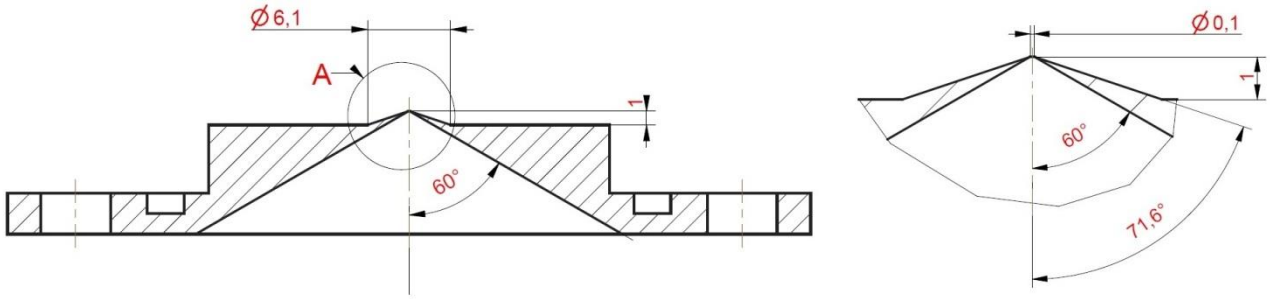

Figure 3.5: Schematics of the nozzle.

3.3. High-repetition-rate time-of-flight mass spectrometer (HRR-TOF-MS)

For time-resolved reaction kinetics studies behind reflected shock waves, the TOF-MS must be operated at high repetition rates. Therefore, the HRR-TOF-MS (Kaesdorf) was designed for repetition rates up to 150 kHz by combining a compact design (short flight distance) with high transmission energies (high flight velocities). This approach avoids the overlap of signals caused by ions from consecutive ionization cycles. Typically, repetition rates of approximately 100 kHz are used in this study. Here no overlap of consecutive spectra occurs up to m/z = 170. With respect to data analysis this is an advantage compared to the experiment described by Tranter et al. [63] that shows overlap of two successive spectra at a repetition rate of 105 kHz.

Figure 3.6 shows the schematic of the TOF-MS connected to the shock tube. The TOF is equipped with an electron impact (EI) ion source with two-stage ion extraction. A two-stage reflectron compensates for differences in flight time due to variable initial energies of the ions up to a second-order correction of approximately 8–10% of the ensemble mean energy. The energy of the ionizing electrons can be tuned from 5 to 85 eV. It is possible to ionize under field-free conditions, because ionization (200 ns – 2 µs) and extraction (300 ns – several µs, rise-time 10 ns) can be pulsed independently. Fragmentation processes or space-charge effects can cause the divergence of the ion beam, which is compensated by the use of electrostatic lenses. The maximum kinetic energy of the ions is 10 keV which is high enough to generate detectable signals for molecular weights up to 1000 u, using two-stage micro channel plate (MCP) detectors. The HRR-TOF-MS is equipped with two detectors one that is used in the reflectron mode (high resolution) and one that can be used in the linear TOF-mode (high transmission and thus improved sensitivity). In this study all the experiments were per-

formed in the reflectron mode of the TOF-MS with the flight path of 40 cm. To avoid the influence of chemically-ionized species from the shock tube, a positively-charged lens shields the ion source against the shock tube.

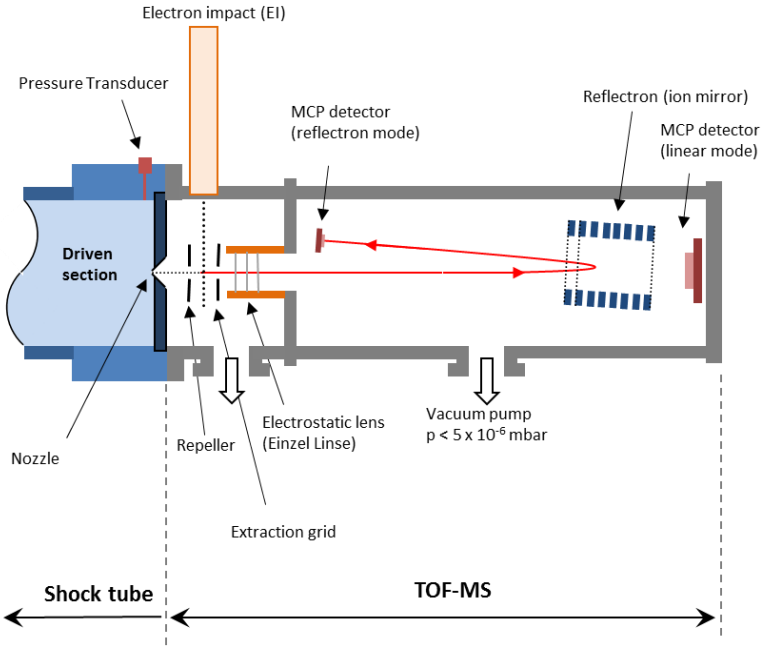

Figure 3.6: The TOF-MS at the shock tube.

The circular pinhole with a diameter of 3 mm connects the vacuum chamber of the ion source to the drift tube of the mass spectrometer. Both ion source and mass spectrometer are pumped with turbomolecular pumps (Pfeiffer, Model TMU 521 P, 520 l/s and Pfeiffer, Model TMU 261 P, 230 l/s respectively). A diaphragm pump (Pfeiffer Model MVP 055-3, 3.8 m^3/hr) is used as the backing pump for both turbomolecular pumps.

The TOF-MS is connected to the shock tube via the nozzle/skimmer system described above. Before the shock arrival the typical gas pressure in the shock tube is ~20–120 mbar. The resulting gas flow through the pinhole inside the TOF-MS causes a negligible loss of test gas in the shock tube. The flow rates are well below the pumping capacity of the TOF and constant pressure in the range of 4×10^{-7} mbar is reached in the TOF-MS. After the arrival of the shock wave, however, the shock-tube pressure increases by a factor of more than 20. The resulting increase in gas flow into the TOF-MS results in a rapid pressure increase in the TOF-MS of approximately 1×10^{-7} mbar/ms. Within the relevant test time of the shock tube (2 ms) this does not cause any significant attenuation of signals. However, after extended times, the pressure could increase such that sparking occurs between the accelerator plates that could damage the mass spectrometer detector (MCP), that has the maximal allowed pressure of

2×10^{-6} mbar. Therefore, the TOF must be switched off 5 ms after the shock arrival to prevent any damage.

3.4. Triggering and data acquisition

Triggering of the whole experiment is accomplished by a pulse delay generator PC card (BME03). A combination of a control device and a 10 MHz pulse generator (TTL) model TGP 110) synchronize the operation of the TOF and its shut-off as well as the data acquisition with the shock event. When the shock wave passes the pressure transducer farthest to the end flange, a signal is generated and this signal is amplified and then sent to a pulse generator from which a TTL output pulse is generated. Once the controller of the card receives this TTL pulse, trigger pulses from the BME delay generator are pulsed through the ion source of the HRR-TOF-MS with predefined rate and thus pulsed ionization and the time-resolved detection of the mass spectra is initiated. During the measurement period the ion source is triggered by the high-repetition-rate pulses and mass spectra are detected at the respective frequency. Chevron-type multichannel plates (Photonis) are used as detectors both in the reflectron as well as in the linear mode. An oscilloscope card (Agilent Acquiris, DP110) in the same PC that also runs the delay generator records the raw data from the HRR-TOF-MS.

After a preselected delay time the controller switches off all high-voltage devices in the TOF-MS. This is necessary because the mass spectrometer could be damaged because of the pressure increase in the after compression of the gas because of the shock wave incident. The TOF-MS is switched off via high-voltage relays that are connected to the power supply of mass spectrometer and are driven with 5 V. Hence the mass spectrometer can be operated as long as the voltage of 5 V is applied to the relay. The voltage is provided by a home-built control device and after a selected delay time the voltage is lowered to 0 V and the TOF-MS is switched off. In our experiment the delay time was set to 5 ms after start of the data acquisition. The flow chart shown in Figure 3.7 illustrates the data acquisition process.

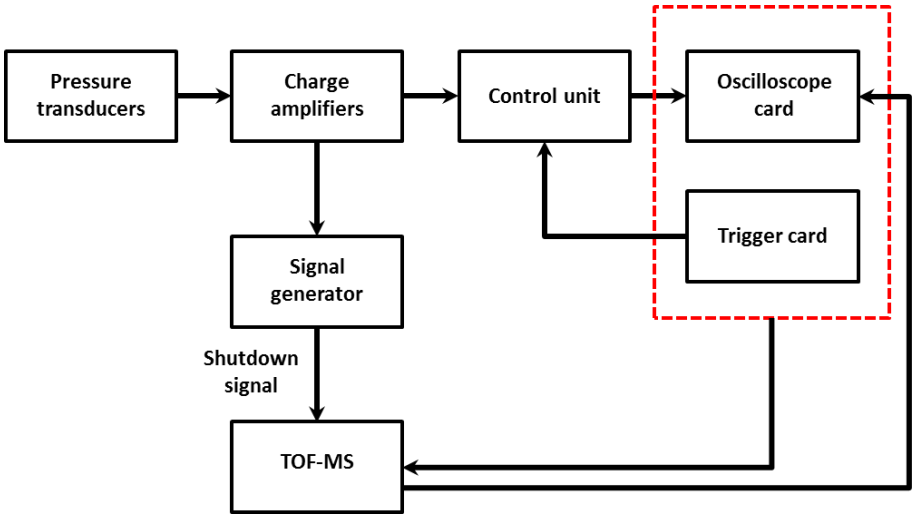

Figure 3.7: Flowchart illustrating the data acquisition.

3.5. Software

The state variables of the free jet were calculated with MATLAB. The data acquisition from the mass spectrometer was performed with the software Acqiris version 4.2 (Agilent). During data analysis, the integration of the peaks was performed with the Integration Wizard program written in LabView in the group of Olzmann [97, 98]. The calculations of the condition behind incident and reflected shock waves and also the simulation of the chemical kinetics model were done with software CHEMKIN (Reaction Design) [103].

4. Results and discussion

Soot formation from combustion has been subject of intense scientific interest for several decades. Investigations of soot formation in the pyrolysis or combustion of complex hydrocarbons – i.e., typical fuels – are difficult due to the complex kinetics of the formation of polycyclic aromatic hydrocarbons (PAH) [28], thus, many studies have focused on simpler hydrogen-free systems to clarify the role of the PAH towards the formation of soot particle and to find whether particles from hydrogen-free precursors proceed with the same mechanism like hydrocarbons. CCl_4 and C_2Cl_4 were investigated as substitutes [104-106]. Moreover, the purest process (without hydrogen impact) of carbon vapor condensation could be observed during carbon suboxide (C_3O_2) pyrolysis [107] because C_3O_2 decomposes forming a carbon atom and two CO molecules, which are nonreactive on the timescale of our experiments at T < 4000 K [108]. In this thesis first the pyrolysis of carbon tetrachloride (CCl_4) behind reflected shock waves was studied. Afterwards, the thermal decomposition of carbon suboxide (C_3O_2) was studied and finally the thermal decomposition of acetylene and the influence of molecular hydrogen addition on soot partial formation were investigated.

4.1. Pyrolysis of carbon tetrachloride (CCl_4)

4.1.1. Motivation

Carbon tetrachloride is widely used in studies of soot formation as a substitute for hydrocarbon fuels [104-106]. Moreover chlorinated hydrocarbons are among the main constituents of many industrial wastes and they may influence the soot formation in industrial furnaces. Frenklach and coworkers [109] reported higher carbon particles yields from shock-tube studies of CH_2Cl_2, $CHCl_3$, and CCl_4 pyrolysis in comparison with normal hydrocarbons. This observation was explained by the fact that the C-Cl bond is much weaker than the C-H bond and results in easier pyrolysis of chlorinated hydrocarbons than comparable non-chlorinated hydrocarbons [110]. Although a variety of complex species including chlorinated aromatic compounds can be formed during pyrolysis of carbon chlorides [111], the kinetics of carbon particles formation from carbon chlorides is supposed to be much simpler compared to hydrocarbon systems, because of the fact that chlorine does not take part in acetylene-addition and ring-cyclization reactions [110]. Nevertheless, the detailed reaction kinetics leading to carbon particle formation of carbon chlorides is yet under debate and requires further research [109].

The kinetics of CCl_4 decomposition are usually described in a simplified way in terms of a gross reaction with monatomic carbon vapor as a product or even entirely neglected in works concerning carbon particle formation based on this precursor. In analogous work of iron particle formation from $Fe(CO)_5$ pyrolysis, however, it was demonstrated that a similar approach neglecting the initial decomposition steps results in unrealistically high rates of vapor condensation [112]. Therefore, secondary reactions between decomposition products are important. According to the general theory of supersaturated vapor condensation, details of the formation of the small critical clusters can be important for the following condensed particle growth [113].

However, detailed kinetics studies of CCl_4 pyrolysis in shock tubes with classical instrumentation are difficult because most experimental methods provide either information about only one chemical species (e.g., ARAS) or measure a global parameter such as optical density. Hence, in the present study, the pyrolysis products of CCl_4 were investigated using HRR-TOF-MS coupled to a shock tube, which allows the simultaneous measurement of concentration-time profiles of the reactant and multiple intermediates and products after CCl_4 pyrolysis. The resulting time-resolved information was then used for the refinement of kinetics models.

4.1.2. Results and discussion

Several series of experiments with mixtures containing of 0.5–1.0% CCl4 and 0.5% Ar as the internal standard with Ne as bath gas was performed. The required concentration is given by the limited detection limit of the mass spectrometer (~ 10^{-10} mol cm^{-3}).

Pressures and temperatures behind the reflected shock were varied in the range of 1.0–2.3 bar and 950–2400 K. The experimental conditions are shown in Table 4.1.

Table 4.1: Experimental conditions for CCl_4 pyrolysis.

Composition	Pressure / bar	Temperature / K
0.5% CCl_4 + 0.5% Ar + Ne	1–2	990–1800
1% CCl_4 + 0.5% Ar + Ne	1.2–2	950–2400

For the study of the pyrolysis of CCl_4 (m/z = 152), for extraction of gases into TOF-MS, a nozzle with a diameter of 60 µm was used. The electron impact energy was set to 60 eV and the TOF-MS was operated with a repetition rate of 100 kHz, corresponding to a fundamental time resolution of 10 µs for the mass-specific time profiles. At these conditions, a mass range of up to m/z = 170 could be monitored without overlap of consecutive mass spectra.

In contrast to atoms, large molecules produce complex mass spectra, because electron impact ionization can lead to fragmentation in the ion source. Figure 4.1 shows the fragmentation pattern of pure CCl_4 obtained at room temperature. Note that there are no peaks corresponding to the parent masses of the CCl_4 isotopologues (m/z = 152–160), because the CCl_4^+ ion is unstable to dissociation and fragments easily [114]. The relative amplitudes of the fragment peaks are in good agreement with partial cross-sections determined by Lindsay et al. [115], chlorine isotopic abundance and distribution of different fragments of CCl_x according to chlorine isotopes.

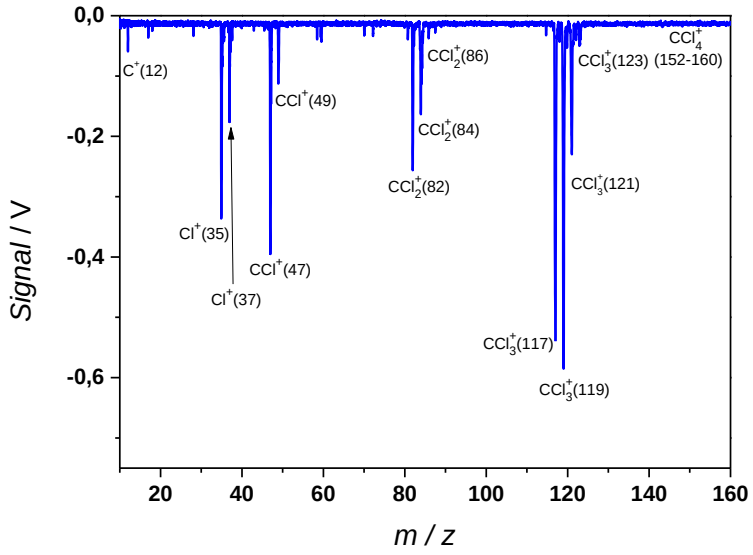

Figure 4.1: Mass spectrum of pure CCl_4 vapor obtained at room temperature (signal accumulated for five ionization cycles) at an electron impact ionization energy of 60 eV.

The kinetics mechanism of CCl_4 pyrolysis consists of 738 reactions and considers 106 species [116]. An excerpt of the reaction mechanism is given in Appendix 8.1. The mechanism describes both the primary decomposition of CCl_4 (chlorine atom loss) and formation of secondary species. The rate coefficients of most reactions that contain CCl_4 and secondary carbon chloride species up to C_2Cl_6 that have been reported before [106, 117-123] have been considered. The core of the reaction mechanism is based on the work of Kumaran et al. [117, 124], Kovacs et al. [118], and Zhiltsova et al. [106]. Especially Kumaran et al. extensively studied the kinetics of chlorine atom loss from CCl_4 and dichloroacetylene (C_2Cl_2) formation during chloroform ($CHCl_3$) pyrolysis at conditions very similar to the present work using atomic resonance absorption spectroscopy (ARAS) for the determination of the chlorine atom concentration. Nevertheless, a full mechanism of the shock-wave-induced pyrolysis of

CCl_4 in the 1500–3000 K temperature range has not yet been validated against experimental data.

The reaction mechanism also includes the formation of chlorinated polyynes and aromatics according to Zhiltsova et al. [106]. The condensation of the carbon vapor produced in the pyrolysis of CCl_4 was described by a simplified kinetics model [108, 125, 126]. Additionally, the growth of the C_n clusters ($3 < n < 85$) via C_2Cl and C_2Cl_2 was included [106]. All reactions for the gas-phase mechanism up to C_6Cl_m were assumed to be reversible with the exception of the reaction $2Cl + M \rightarrow Cl_2 + M$, for which rate coefficient expressions for forward and backward reactions were formulated separately according to Baulch et al. [127]. The activation energies for the reverse reactions were computed using the equilibrium constants of the involved reactions based on the thermochemical data from the JANAF tables [128]. Complementary quantum chemical calculations have been performed to improve the confidence in some particular rate expressions of selected reactions used in our kinetics mechanism [116].

The first question addressed was the energy needed for subsequent dissociation of Cl atoms from CCl_4. From the literature it is not entirely clear if the dissociation of the first Cl atom is energetically or kinetically easier than that of the second Cl atom. Because it has been reported that C-Cl dissociation is slower in CCl_3 than in CCl_4, one may conclude that the energy of the C-Cl bond is larger in CCl_3 than in CCl_4. Nevertheless, according to the JANAF thermochemical tables [128] it should be the other way round with tabulated C-Cl bond energy of 293.5 kJ/mol for CCl_4 and 276.8 kJ/mol for CCl_3. In Ref [116], the electronic ground state energies and the enthalpies of formation of CCl_x (x = 0–4) species were calculated. The reaction enthalpy for C-Cl bond breaking at T = 0 K has been calculated to 282.8 kJ/mol for CCl_4 and 276.9 kJ/mol for CCl_3 and are in good agreement with the JANAF tables. Taking into account four-fold reaction degeneracy in CCl_4 compared to a threefold one in CCl_3, it is plausible that C-Cl dissociation from CCl_4 could even be faster than in CCl_3 despite the slightly more favorable energetics in the latter case. In addition, for the C-Cl dissociation in CCl_2, corresponding values of 325.5 and 407.7 kJ/mol for CCl, were calculated, respectively.

Furthermore, based on the results of Michael et al. [129] who performed experiments using ARAS and schlieren techniques, simulations were performed with their high-pressure and low-pressure rate data for the following reaction as guidance.

$$CCl_4 + M \rightarrow CCl_3 + Cl + M \qquad \text{(R4.1)}$$

It was found that this rate has no influence on the detected species concentration profiles for the experimental conditions investigated here (see Table 4.1). However, for consistency, all subsequent simulations were performed with the rate reported in ref. [119] who used high-pressure rate coefficients. The *ab initio* calculated data in Ref. [116] of 282.8 kJ/mol are in good agreement with the activation energy of 288.2 kJ/mol in the high pressure limit (published in ref [129]) and the value of 286 kJ/mol, finally used in our kinetics simulations and also assumed in Ref [120] (see appendix 8.1).

A sensitivity analysis was performed to determine the rate-limiting reactions that are important for the formation and depletion of CCl_4. Figure 4.2 shows the results of the sensitivity analysis at 1460 K and a total pressure of 1.4 bar for a mixture containing 0.5% CCl_4 and 0.5% Ar in Ne for reaction times of 50 µs. The analysis shows the overwhelming importance of the bimolecular reaction $CCl_2 + CCl_2 = C_2Cl_2 + 2\ Cl$ for CCl_4 decomposition. This reaction, as reported in Ref [117], is a (non-elementary) two-step reaction whose rate had been determined from ARAS measurements at dilute conditions as 5.4×10^{14} exp(−7641 K/T) cm^3/mol s.

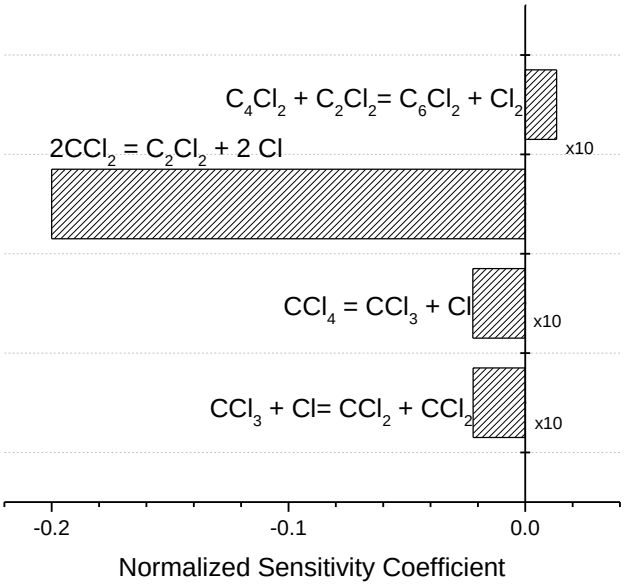

Figure 4.2: Normalized sensitivity analysis for CCl_4 at T_5 = 1460 K, p_5 = 1.4 bar, $x(CCl_4)$ = 0.5% and 50 µs of reaction time.

The second question addressed was the energy profile of the overall reaction sequence $C_2Cl_2 \rightarrow C_2Cl + Cl \rightarrow C_2 + 2\ Cl$. A reaction enthalpy of 824.8 kJ/mol for the overall process $C_2Cl_2 \rightarrow C_2 + 2\ Cl$ was calculated. However, it should be noted that the above calculated activation energies for $CCl_4 \rightarrow CCl_3 \rightarrow CCl_2 \rightarrow CCl$ as well as for the subsequent reactions $C_2Cl_2 \rightarrow C_2Cl + Cl \rightarrow C_2 + 2\ Cl$ do not significantly influence the calculated profiles of Cl_2, C_2Cl_2, and

CCl_4 of the current mechanism compared to corresponding activation energy taken from the literature [117]. The experimental data were compared with the simulation data of the reaction mechanism developed for CCl_4 decomposition. Simulations were performed for adiabatic conditions, constant volume and constant energy, using CHEMKIN [103] and thermodynamic data of Burcat [130].

Mass spectra from two experiments at 1210 and 1460 K for the mixture containing 1% CCl_4 and 0.5% Ar in Ne are presented in Figure 4.3 and Figure 4.4. In both cases averages of five ionization cycles at pre-shock conditions (blue upward) and a single cycle ionization spectrum at post-shock conditions at 200 µs behind the reflection of the shock wave (red downward) are presented. The mass spectrum in Figure 4.4 shows that besides the species discussed here, only C_2Cl_4 and ionization-related fragments are present. A comparison between Figure 4.3 and Figure 4.4 shows that product formation at low temperature is slower and nearly no products can be observed at approximately 200 µs at low temperature, as opposed to higher temperatures.

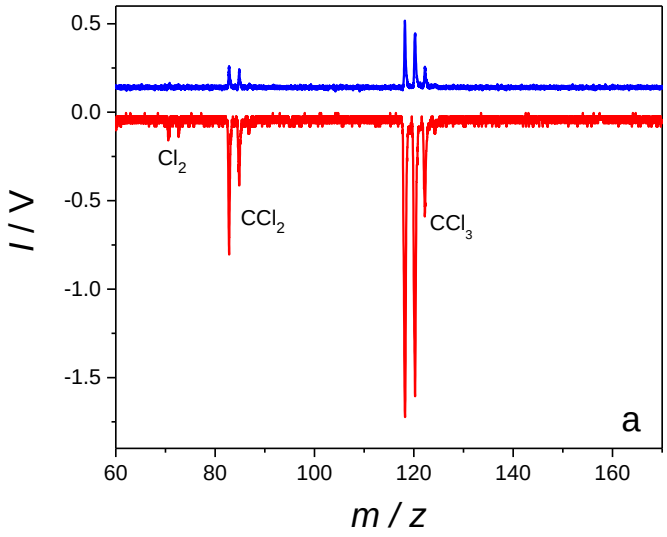

Figure 4.3: Mass spectra from an experiment at T_5 = 1210 K and p_5 =1.95 bar.
Top spectra (blue): Average of five ionization cycles at pre-shock conditions.
Bottom spectra (red): Single-cycle ionization spectrum at 200 µs after shock arrival.

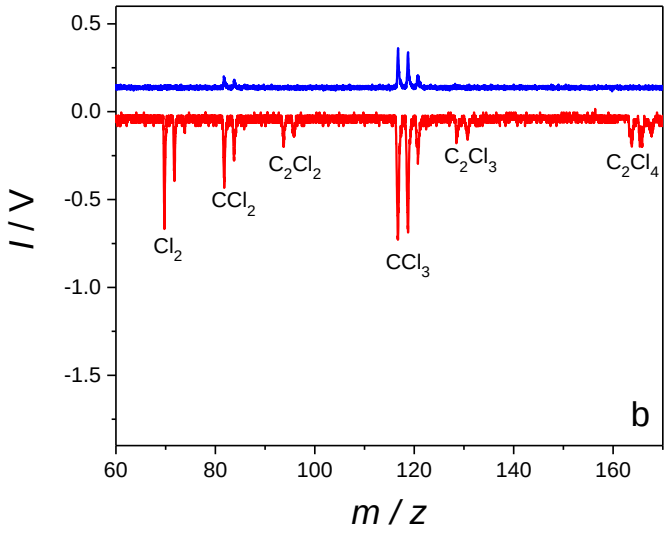

Figure 4.4: Mass spectra from an experiment at T_5 = 1460 K and p_5 =1.76 bar.
Top spectra (blue): Average of five ionization cycles at pre-shock conditions.
Bottom spectra (red): Single-cycle ionization spectrum at 200 µs after shock arrival.

From the raw data, peak area-time profiles were extracted for Cl_2, C_2Cl_2, and CCl_3 by summing their peak areas for the corresponding isotopologues (arising from the ^{35}Cl and ^{37}Cl isotopes, which have a relative abundance of 3:1). The other peaks did not have a sufficient signal-to-noise ratio or could not reliably be identified due to overlap of several species with the same *m*/*z* ratio due to fragmentation. Several species might contribute to the peak at *m*/*z* = 117 ($^{12}C^{35}Cl_3$). This mass represents both CCl_3 itself (formed by chemical reactions) and the most dominant CCl_4 fragment (i.e., CCl_3 formed in the TOF from dissociative ionization). Furthermore, potentially heavier species could also produce CCl_3 fragments (see discussion later). Thus, any analysis concerning this peak can only be qualitative.

Figure 4.5 shows a comparison of experimental data of CCl_3 + CCl_4 with results of the simulation based on the kinetics model for the mixture of 1% CCl_4 and 0.5% Ar in Ne between 1210 and 2385 K [131]. The symbols represent measured time-dependent peak intensities of CCl_3 and CCl_4 and the lines represent the simulated temporal profiles of the sum of the calculated concentrations for CCl_3 and CCl_4. Due to the instability of CCl_4, no peaks of CCl_4 were detected and the first detected peak that represents CCl_4 is the peak of CCl_3. In the evaluation of CCl_3, the sum of the peak intensities at *m*/*z* = 117 ($^{12}C^{35}Cl_3$) and *m*/*z* = 119 ($^{12}C^{35}Cl_2{}^{37}Cl$) was considered. Considering that the CCl_3 and CCl_4 have identical calibration factor, the CCl_3 peaks were weighted with the known concentration of the CCl_4 and depicts the sum of CCl_3 and CCl_4.

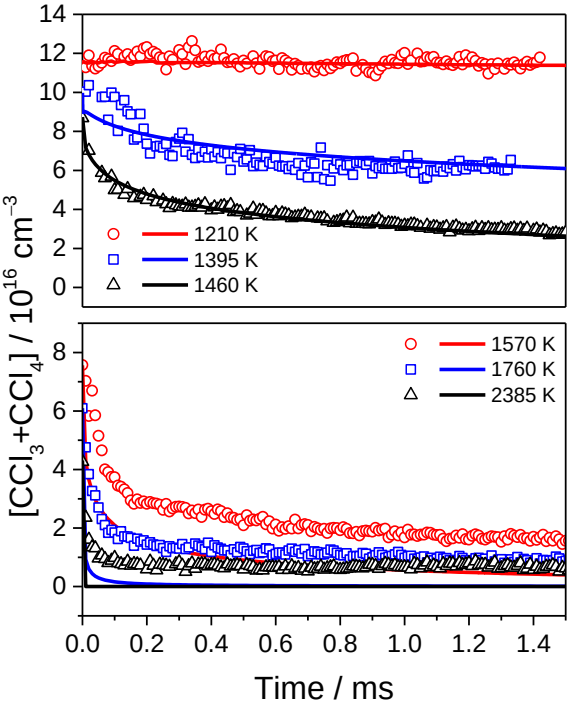

Figure 4.5: Temporal variation of the CCl_3+CCl_4 signal. Symbols: Experimental data, lines: Simulation (sum of CCl_4 and CCl_3) [131].

At low temperatures (1000–1460 K) the measured intensity profiles are well described by the kinetics model. However, at higher temperatures the model predicts fast total decomposition of CCl_4 and CCl_3, and all considered chlorinated species up to C_2Cl_6. Therefore, at higher temperatures it is not expected to detect signals at m/z = 117 ($^{12}C^{35}Cl_3$) and 119 ($^{12}C^{35}Cl_2{}^{37}Cl$) within the given time resolution. The nature of these species cannot be clarified based on the experiments but it can be concluded that the presence of the m/z = 117 and 119 signals is strong evidence for the presence of higher carbon chlorides (C_4Cl_6, C_6Cl_6 and etc.) which are predicted by the kinetics model.

To find an explanation for the discrepancy between measured and simulated CCl_3+CCl_4 profiles at high temperature, the reliability of the measured final values at high temperature was checked by considering the measured Cl_2-concentration profiles that are affected by minor experimental errors only. The comparison of the measured Cl_2 concentration profiles at 1460 and 2385 K shows that at 2385 K temperature almost twice the Cl_2 concentration was produced in comparison with 1460 K, as it can be seen in Figure 4.6. Thus, with respect to the Cl mass balance, at least double amounts of CCl_4 should have been consumed at 2385

K compared to 1460 K (in fact, even more than double amounts because a part of the chlorine atoms in CCl_4 reacts to Cl and C_2Cl_2, chlorinated polyyenes, C_xCl_y radicals, etc.).

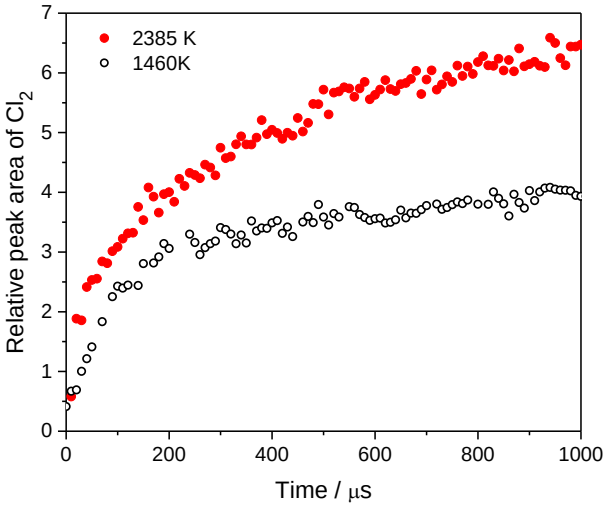

Figure 4.6: Temporal variations of the Cl_2-intensity signals at T_5 = 1460 K, p_5 = 1.76 bar (open circles) and T_5 = 2385 K and p_5 = 1.42 bar (full circles) for the mixture containing 1% CCl_4 and 0.5% Ar in Ne showing the signal increase of almost a factor of two when increasing the temperature by 1000 K.

To determine the amount of CCl_4 which is consumed at 1460 K, the experimental CCl_3 + CCl_4 and simulated curve at 1460 K are compared. Both are in good agreement as seen in Figure 4.5. The calculated initial CCl_4 concentration at this temperature was found to be reduced by almost a factor of two at the final reaction time. At 2385 K, the model predicts that CCl_4 is reacted away essentially completely after 200 µs. In contrast, in the experiment at this temperature, a non-zero level of [CCl_3+CCl_4] signal was found after an initial rapid decay. This plateau most likely represents the formation of more complex carbon chlorides that fragment to CCl_3 after ionization. This observation is in good agreement with the analysis of particles formed during CCl_4 pyrolysis at various temperatures found in an earlier study [132]. Furthermore, in Ref. [124] only at temperatures above 2500 K the particles were found to consist of pure carbon, whereas at lower temperatures (1900–2500 K) significant amounts of Cl_2 were detected. Thus, we assume that at low temperatures, complex carbon chloride clusters form by aggregation of simpler species.

The comparison of simulated and measured time profiles for the two major reaction products Cl_2 and C_2Cl_2 is presented in Figure 4.7. The contribution of higher carbon chloride fragments on the C_2Cl_2 peak is negligible. C_2Cl_4 was also detected but was not further analyzed because of the additional contribution from fragmentation of higher carbon chlorides.

In Figure 4.7, both signals for Cl_2 and C_2Cl_2 were normalized with regard to their maximum values of all experiments and calculations. Thus, one could compare not only the characteristic times in the presented profiles, but also the change of relative concentrations with temperature. Satisfactory agreement is observed for Cl_2 and C_2Cl_2 at temperatures between 1500 and 2100 K. Formation of both species become faster with increasing temperature in the 1400–1800 K range due to more rapid CCl_4 decomposition. At 1900 K the formation of Cl_2 becomes slower due to the increasing role of the reverse reaction $Cl_2 + M \rightarrow 2\ Cl + M$.

In conclusion, the experimental results support the suggested kinetics scheme for CCl_4 pyrolysis. The mechanism (Appendix 8.1) is based on reversible reactions employing thermodynamics to calculate the rate expression for the reverse reaction, with the exception of the $2\ Cl + M \rightarrow Cl_2 + M$ reaction whose rate expressions for forward and reverse reaction were treated separately. This assumption led to an improved agreement between measured and calculated values for Cl_2 concentration-time profile at higher temperatures. It is not clear why the equilibrium between Cl_2 and Cl is not established. It is assumed that surface reactions of Cl_2/Cl at the carbonaceous surface act as a sink for Cl or Cl_2 as is known from similar systems [133]. Accordingly missing reactions of Cl and Cl_2 with higher molecular weight products in the mechanism can lead to the observed effect.

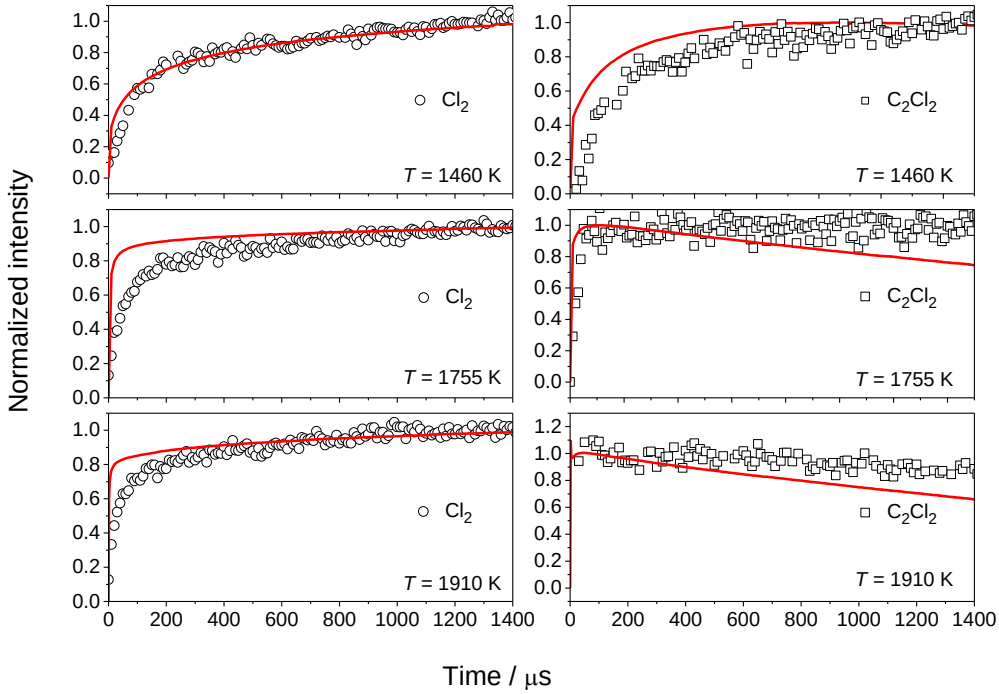

Figure 4.7: Temporal variation of the Cl_2 and C_2Cl_2 signals at various post-shock temperatures. Symbols: experimental data, lines: Simulations. The signals are normalized to the maximum values [131].

To illustrate the influence of the reverse reaction rate of the reaction 2 Cl + M → Cl_2 + M on the predicted species profiles, Figure 4.8 exhibits the calculated concentration profiles of (CCl_3+CCl_4), C_2Cl_2, and Cl_2 normalized to argon at 1650 and 2080 K assuming either reversibility for reaction 2 Cl + M ⇌ Cl_2 + M (case 1, dashed line) or considering forward and reverse reactions with reaction coefficients from this work separately (case 2, solid line). At low temperatures (Figure 4.8a), both cases give similar results for all species. Thus, the predictions remain unaffected by the reverse reaction rate. In contrast, at 2080 K (Figure 4.8b), the simulation shows an increased Cl_2 concentration (roughly about 20%) for case 2 compared to simulations assuming an irreversible reaction. However, even at this high temperature, the influence of the rate of the reverse reaction on the predicted concentrations of the species (CCl_3 + CCl_4) and C_2Cl_2 is small. Thus, the influence of the reversibility of reaction on the role of the possible growth species C_2Cl_2 or C_2 for carbonaceous material will be of less importance as well.

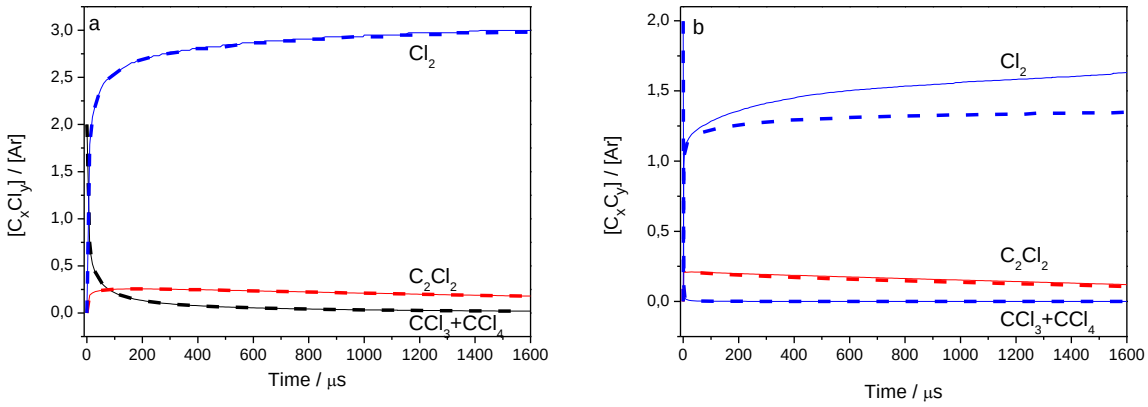

Figure 4.8: Calculated species concentrations profiles of CCl_4, C_2Cl_2 and Cl_2 at two temperatures of 1650 K (left) and 2080 K (right) assuming two different 'reversible' scenarios. The first (dashed lines) given by the reversibility of the forward reaction and knowledge of the corresponding equilibrium constant due to thermodynamics and second (solid lines, this work) [131] separate forward and reverse reactions for 2 Cl + M → Cl_2 + M.

To achieve deeper insight into the kinetics during the pyrolysis of CCl_4, a reaction-flow analysis was performed. The formation of C_2Cl_2 during CCl_4 pyrolysis is important for understanding the processes of small carbon cluster growth and the following carbonaceous particles formation. As deduced from this analysis, the concentration of C_2Cl_2 decreases due to its consumption by the formation of chlorinated polyynes and by carbon clusters via C_n + C_2Cl_2 → C_{n+2} + Cl_2. The simulations for the temperatures investigated here show that the main channel towards carbon cluster formation results from the reactions of C_2Cl_2 and the polyynes leading to Cl and Cl_2 elimination: CCl_4→ CCl_2 → C_2Cl_2 (→ chlorinated polyynes) →

C clusters. Thus, the growth of carbon clusters via C_2 addition to produce carbonaceous material that is postulated in Refs. [108, 125] for C_3O_2 pyrolysis seems to be negligible for our reaction conditions. This conclusion is in line with the observation of Frenklach et al. [109] who noted that carbonaceous powder produced from shock tube pyrolysis of CCl_4 at high temperature was not dark colored, as usual soot particles, but had a light color "off-white-gray" – revealing different mechanisms to solid carbon formation with features different from soot.

4.1.3. Conclusions

The temporal variation of CCl_4 + CCl_3, C_2Cl_2, and Cl_2 concentrations in the process of pyrolysis of CCl_4 was experimentally observed behind reflected shock waves with a high-repetition-rate time-of-flight mass spectrometer. The data obtained allowed to compile a kinetics model for CCl_4 pyrolysis. For parts of the model, quantum chemical calculations were performed to evaluate the bond dissociation energies in the CCl_4 system. Supported by the fact that no evidence of the C_2 dimer was experimentally found during CCl_4 pyrolysis, the reaction flow analysis of the simulations indicated that the reaction sequence to carbonaceous material in CCl_4 pyrolysis proceeds via $CCl_4 \rightarrow CCl_2 \rightarrow C_2Cl_2 \rightarrow$ chlorinated polyynes $\rightarrow C_n$ whereas the further addition of C_2Cl_2 to C_n was found to be the key step in cluster formation at the reaction conditions investigated here.

4.2. Pyrolysis of carbon suboxide (C_3O_2)

4.2.1. Motivation

The aim to reduce soot formation in combustion processes and to synthesize carbonaceous nanostructures with tailored properties motivated the investigation of the hydrogen-free carbon-particle precursor carbon suboxide (C_3O_2, O=C=C=C=O) in several experimental and modeling studies during the past decades [105, 108, 134-137]. Demchuk et al. [134] studied the gas phase reaction of hydrogen atoms with C_3O_2 in the temperature range of –96–235°C. They detected CO, CH_4, C_2H_2, and ketene as products. They also observed some black residue, which was concluded to potentially be carbon and/or polymer. They also proposed a mechanism and attributed the chain reaction to intermediate formation of ketene (CH_2CO) and formyl radical (HCO). The rapid reaction of ketene with H atoms produces CO and CH_4. The formyl radicals also react with C_3O_2 and produce CO. In 1999, Dörge et al. [135] studied the pyrolysis of the carbon suboxide behind reflected shock waves at temperatures ranging from 1200 to 2400 K and at a pressure of 54 bar. They followed the formation of soot parti-

cles by laser light extinction measurements at 632.8 and 1064 nm and studied the shape of the soot particles with electron microscopy. They showed that the induction times are shorter and the particle growth rate constants are higher than those obtained for soot formation from methane (CH_4) and benzene (C_6H_6). Their study also revealed that the soot yield does not depend on the C_3O_2 mole fraction and had its maximum at around 1600 K. The electron micrographs of the particles were similar to those of soot particles formed from hydrocarbons [135].

Friedrichs et al. [108] investigated the thermal decomposition of carbon suboxide (C_3O_2) behind shock waves in the temperature range from 1750 to 2300 K with mixtures containing 7 to 46 ppm C_3O_2 in Ar using C-atom-resonance-absorption spectroscopy (C-ARAS) at 156.1 nm. The C-atom concentration-time profiles exhibited short induction times from 10 to 50 µs. After an increase in the profile a plateau in the C-atom concentration was reached. Higher plateau values for the C-atom concentrations were found when increasing the temperature, but keeping the initial concentration of C_3O_2 constant. A sensitivity analysis for an experiment with initial concentration of 13 ppm C_3O_2 at 2100 K revealed that in the beginning of the thermal decomposition of C_3O_2 the following reactions are the most important ones for describing the C-atom concentration.

$$C_3O_2 + M \rightarrow C_2O + CO + M \quad \text{(R4.2)}$$

$$C_2O + M \rightarrow C + CO + M \quad \text{(R4.3)}$$

Reaction (R4.3) is important only during the induction time but reaction (R4.2) is the dominant reaction during the first 100 µs. After that reaction (R4.4) becomes as important as reaction (R4.2).

$$C_3O_2 + C \rightarrow \text{Products} \quad \text{(R4.4)}$$

A likely product of the reaction (R4.4) is C_2 from the following reaction.

$$C_3O_2 + C \rightarrow C_2 + 2CO \quad \text{(R4.5)}$$

They also measured the rate constants of the C_3O_2 decomposition.

Sojka et al. [136] presented an efficient discrete Galerkin method [138], the mathematical method for the solution of ordinary differential equations of heterogeneous polyreaction kinetics, to compute solid particle formation from gas phase species and applied the technique to model the formation of soot-like and fullerene-like solid particles during thermal

decomposition of C_3O_2 [136]. They calculated the concentration-time profiles for all gas-phase products and also solid carbon particles at temperatures ranging from 1200 to 2250 K.

Starke et al. [105] studied the formation of the carbonaceous particles from C_3O_2 behind reflected shock waves in the temperature range of 1400–3200 K and pressures of 1.3–4.5 bar. They measured the appearance of the particles by laser light extinction using a He/Ne laser at λ = 632.8 nm and laser-induced incandescence (LII) using the Nd:YAG laser at λ = 1064 nm. The double bell-shaped temperature dependence of the normalized optical density was observed by extinction experiments. The second bell at high temperature is only observed in pyrolysis of hydrogen-free precursors and either occurs because of particles with other formation mechanism than the particles of the first bell or particles with different optical properties. Additionally, the LII experiments showed the double bell-shaped dependence of the particles mean diameter to the temperature and confirmed their optical density experiments [105].

In 2005 Wen et al. introduced the fixed sectional aerosol dynamics model to investigate carbonaceous nanoparticle formation during the pyrolysis of C_3O_2 behind reflected shock waves in the temperature range of 1200–3800 K [137]. Their model successfully predicted the characteristics of nanoparticle formation in shock tubes, including induction time, growth rate, and particle yield in comparison with the experimental data of Sojka [136]. The predicted time dependence of the particle yield was in a good agreement with the measured optical density and the averaged particle diameters were in reasonable agreement with the particle size measured with LII [139] and TEM (transmission electron microscopy) [140]. They also investigated the temperature dependence of the particle properties, i.e., particle yield, total particle number density and average particle size as a function of temperature. The double bell-shaped profile for the particle yield and average particle diameter was found for the mixtures containing 0.33 and 1% C_3O_2. The first peak at around 1600 K was attributed to the largest particles nucleation and surface growth effect while the second peak at around 2700 K according to the almost constant particle number densities at this temperature could be because of the larger mass increase in the surface growth process. The drop at around 2300 K was discussed to be because of the decreased particle nucleation and surface growth processes.

The studies carried out so far addressed the determination of rate constants of the C_3O_2 decomposition, the induction times of particle formation, the rate constants of particle formation, as well as time-resolved measurements of particle volume fractions, and particle diameter. However none of the previous studies was based on detailed experimental data of

the concentrations of reactants, products, and intermediates during C_3O_2 decomposition. In this study the pyrolysis of the carbon suboxide was studied behind reflected shock waves using TOF-MS and the absolute concentration profile of the reactant (C_3O_2) and products are measured simultaneously.

4.2.2. Results and discussion

The thermal decomposition of carbon suboxide (C_3O_2) was investigated at temperatures between 950 and 2185 K and pressures between 1.0 and 2.0 bar using mixtures containing mole fractions of 0.4 or 1% C_3O_2, and 1% Kr as an internal standard with Ne as the bath gas. Carbon suboxide was synthesized in the laboratory of inorganic chemistry at the University of Duisburg-Essen following a modified synthesis procedure based on the work of Stock and Klemenc [141, 142]. As initial, substances malonic acid bis(trimethylsilylester) ($C_9H_{20}O_4Si_2$) and phosphorus pentoxide (P_4O_{10}) were used. The purity of C_3O_2 was checked with FTIR and there were no impurities such as CO_2 in the mixture. C_3O_2 has been routinely degassed by vacuum pumping at liquid nitrogen temperature. To avoid degradation and polymerization effects of C_3O_2 in the prepared mixture, mixtures were renewed every day. The experimental conditions are shown in Table 4.2.

Table 4.2: Experimental conditions for C_3O_2 pyrolysis.

Composition	Pressure / bar	Temperature / K
0.4% C_3O_2 + 1% Kr + Ne	1–1.75	1360–2185
1% C_3O_2 + 1% Kr + Ne	1–2	950–2005

According to the global reaction for high temperature conditions,

$$C_3O_2 \rightarrow 2CO + C \qquad \text{(R4.6)}$$

the decomposition of one molecule C_3O_2 produces two CO molecules and one carbon atom [40]. Thus, it was useful to focus on the concentration-time profiles of C_3O_2 and its major decomposition product.

In this section, the evaluation procedure of the mass spectra is presented in more detail. Because C_2O has the same nominal mass as argon (m/z = 40), krypton was used as an internal standard instead of Ar used in the experiments described before. A mass spectrum of the noble gas mixture containing C_3O_2 at room temperature is shown in Figure 4.9. The peaks at m/z = 82, 83, 84, and 86 are related to isotopes of Kr. The peaks at 12, 24, 28, and 40 are for C, C_2, CO, and C_2O respectively, which are the dissociative ionization products of C_3O_2. The

spectrum shows that C, C_2, and CO are formed as fragmentation products of C_3O_2 during ionization and also as decomposition product of C_3O_2 in the thermally-activated reaction. Thus in kinetics measurements, the effect of fragmentation must be corrected.

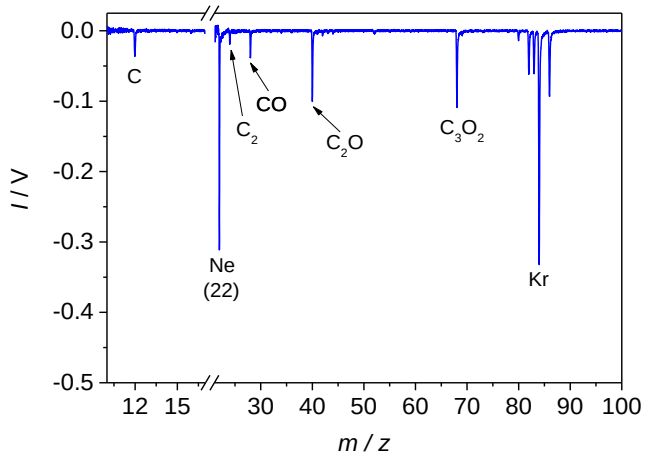

Figure 4.9: Mass spectrum of a C_3O_2/Kr/Ne gas mixture at room temperature. The energy of the ionizing electrons was 50 eV.

For comparison, two mass spectra of C_3O_2 are plotted in Figure 4.10a. The blue upward line represents the pre-shock conditions, and the red downward line depicts the mass spectrum 1 ms after the arrival of the reflected shock wave (T_5 = 1500 K, p_5 = 1.6 bar) for the mixture containing 0.4% C_3O_2 and 1% Kr in Ne. Figure 4.10b shows the same mass spectra that are normalized to the intensity of the C_3O_2 peak. The growth of the CO peak relative to C_3O_2 is better seen and confirms the CO formation during the dissociation of C_3O_2..

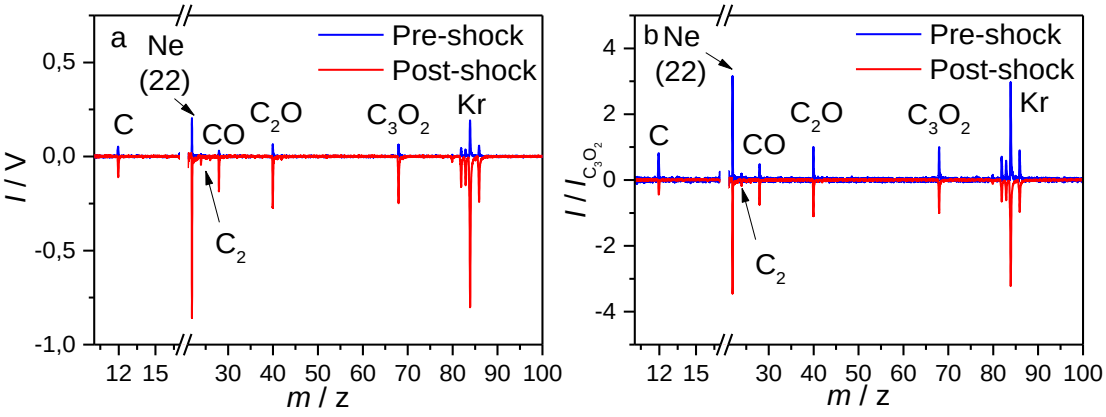

Figure 4.10: a) Mass spectra for pre-shock (solid line) and post-shock (dashed line) conditions. b) Mass spectra for pre-shock (solid line) and post-shock (dashed line) conditions normalized to intensity of C_3O_2 peak. The increase at m/z = 28 which is related to CO is noticeable. The energy of the ionizing electrons was 50 eV. The pre-shock spectrum is shown for better comparison.

Absolute concentrations of C_3O_2 and CO were obtained by calibration measurements for both species. The details about the calibration process defined in section (2.5.1.2). After defining the peak position for each species, the peak areas were integrated and related to the Kr signal as internal standard. This procedure was described in section 2.5. For calibration of both CO and C_3O_2, shock-heated mixtures at relatively low temperatures ($\approx 900 < T_5 < 1200$ K) and at pressures of p_5= 1– 2 bar were used. From the experiments with C_3O_2 at low temperatures where C_3O_2 does not decompose on the experimental time scale, the ratio of C, C_2, and CO over C_3O_2 was derived, which represents the part of C_3O_2 that is fragmented to C, C_2, and CO. This ratio was later used to correct the C, C_2, and CO profile by subtracting the fragmentation part.

Concentration-time profiles for C_3O_2 and CO are measured and calculated and compared with the simulation data based the model that was developed in our institute [131]. According to the work of Friedrichs and Wagner [108], a fast thermal decomposition of C_3O_2 generates CO, CCO, C, and C_2. The rate of the important reaction pathways are described in Table 4.3.

Induction times, rate constants of particle formation, and soot volume fractions for highly-diluted carbon-suboxide mixtures in argon at roughly 5 MPa could be successfully modeled by a reaction mechanism published by Sojka [126]. This mechanism included the reaction sequences (R4.2) to (R4.13) to simulate the gas-phase chemistry up to the carbon cluster C_{84}.

Carbonaceous species C_n with $n > 84$ were assumed to become solids and were modeled by a discrete Galerkin method [138]. The present study mainly relies on this mechanism. However, the cited mechanism underpredicted the induction times of carbon particle formation for carbon suboxide mixtures in the 1–33% C_3O_2 range at pressures in the 0.1–0.8 Pa range by nearly one order of magnitude. Therefore, the kinetics taken from Ref. [126] had to be improved according to Ref. [143].

Table 4.3: Modified and extended reaction mechanism for C_3O_2 pyrolysis addition. Rate coefficient $k = A\ T^n \exp(-E_a/RT)$.

No.	Reaction	A / cm^3 mol^{-1}	n	E_a / kJ mol^{-1}	Ref.
(R4.2)	$C_3O_2 + M \rightarrow CCO + CO + M$	2.00×10^{15}	0.0	2.45×10^{2}	[108]
(R4.3)	$CCO + M \rightarrow CO + C + M$	2.00×10^{15}	0.0	1.85×10^{2}	[108]
(R4.4)	$C_3O_2 + C \rightarrow$ Products	3.60×10^{14}	0.0	2.30×10^{1}	[126]
(R4.7)	$C_3O_2 + CCO \rightarrow$ Products	2.00×10^{15}	0.0	2.45×10^{2}	[108]
(R4.8)	$CCO + C \rightarrow C_2 + CO$	4.50×10^{11}	0.5	0.0	[126]
(R4.9)	$C_n + CCO \rightarrow C_{n+1} + CO$	4.50×10^{11}	0.5	0.0	[126]
(R4.10)	$C_n + C \rightarrow C_{n+1}$	4.50×10^{11}	0.5	0.0	[126]
(R4.11)	$C_n + C_2 \rightarrow C_{n+2}$	4.50×10^{12}	0.5	0.0	[126]
(R4.12)	$C_n + C_3O_2 \rightarrow C_{n+1} + CO + CO$	1.00×10^{13}	0.5	0.0	[126, 143]
(R4.13)	$C_n + C_m \rightarrow C_{n+m}$	1.00×10^{12}	0.5	0.0	[126]

The major improvements were as followed:

The reaction coefficient for reaction (R4.2) was set according to Ref. [108] to $k_{4.2} = 2.00\times10^{15}\exp(-29469\ \mathrm{K}/T)$ cm^{3}mol^{-1}s^{-1} and the rate coefficient for reaction (R4.3) was chosen according to [144] to $k_{4.3} = 2.00\times10^{15}\exp(-22249\ \mathrm{K}/T)$ cm^{3}mol^{-1}s^{-1}. One further essential change that was introduced is related to reaction type (R4.12), whereas in [126], C_3O_2 addition (R4.12) was only taken into account for carbon molecules C_n with $2 < n < 29$. In the present study, this reaction was extended up to carbon molecules C_n with $n \leq 84$, i.e., up to carbon clusters of a diameter of approximately 1 nm size. Carbonaceous species formation C_n with $n > 84$ was neglected here since this work is focused on the validation of the gas-phase chemistry of small species.

Thermochemical data from readily available sources [130, 145] were taken for all low molecular-mass species up to C_{12}. For the larger species C_n with $12 < n \leq 84$, thermodynamic data relied on Martin et al. [146], assuming that the corresponding data for C_{84} are equal to that of graphite. Deduced from work of Martin et al. [146], for the enthalpy of formation of the clusters C_n, $\Delta H_f(C_n)$, with $10 \leq n \leq 84$ in the gas-phase calculations, the relation $\Delta H_f(C_n) = \Delta H_f(C_{10})\ [0.025\ (n-10) + 1]$ was employed which for example results in $\Delta H_f(C_{84}) = 5985$ kJ mol^{-1} at 2000 K [146]. Simulations were performed for adiabatic conditions, constant volume and constant energy, using CHEMKIN [103] and thermodynamic data of Burcat [130].

Figure 4.11 shows measured and calculated concentration-time profiles for C_3O_2 and corrected CO that the part from C_3O_2 fragmentation is abstracted for the lowest temperature

examined for the mixture containing 1% C_3O_2 and 1% Kr in Ne. In agreement with the experiments, the simulations predict a negligible consumption of C_3O_2 and also no CO production at T_5 = 1170 K.

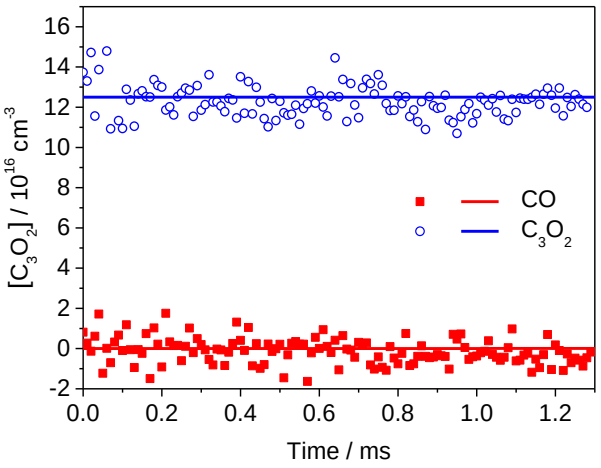

Figure 4.11: Concentration-time profiles for the post-shock region for an experiment at T_5 = 1170 K and p_5 = 2 bar with mixture containing 1% C_3O_2 and 1% Kr in Ne. Open circles are C_3O_2 and solid squares are corrected CO. Solid lines show the simulation [131].

With increasing temperature, the thermal decomposition of C_3O_2 proceeds as seen in Figure 4.12 for 1420 K and in Figure 4.13 for 1535 K. The agreement between simulations and experiments is reasonable, concerning the absolute values as well as for the shape of the curves for both CO and C_3O_2, although at 1420 K, the model predicts a slightly slower decay of C_3O_2, and consequently a too slow formation of CO compared to the measurement.

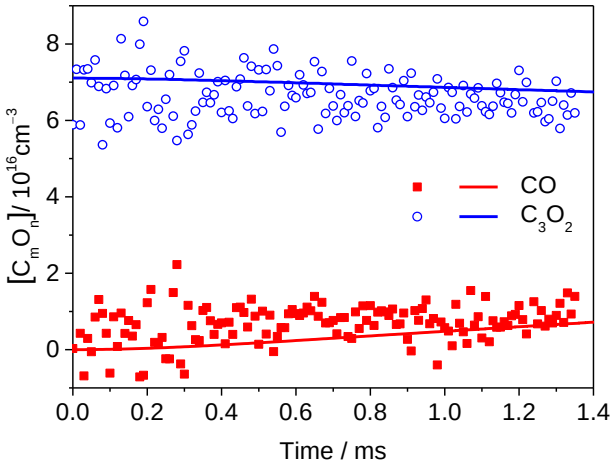

Figure 4.12: Concentration-time profiles for the post-shock region for an experiment at T_5 = 1420 K and p_5 = 1.55 bar with mixture containing 1% C_3O_2 and 1% Kr in Ne. Open circles are C_3O_2 and solid squares are CO. Solid lines show the simulation [131].

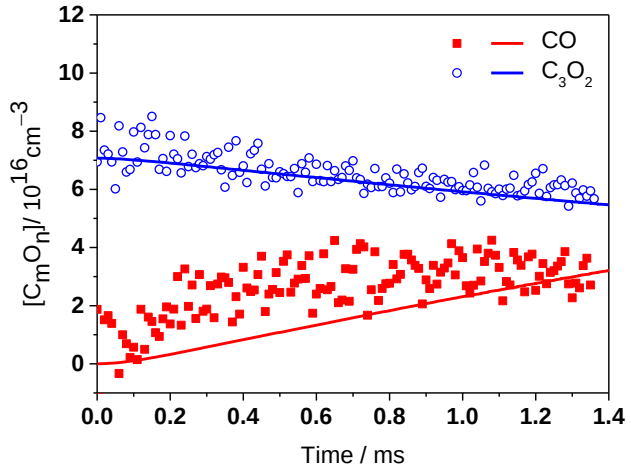

Figure 4.13: Concentration-time profiles for the post-shock region for an experiment at T_5 = 1535 K and p_5 = 1.5 bar with mixture containing 1% C_3O_2 and 1% Kr in Ne. Open circles are C_3O_2 and solid squares are CO. Solid lines show the simulation [131].

At even higher temperature (T_5 = 1630 K) shown in Figure 4.14, the simulations satisfactorily match the measurements up to reaction times of roughly 0.9 ms. At longer times, the discrepancy between both is more prominent, but still, simulated values agree with the measured ones within the experimental uncertainty in concentration calculation of 15%.

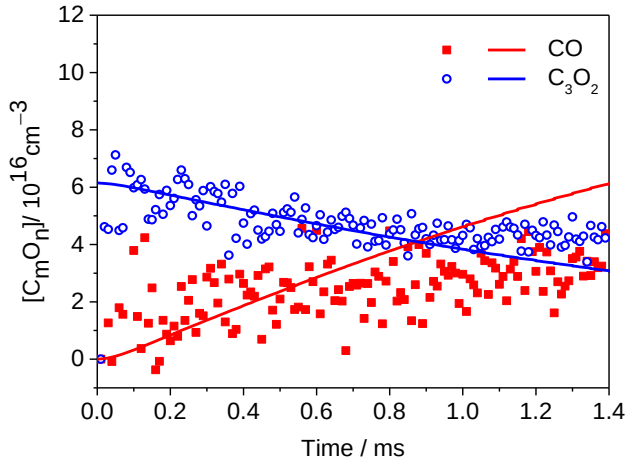

Figure 4.14: Concentration-time profiles for the post-shock region for an experiment at T_5 = 1630 K and p_5 = 1.4 bar with mixture containing 1% C_3O_2 and 1% Kr in Ne. Open circles are C_3O_2 and solid squares are CO. Solid lines show the simulation [131].

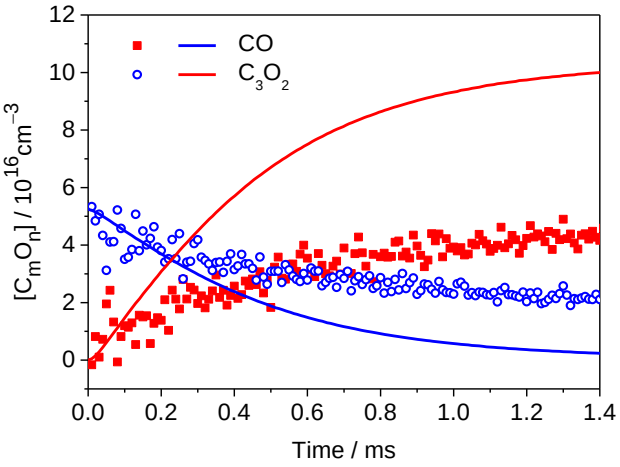

Figure 4.15: Concentration-time profiles for the post-shock region for an experiment at T_5 = 1790 K and p_5 = 1.3 bar with mixture containing 1% C_3O_2 and 1% Kr in Ne. Open circles are C_3O_2 and solid squares are CO. Solid lines show the simulation [131].

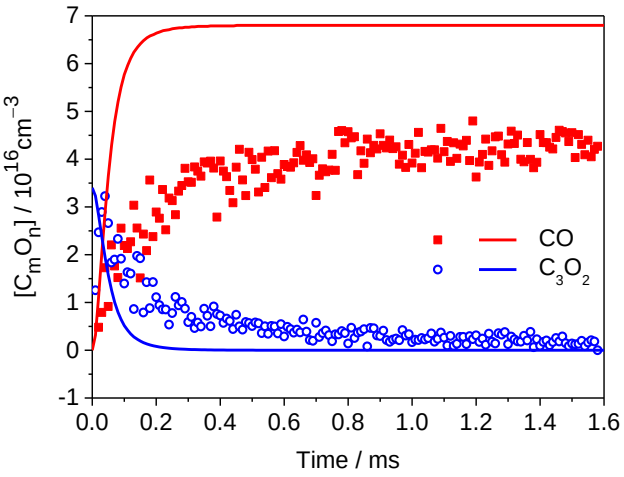

Figure 4.16: Concentration-time profiles for the post-shock region for an experiment at T_5 = 2005 K and p_5 = 0.95 bar with mixture containing 1% C_3O_2 and 1% Kr in Ne. Open circles are C_3O_2 and solid squares are CO. Solid lines show the simulation [131].

While at 1790 and 2005 K (Figure 4.15 and Figure 4.16, respectively), the shapes of C_3O_2 and CO profile were reasonably well described by the model, but the final concentration of CO was underpredicted by roughly a factor of 1.6. A closer inspection of the difference between modeled and calculated CO profiles indicates an unmatched oxygen balance at 2006 K in the experiment: roughly 2×10^{16} O atoms were missing per cm^3 at end-gas conditions which corresponded to approximately 30% of the initial oxygen concentration in C_3O_2. O was detected in the major product CO and the remaining C_3O_2 fraction which was not consumed during the experiments. In contrast, only negligible amounts of CO_2 and CCO were formed in the

experiments as confirmed by the model. Furthermore, no evidence of higher carbon oxides like $C_{8n}O_{2n}$ ($3 \leq n \leq 5$) was found experimentally in the mass spectra. Thus further research is required to identify the missing channels for oxygen consumption, such as its incorporation into large carbon clusters and carbon particles, respectively.

As it can be seen in reaction (R4.10) and (R4.11), C atoms and C_2 molecules are of special interest for the formation of carbon clusters and carbon particles. To examine the role of both species for the build-up of the C_n compounds, it was aimed to analyze the signals for C and C_2 in the corresponding spectra. Due to poor signal-to-noise ratios, only the maximum concentrations taken from the signal plateau at longer times were used for the following considerations. A direct calibration of the species concentrations was not possible. Therefore, relative concentrations of C *vs.* C_2 were deduced for the comparison with the model predictions.

The data evaluation is complicated because C and C_2 are also formed through fragmentation during electron impact ionization and thus interfere with the species generated through the thermal decomposition reaction of C_3O_2 and C_2O. Figure 4.17a and Figure 4.17b show the peaks of C and C_3O_2 and peaks of C_2, CO and C_3O_2 respectively and also the calculated peak area ratios at T_5 = 1170 K and p_5 = 2 bar averaged over all post-shock mass spectra for the mixture containing 1% C_3O_2 and 1% Kr in Ne. At this temperature the thermal decomposition of C_3O_2 is negligible and the peaks for C, C_2, and CO are mainly due to the fragmentation of C_3O_2. The given ratios in the graphs are used to separate the effect of fragmentation from those of chemical kinetics.

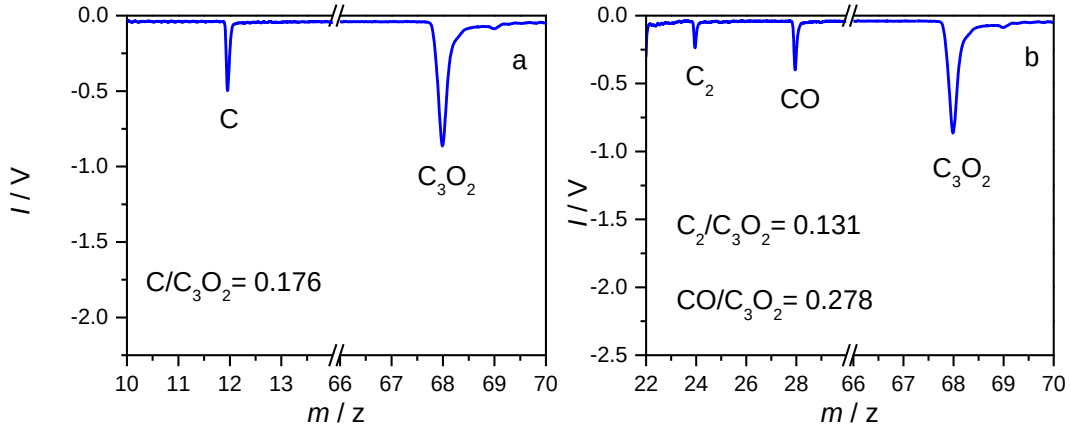

Figure 4.17: a) C and C_3O_2 peaks and peak area ratio at T_5 = 1170 K and p_5 = 2 bar averaged over all post-shock spectra. b) C_2 and CO peaks and peak area ratio at the same condition.

The data analysis with respect to C atoms and the increase of the C/C_3O_2 peak ratio due to C formation is displayed in Figure 4.18. In this figure the temporal C/C_3O_2 peak area ratios of all post-shock spectra at 2005 K and 0.94 bar is shown. The slope of the function ratio clearly shows an increase and hence implying C-atom formation.

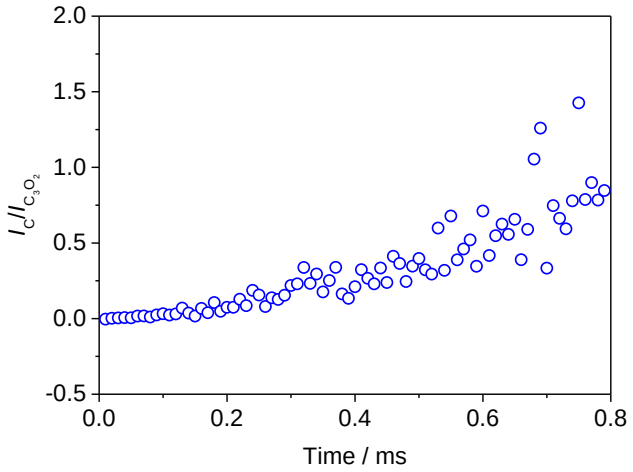

Figure 4.18: Temporal C/C_3O_2 peak area ratios at 2005 K and 0.94 bar.

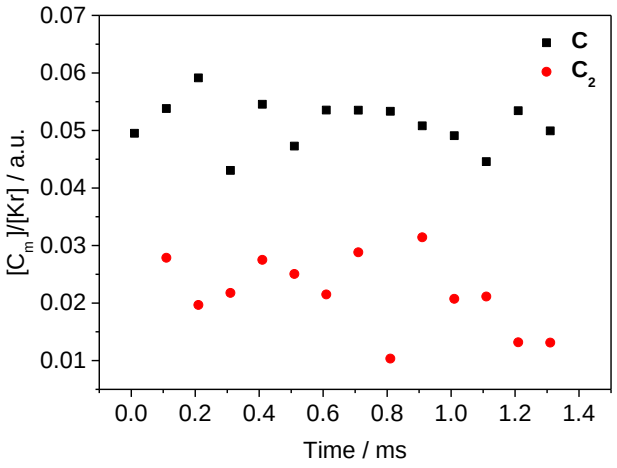

Figure 4.19: Relative C and C_2 concentration-time profiles at T_5 = 1675 K and p_5 = 1.4 bar.

Clear evidence for the presence of thermally-formed C and C_2 was found in the measurements and the increase of the C_n/C_3O_2 peak ratios observed therein. This conclusion is fully supported by the modeling calculations. In addition, in Figure 4.19, measured C and C_2 concentration profiles related to the Kr concentration are shown. Because calibration factors are not available for C and C_2, only arbitrary units can be given. To increase the signal-to-noise ratio of the respective signals it was necessary to average ten subsequent mass spectra, i.e.,

reducing the time resolution of the detection to 100 µs to deduce the concentrations. The resulting C and C_2 concentration ratios have an uncertainty of a factor of 2–3. The small variation in concentration over time justifies the approach to average all post-shock C and C_2 signal intensities before further evaluating the C/C_2 ratios.

Figure 4.20 illustrates the dependence of the ratio of the integrated concentration profiles of C and C_2 (C/C_2 concentration ratio) versus the temperature T_5 relative to the ratio measured at 1420 K, which was the lowest temperature that led to a considerable C_3O_2 consumption within the test time. In experiments and simulations, the C/C_2 concentration ratios increase with temperature whereas the simulation overpredicts this increase. When comparing measurements and simulations, it must be kept in mind that the signals for C and C_2 could interfere with those from fragments of larger carbon clusters. Nevertheless, the overall trend of increasing C/C_2 concentration ratios with temperature seemed to be reliable since it was observed in experiments and simulations. The simulations showed that the increase of the C/C_2 concentration ratio was due to a relative decrease of the C_2 concentration in comparison to that of C atoms. This leads to the conclusion that the relative contribution of C_2 to the formation of larger carbon clusters increases with temperature. To demonstrate the increasing concentration of large carbon clusters with temperature, the simulated normalized C_{84} integrated concentration profile is also given in Figure 4.20. Thus, reaction type (R4.11) was concluded to be more efficient for carbon cluster growth than channel (R4.10) which shows the contribution of C atom in carbon cluster formation.

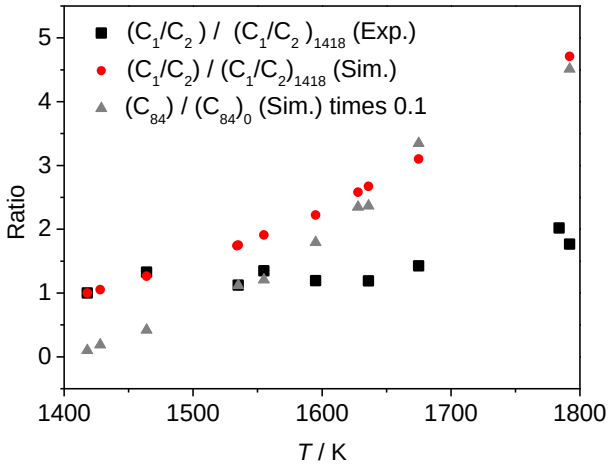

Figure 4.20: Measured and calculated ratio of C/C_2 normalized to the C/C_2 ratio at T_5 = 1420 K, and calculated carbon cluster concentration of C_{84} normalized with the C_{84} carbon cluster concentration at T_5 = 1420 K versus temperature T_5.

4.2.3. Conclusions

The decomposition of C_3O_2 behind reflected shock waves was examined by shock-tube experiments and kinetics simulations. For the first time, in shock tubes, concentration profiles for C_3O_2 and CO were simultaneously measured by HRR-TOF-MS as a function of time. The concentration-time profiles served as validation data for an improved kinetics model for C_3O_2 decomposition that incorporates the growth of carbon particles up to approximately 1 nm in diameter. The experimental results were in reasonable agreement with the model predictions for temperatures up to 1800 K. Thus, the actual studies could confirm the rate constant $k = 2.00\times10^{15}\exp(-29469\ \mathrm{K}/T)\ \mathrm{cm^3mol^{-1}s^{-1}}$ for the decomposition of C_3O_2 previously given in the literature [108]. Furthermore, the integrated concentration profiles of C atoms and C_2 molecules were detected and related to model predictions for these species and large clusters' concentrations. The resulting observations indicate that the C_2 addition channel is more important for carbon cluster growth compared to reactions with C-atom addition to the corresponding clusters.

4.3. Pyrolysis of acetylene (C_2H_2)

4.3.1. Motivation

Acetylene (C_2H_2, H−C≡C−H) is a major decomposition product of several hydrocarbons and plays an important role as a building block towards soot formation. Its thermal decomposition has been studied in a wide temperature range by several authors [92, 147]. In 1980, Frank and Just [147] studied the thermal decomposition of acetylene behind reflected shock waves in the temperature range of 1850–3000 K in diluted mixtures of acetylene (5–400 ppm) in argon by measuring H- ARAS. They showed that at 2000 K the H atom production by reaction (R4.14) is very small and $k_{R4.14}$ has almost no influence on H atom production. At 2500 K the rates of (R4.14) and (R4.15) are comparable, therefore reaction (R4.15) and $k_{R4.15}$ play significant role in H atom formation. But at 3000 K, the rate of H-atom production by reaction (R4.14) is much higher than by reaction (R4.15).

$$C_2H_2 + M \rightleftharpoons C_2H + H + M \qquad \text{(R4.14)}$$

$$C_2H_2 + C_2H \rightleftharpoons C_4H_2 + H \qquad \text{(R4.15)}$$

Wu et al. [92] studied the thermal decomposition of acetylene behind reflected shock waves in the temperature range of 1900–2500 K and pressures ranging from 0.3 to 0.55 bar using time-of-flight mass spectrometry. Diacetylene (C_4H_2) and triacetylene (C_6H_2) were detected

as major products of acetylene pyrolysis and concentration-time profiles for C_2H_2, C_4H_2 and C_6H_2 were plotted for the observation time of 750 µs. Neither higher polyacetylenes nor polycyclic aromatic hydrocarbons (PAHs) were detected in their experiments.

Ruiz et al. [148-150] have studied the soot yield from C_2H_2 and C_2H_4 pyrolysis and its properties in a flow reactor as a function of temperature, initial concentrations, and residence time.

Eremin et al. [151] published a detailed experimental study elucidating the role of hydrogen on particle growth behind shock waves where temperature, particle sizes and induction times were measured. It was found that the measured temperatures were similar for both cases (with and without H_2 addition) and that H_2 addition increases the induction times and decreases both the particle sizes and optical density of the soot-containing mixture.

All these studies have in common: They investigate the effect of molecular hydrogen where the main targets were soot particles in the late stage of formation. In shock tubes experiments the focus was also set on the effect of adding H_2 on the optical density of the reaction mixture, on particle sizes, as well as gas temperature. In the present work, the influence of H_2 on carbonaceous reaction intermediates that are important for soot precursor formation in acetylene pyrolysis has been studied in a shock tube. This study contributes to the understanding of soot formation in its early stage from the acetylene pyrolysis behind reflected shock waves by simultaneously time-resolved measuring of absolute concentrations of polyacetylenes which are considered as potential precursors leading to soot formation by using TOF-MS. The effect of hydrogen addition is also investigated to see if the presence of H_2 can inhibit or promote the soot formation. Additionally, a detailed kinetics model was developed to explain the experimental observations.

4.3.2. Results and discussion

In this study measurements were performed with two different concentrations (2 or 5%) of C_2H_2 in Ne. For the 5% case, the nozzle was frequently blocked after the experiments as a result of soot formation. A compromise between nozzle diameter and concentration of the precursor was chosen to avoid this issue. Therefore, most experiments were carried out with 2% C_2H_2 but some measurements with 5% were also included for those experiments where the nozzle was not blocked. For the measurements with H_2, mixtures of 2% and 5% C_2H_2 with 2 and 4% H_2 in Ne were prepared. All mixtures additionally contained 1% Ar as internal inert standard. The pyrolysis of acetylene (C_2H_2) was studied at temperatures between 1760 and 2565 K and pressures between 0.79 and 1.28 bar. The experimental conditions are given in Table 4.4.

Table 4.4: Experimental conditions for C_2H_2 pyrolysis

Composition	Pressure / bar	Temperature / K
2% C_2H_2 + 1% Ar + Ne	0.9–1.3	1855–2310
2% C_2H_2 + 2% H_2 + 1% Ar + Ne	0.9–1.5	1895–2410
2% C_2H_2 + 4% H_2 + 1% Ar + Ne	0.95–1.1	1995–2430
5% C_2H_2 + 1% Ar + Ne	0.95–1.1	1995–2430
5% C_2H_2 + 2% H_2 + 1% Ar + Ne	0.75–1.3	1950–2250
5% C_2H_2 + 4% H_2 + 1% Ar + Ne	0.75–1.2	1750–2300

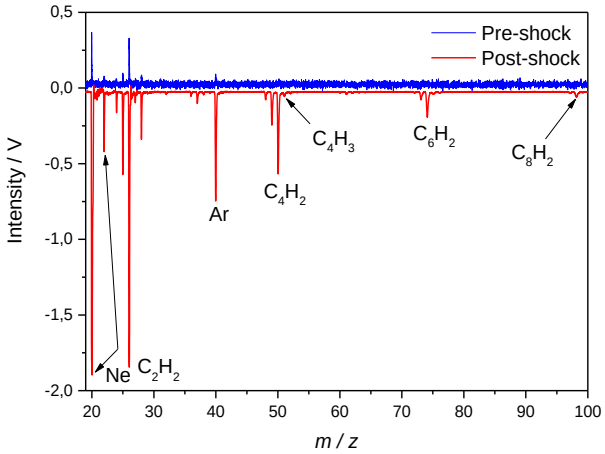

Figure 4.21: Mass spectra of a C_2H_2/Ar/Ne gas mixture for pre-shock (blue line) condition and post-shock (red line) condition at reaction time of 1 ms . Ionization energy was 45 eV. The pre-shock spectrum is shown inverted to facilitate comparison.

Figure 4.21 shows a pre-shock and a post-shock mass spectrum for an experiment with T_5 = 1995 K and p_5 = 1.08 bar with a mixture containing 5% C_2H_2 and 1% Ar in Ne. Blue upward signal is a pre-shock mass spectrum and exhibits the typical fragmentation pattern of C_2H_2 with electron-impact ionization. The red downward signal is a post-shock mass spectrum and the additional peaks visible at masses higher than m/z = 40 are associated with products of the thermal decomposition of C_2H_2. The post-shock spectrum shows signals that are attributed to higher polyacetylenes (C_4H_2, C_6H_2, and C_8H_2) which are the C_2H_2 pyrolysis products. The first aromatic structure (e.g., benzene), however, was not detected. The concentration of benzene is below the sensitivity of the apparatus (x_i = 1.7×10^{-4}) or (2.13×10^{15}cm^{-3}). This is in agreement with calculations that predict very small mole fractions of aromatic species ($x_{aromatic}$ < 10^{-8}). Only in the experiments with 5% C_2H_2, traces of C_4H_3 are found which is an important intermediate to form the first aromatic ring (forming phenyl via C_2H_2 addition) according to the following reaction:

$C_4H_3 + C_2H_2 \rightleftharpoons C_6H_5$ (Phenyl) (R4.16)

As stated before, for quantitative analysis of the signal intensities the TOF-MS must generally be calibrated for each species individually. This is doable only for stable species or for species where a reliable quantitative formation reaction is available. For other species, semi-quantitative data is available that provide reliable information about the temporal variation, but not absolute concentrations. To calibrate C_2H_2 in shock-heated measurements with known initial concentrations, studies are performed at relatively low temperatures where C_2H_2 does not decompose and signal intensities are converted to absolute concentrations. In case of polyacetylenes, however, diacetylene (C_4H_2) is explosive and not available commercially. Therefore, the calibration factors m ($I_i = mc_i$) for C_4H_2, C_6H_2 and C_8H_2 were determined by taking into account the calibration factor ratio of C_2H_2:C_4H_2:C_6H_2:C_8H_2 (1:2:3:4), where I_i and C_i are the intensity and the corresponding concentration of the species *i*. These factors are in line with the respective measured and calculated ratios of electron-impact-ionization cross sections from the NIST database [152] but are slightly different from the ratios adopted in Ref. [92]. The calibration factors for the stable species (C_2H_2) were determined according to the process that was described in chapter (2.5.1.2). The experimental data are compared with results of simulations based on two previous models [92, 147] as well as the model used in this work [153].

The Mechanism employed here has been validated in several publications before [136, 154-156]. The C_1 chemistry relies on the work of Sojka [126], the C_2 reactions are assembled from Heghes [157], while the core of the reactions of the C_3 to C_8 species follows the work of Böhm et al. [158]. The polyaromatic hydrocarbon chemistry as given by Frenklach et al. [5] for the HACA route, as well as PAH channels as proposed and validated by Böhm and Jander [159] and by Naydenova [160] for the incorporation of combinative steps of aryls (functional group or substituent derived from an aromatic ring, like phenyl which is derived from benzene) were employed. Besides, the C_2 channel for the growth of aromatic hydrocarbons as proposed by Gu et al. [161] with the rate coefficient from Becker et al. [162] for the mentioned reaction type are taken into consideration. The model also contains carbon-cluster formation for particles up to C_{84} as published in [163], with improvements as presented and validated in [143]. The calculations were performed under constant volume assumption using the CHEMKIN package [103]. The model describing polyacetylenes chemistry until $C_{12}H_2$ is presented in the appendix 8.2.

The measured concentration-time profiles are compared with simulations based on three kinetics models in Figure 4.22. Figure 4.22a shows a concentration-time profile for C_2H_2,

C_4H_2, and C_6H_2 during C_2H_2 pyrolysis for the mixture of 2% C_2H_2, 1% Ar, and 97% Ne at T_5 = 2005 K and p_5 = 1.20 bar. Figure 4.22b shows the corresponding profiles for the same mixture at T_5 = 2240 K and p_5 = 0.96 bar. At these conditions, acetylene is not completely consumed within the test time. The signal intensities of the polyacetylenes decrease with increasing molecular weight (C_4H_2 > C_6H_2 > C_8H_2) and reach a plateau at longer times. The examinations of concentration profiles with respect to the carbon mass indicate well-balanced species concentrations within the experimental uncertainties. Moreover, the maximum C_6H_2 concentration is 20 times smaller than the initial C_2H_2 concentration, which is in line with previous observations [92]. The Wu et al. [92] and Frank and Just [147] models predict an induction time for acetylene depletion and a concomitant later appearance of the products that is not observed experimentally. A model used in the present work shows no such induction time and is in significantly better agreement with the experiment. This trend is observed throughout the whole range of temperatures and reactant concentrations.

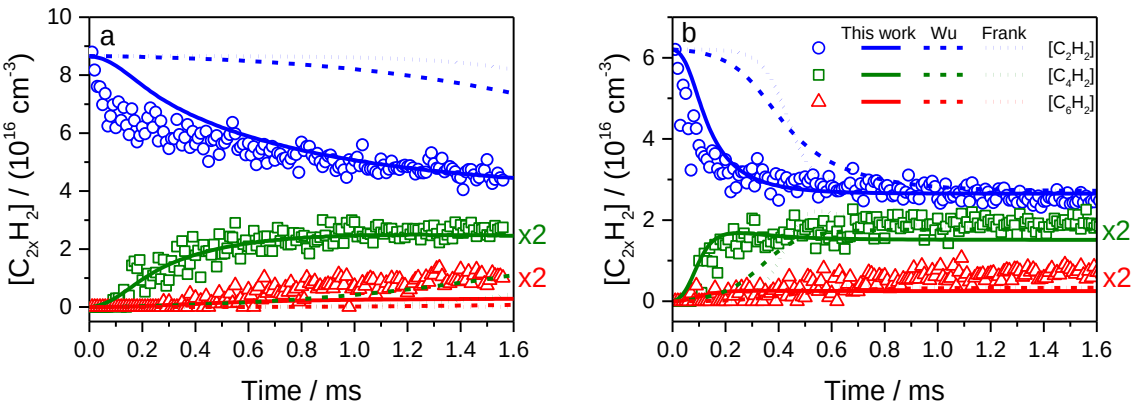

Figure 4.22: Measured (symbols) and simulated (lines) concentration-time profiles of the main species during C_2H_2 pyrolysis for the mixture containing 2%C_2H_2 and 1% Ar in Ne. Simulations based on the models from [92, 147] are compared with the model of this work. The repetition rate of ionization was 100 kHz and the ionization energy was 45 eV. a) T_5 = 2005 K and p_5 = 1.20 bar and b) T_5 = 2240 K and p_5 = 0.96 bar.

Figure 4.23a and b show the concentration-time profiles of the main species during C_2H_2 pyrolysis for the mixture containing 5% C_2H_2, 1% Ar, and 94% Ne respectively at T_5 = 1995 K and p_5 = 1.08 bar and T_5 = 2225 K and p_5 = 0.95 bar. By increasing the temperature from 2000 to 2240 K, the model predicts the start of depletion of acetylene during the first 500 µs with a better agreement compared to two other models [92, 147]. However the production of diacetylene (C_4H_2) is almost at all the temperatures well predicted by the model of this study, the production of hexatriyne (C_6H_2) is underpredicted by the same model and the production of octatetrayne (C_8H_2) is overpredicted by the model. Simulations based on all three models, however, agree with the experiment at longer reactions times.

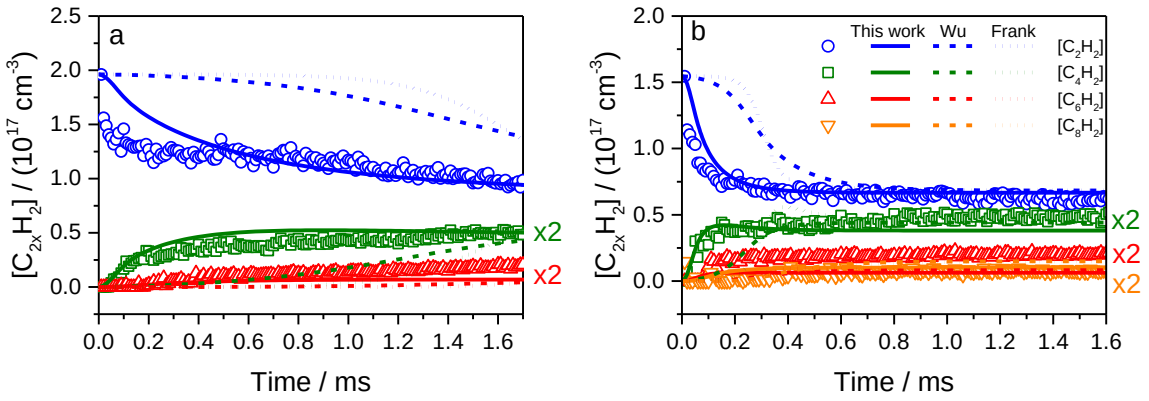

Figure 4.23: Measured (symbols) and simulated (lines) concentration-time profiles of the main species during C_2H_2 pyrolysis for the mixture containing 5%C_2H_2 and 1% Ar in Ne. Simulations based on the models from [92, 147] are compared with the model of this work. The repetition rate of ionization was 100 kHz and the ionization energy was 45 eV. a) T_5 = 1995 K and p_5 = 1.08 bar and b) T_5 = 2225 K and p_5 = 0.95 bar.

The influence of H_2 on the C_2H_2 decomposition chemistry is studied in mixtures containing 2 and 5% C_2H_2 with 2 and 4% H_2. Preliminary tests showed that the selected initial concentrations were the best choice to achieve an acceptable signal-to-noise ratio and to avoid blockage of the nozzle with soot particles. Using concentrations larger than 4% H_2 was not straightforward due to a strongly decreased consumption of C_2H_2 and consequently very low concentrations of polyacetylenes. Simulated concentration-time profiles are compared with the model of this study as it showed the better agreement in comparison with other available models at the wider temperature range.

Figure 4.24 shows concentration-time profiles for mixtures containing 2% C_2H_2 with three molecular hydrogen contents ($x(H_2)$ = 0, 2, and 4%) at approximately the same experimental conditions ($T_5 \approx$ 2245 K, $p_5 \approx$ 1.20 bar). In the presence of H_2, less C_2H_2 (almost 50% less than if H_2 is not added) is consumed and accordingly less diacetylene (C_4H_2) is produced. As it is observed in Figure 4.24 at 2245 K, with 2% H_2 added to the mixture, still a small amount of C_6H_2 is produced, but when increasing the amount of hydrogen to 4%, no C_6H_2 and C_8H_2 are detected (i.e., the concentrations are reduced at least by a factor of 50 compared to the cases without H_2). With no H_2 added, the C_2H_2 profile is well predicted by the model but with adding the H_2 to the mixture, there is a slight discrepancy between the experiments and simulation data. In the absence of H_2, the C_2H_2 profile at longer time is well predicted by the model of this study and there is small discrepancy at start of the reaction. By adding H_2 to the mixture there is a discrepancy between the experiment and model prediction for C_2H_2. At longer times, the discrepancy between both is more prominent, but still, simulated values

agree with the measured ones within the experimental uncertainty in concentration calculation of 15%. The C_4H_2 and C_6H_2, however, are well predicted by the model for all mixtures.

Figure 4.25 shows concentration-time profiles for mixtures containing 2% C_2H_2 without and with molecular hydrogen ($x(H_2)$ = 2, and 4%) at almost the same experimental conditions (T_5 ≈ 2315 K, p_5 ≈ 1.10 bar).

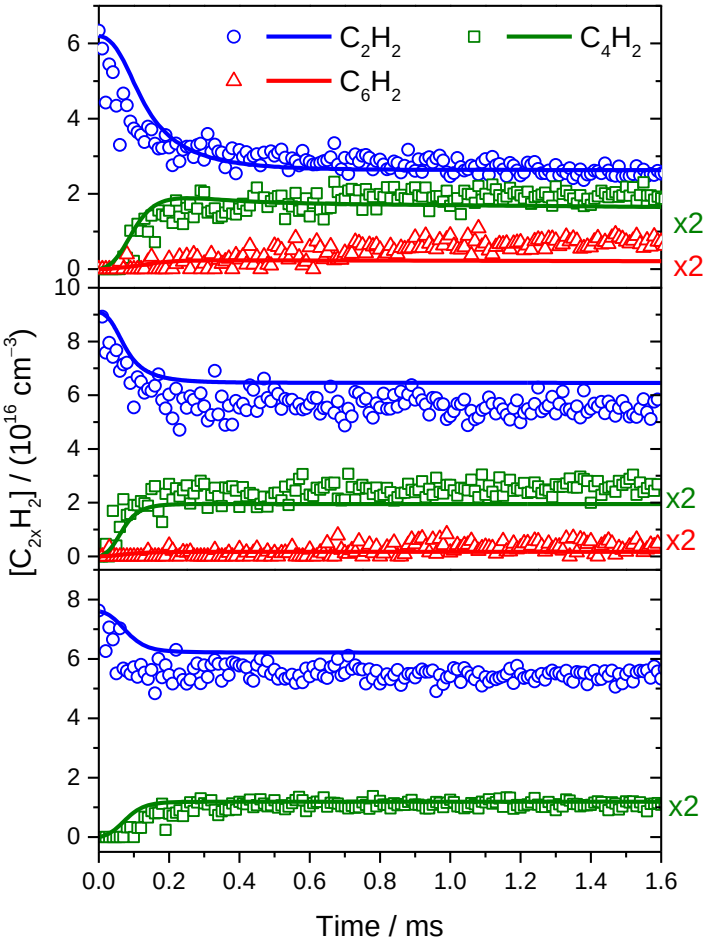

Figure 4.24: Comparison of the measured and calculated concentration-time profiles of $C_{2n}H_2$ species for a mixture of 2% C_2H_2, 1% Ar, and 97% Ne at T_5 = 2240 K and p_5 = 0.96 bar (a), a mixture of 2% C_2H_2, 2% H_2, 1% Ar, and 95% Ne at T_5 = 2245 K and p_5 = 1.41 bar (b) and a mixture of 2% C_2H_2, 4% H_2, 1% Ar, and 93% Ne at T_5 = 2250 K and p_5 = 1.18 bar (c). Solid lines are results of the simulations from this work [153] (see text).

Figure 4.25 shows that when increasing the temperature to 2315 K, a small amount of C_8H_2 is also detected for the mixture without H_2 added. In contrast, when adding 2% H_2 to the mixture no C_8H_2 is detected, whereas a small amount of C_6H_2 is still apparent. When further increasing the amount of H_2 to 4%, no traces of C_6H_2 and C_8H_2 are detected. C_2H_2 and C_4H_2

are well predicted by the model for all mixtures, but there is a slight underprediction for C_6H_2 and a small overprediction for C_8H_2.

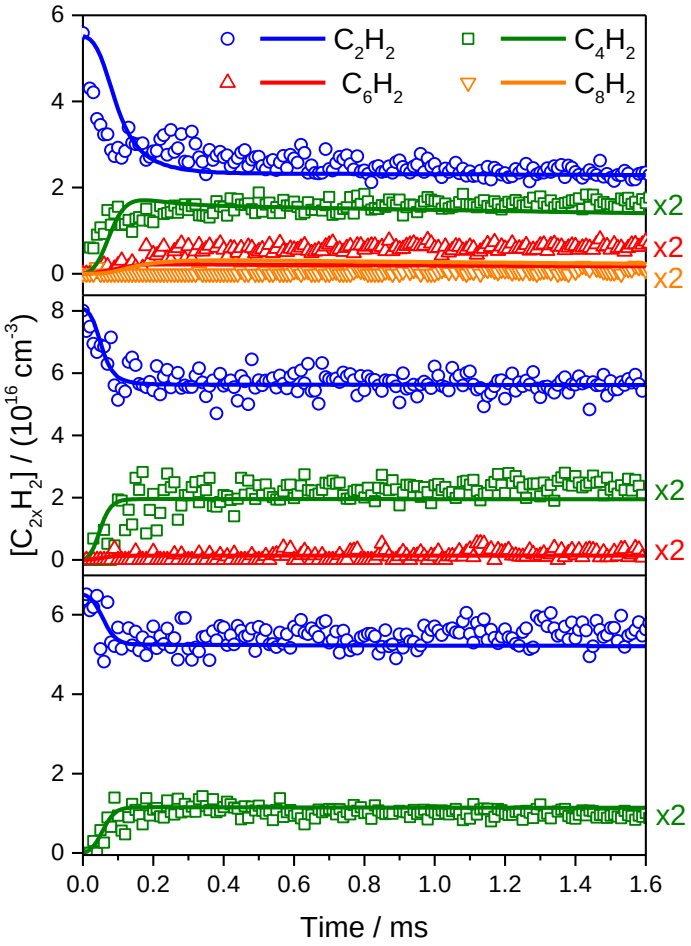

Figure 4.25: Comparison of the measured and calculated concentration-time profiles of $C_{2n}H_2$ species for a mixture of 2% C_2H_2, 1% Ar, and 97% Ne at T_5 = 2305 K and p_5 = 0.88 bar (a), a mixture of 2% C_2H_2, 2% H_2, 1% Ar, and 95% Ne at T_5 = 2315 K and p_5 = 1.29 bar (b) and a mixture of 2% C_2H_2, 4% H_2, 1% Ar, and 93% Ne at T_5 = 2315 K and p_5 = 1.04 bar (c). Solid lines are results of the simulations from this work [153] (see text).

Figure 4.26 shows three additional experiments with higher acetylene concentration (5%) and with variable H_2 concentration (0–4%) at the same reflected shock conditions ($T_5 \approx 2210$ K, $p_5 \approx 1.00$ bar). The model predicts the depletion of the C_2H_2 well for all 3 cases and there is a slight underprediction for C_4H_2 that becomes more prominent with increasing H_2 concentration. The model also underpredicts the C_6H_2 formation while there is a slight overprediction for C_8H_2 in the case without hydrogen addition and in the case with hydrogen addition, no C_8H_2 is detected.

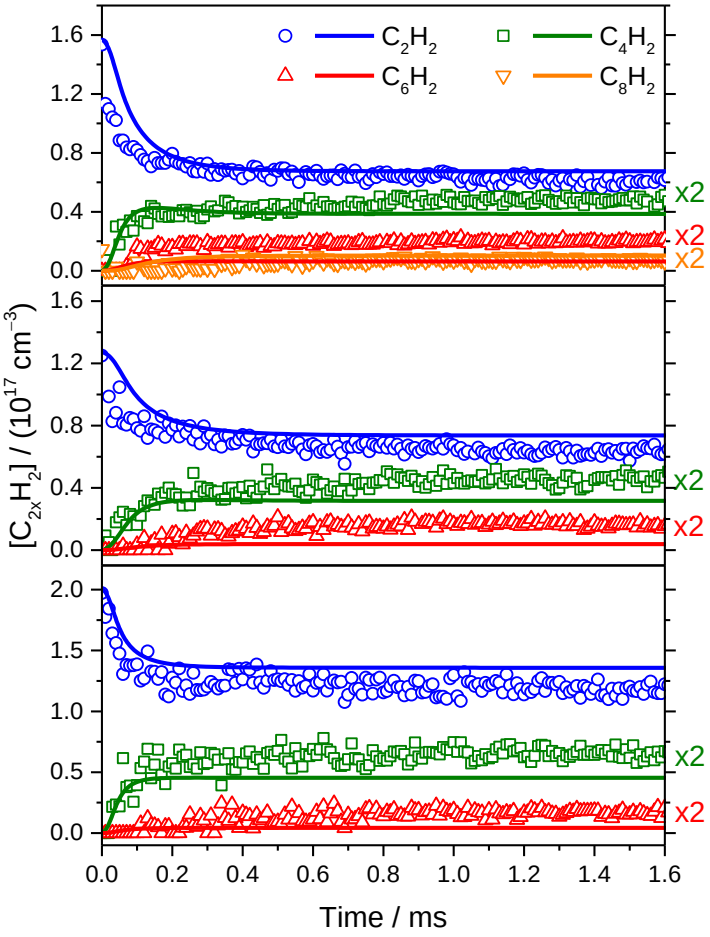

Figure 4.26: Comparison of the measured and calculated concentration-time profiles of $C_{2n}H_2$ species for a mixture of 5% C_2H_2, 1% Ar, and 97% Ne at T_5 = 2225 K and p_5 = 0.95 bar (a), a mixture of 5% C_2H_2, 2% H_2, 1% Ar, and 95% Ne at T_5 = 2195 K and p_5 = 0.76 bar (b) and a mixture of 5% C_2H_2, 4% H_2, 1% Ar, and 93% Ne at T_5 = 2215 K and p_5 = 1.21 bar (c). Solid lines are results of the simulations from this work [153] (see text).

Again all profiles are well reproduced by the model that shows that H_2 addition inhibits the formation of higher acetylenes. In exploring the reasons for the inhibition of polyacetylenes formation by H_2 addition, a reaction path analysis was carried out. This analysis shows that the following reactions ((R4.14) and (R4.17)) compete during the pyrolysis of acetylene at high temperatures:

$$C_2H_2 + M \rightleftharpoons C_2H + H + M \qquad \text{(R4.14)}$$

$$C_2H_2 + C_2H_2 \rightleftharpoons C_4H_3 + H \qquad \text{(R4.17)}$$

C_4H_2 is produced by addition of the ethynyl radical (C_2H) to C_2H_2 (R4.15). Additionally, further hydrogen-elimination reaction of C_4H_3 produces C_4H_2 (R4.18).

$$C_2H_2 + C_2H \rightleftharpoons C_4H_2 + H \quad \text{(R4.15)}$$

$$C_4H_3 \rightleftharpoons C_4H_2 + H \quad \text{(R4.18)}$$

Further C_2H addition to C_4H_2 and its reaction products via reaction type (R4.15) forms the next higher polyacetylenes C_6H_2, C_8H_2, etc. In experiments, C_4H_3 can be distinguished from C_4H_2 but is observable in experiments with initial concentrations of 5% C_2H_2 only. In this case, the intensity is about a factor of 10 smaller than that of the major product C_4H_2 but higher than the peak intensity on the same mass produced by the isotopic signature of ^{13}C with an abundance of 4.5% for C_4H_2. Therefore, the identified mass at 51 clearly reflects the C_4H_3 species.

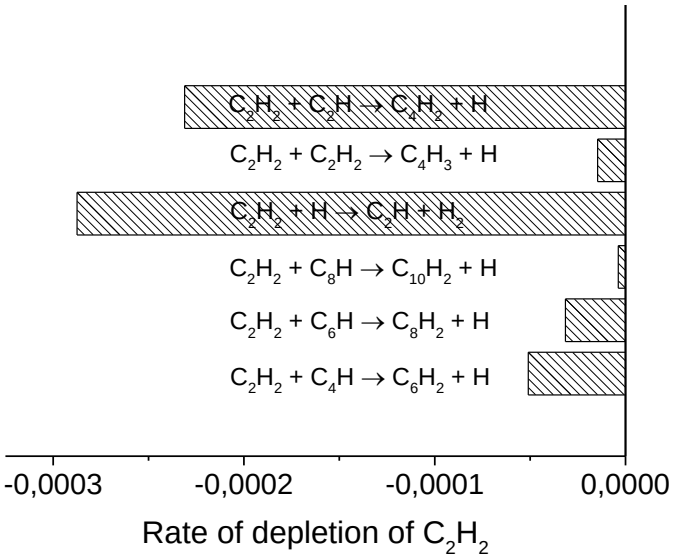

Figure 4.27: Rate of depletion of acetylene at 2225 K and 0.95 bar and a mixture of 5% C_2H_2, 1% Ar, and 97% Ne.

A reaction-path analysis was performed to determine the fate of acetylene and the reaction channels that are important for the formation of higher polyacetylenes. The results are exemplarily shown in Figure 4.27 for a reaction time of 0.1 ms and for a mixture of 5% C_2H_2 and 1% Ar in Ne at 2225 K and 0.95 bar. It can be clearly seen that acetylene is mainly consumed by reactions (R4.15) and (R4.19).

$$C_2H_2 + H \rightleftharpoons C_2H + H_2 \quad \text{(R4.19)}$$

Further formation of polyacetylenes ((R4.20) –(R4.22)) exhibits increasingly lower importance regarding C_2H_2 consumption:

$$C_2H_2 + C_4H \rightleftharpoons C_6H_2 + H \quad \text{(R4.20)}$$

$$C_2H_2 + C_6H \rightleftharpoons C_8H_2 + H \quad \text{(R4.21)}$$

$$C_2H_2 + C_8H \rightleftharpoons C_{10}H_2 + H \quad \text{(R4.22)}$$

In addition, simulations were performed using recent models of Chernov et al. (DLR) [164] and Ranzi [165] to analyze their performance towards the prediction of polyacetylenes. The results are shown in Figure 4.28 for an experiment with 5% C_2H_2 and 1% Ar in Ne at T_5 = 2225 K, p_5 = 0.95 bar. The model of Chernov et al. predicts a slower C_2H_2 consumption compared to our model and produces more C_4H_2 and less C_6H_2. Also, the plateau seen in the experimental data was not well reproduced. It should be noted that this model was developed for the gas-phase growth of PAH in methane, ethylene, and ethane flames but contains a submechanism for acetylene.

The model of Ranzi reaches the equilibrium plateau faster, but the predicted concentrations deviate from the measured ones for C_2H_2 and C_4H_2. The most important reactions of the three models for acetylene consumption to analyze the difference in their predictions were identified. In the Chernov mechanism, the depletion of C_2H_2 is mainly controlled by the following reactions:

$$C_2H_2 + M \rightleftharpoons C_2H + H + M \quad \text{(R4.14)}$$

$$C_2H_2 + H \rightleftharpoons C_2H + H_2 \quad \text{(R4.19)}$$

$$C_2H_2 + C_2H_2 \rightleftharpoons C_4H_2 + H_2 \quad \text{(R4.23)}$$

But these reactions cannot explain the discrepancies of the three models. It is rather the availability of the H-atom pool in each model that promotes further chain reactions.

The main H-atom sources identified in our model are:

$$C_2H_2 + C_2H_2 \rightleftharpoons C_4H_3 + H \qquad \text{(R4.17)}$$

$$C_4H_3 \rightleftharpoons C_4H_2 + H \qquad \text{(R4.18)}$$

with rate coefficients of $2.00\times10^{13}\exp(-186.3\ \text{kJ}/RT)\ \text{cm}^3\text{mol}^{-1}\text{s}^{-1}$ and $1.70\times10^{18}(T/\text{K})^{-1.23}\exp(-178.1\ \text{kJ}/RT)\ \text{cm}^3\text{mol}^{-1}\text{s}^{-1}$, respectively [92, 166]. The Chernov model contains only the much slower reaction $2C_2H_2 \rightarrow H_2CCCCH + H$ with a rate coefficient of $2.00\times10^{9}\exp(-121.9\ \text{kJ}/RT)\ \text{cm}^3\text{mol}^{-1}\text{s}^{-1}$.

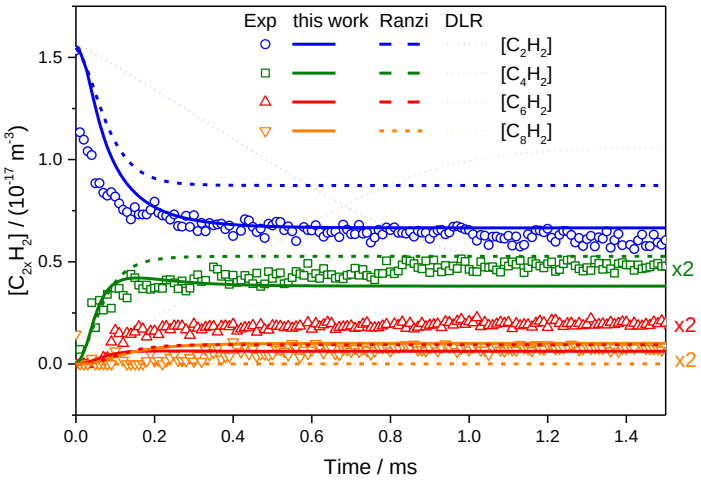

Figure 4.28: Simulations based on three models (this work [153], Chernov et al. [164], and Ranzi [165]) for an experiment with 5% C_2H_2 and 1%Ar in Ne (T_5 = 2225 K, p_5 = 0.95 bar).

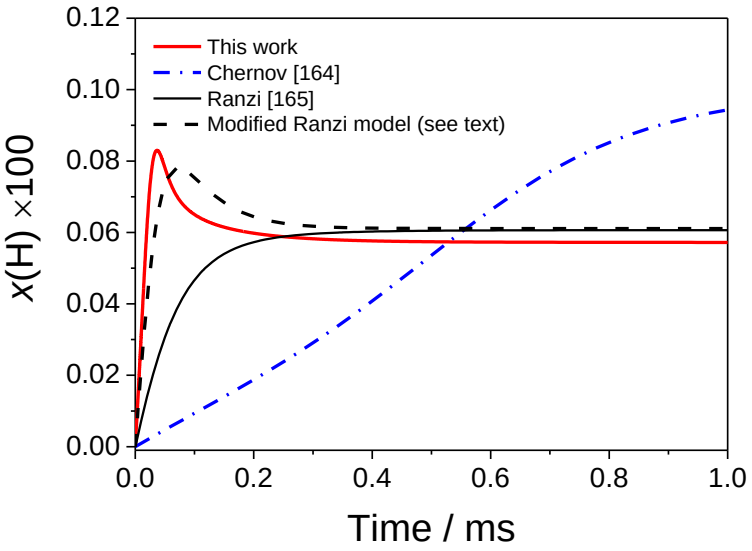

Figure 4.29: Simulated H-atom concentration for a mixture of 5% C_2H_2 balanced in neon. T_5 = 2225 K and p_5 = 0.95 bar.

Figure 4.29 shows the H-atom concentrations predicted by the three models. Our model produces within 50 µs sufficient H atoms to initiate further chain reactions, whereas in the model of Chernov the H-atom concentration increases much more slowly. In the Ranzi model, in contrast, the H-atom concentration is slightly lower than in our mechanism but the final values are close to each other. The H-atom initiation reaction (R4.14) in the Ranzi model has a rate coefficient of $k = 2.00\times10^{16}\ \exp(-341.2\ \text{kJ}/RT)\ \text{cm}^3\text{mol}^{-1}\text{s}^{-1}$ which is at 2225 K a factor of five lower than the value in our mechanism. When this rate coefficient is replaced with our value [153], both H-atom concentration profiles agree much better with each other (dashed line in Figure 4.29).

Interestingly, reactions (R4.19) $C_2H_2 + H \rightarrow C_2H + H_2$ and (R4.15) $C_2H_2 + C_2H \rightarrow C_4H_2 + H$ exhibit high rates of production and removal of H atoms, but their effect on the H-atom concentration does not influence the reaction progress because their contributions are antagonistic and cancel. Hence, only reactions (R4.17) and (R4.18) play a major role.

When incorporating both reactions ((R4.17) and (R4.18)) with the respective reaction coefficients in the Chernov model together with the rate coefficient for reaction (R4.19) $2.0\times10^{9}(T/\text{K})^{1.64}\ \exp(-126.8\ \text{kJ}/RT)\text{cm}^3\text{mol}^{-1}\text{s}^{-1}$ both models agree in the C_2H_2 decay although the (final) equilibrium concentrations still differ, apparently because of differences in thermodynamics data.

As discussed above, with added H_2, decreased C_2H_2 consumption and decreased concentrations of polyacetylenes were found. As deduced from the modeling, the addition of H_2 shifts the equilibrium of reaction (R4.19) to the left and therefore decreases the concentration of C_2H.

$$C_2H_2 + H \rightleftharpoons C_2H + H_2 \qquad \text{(R4.19)}$$

Therefore, less C_2H is available to form C_4H_2 via the $C_2H_2 + C_2H$ reaction (R4.15) in these mixtures. For the same reasons, the hydrogen atom concentration increases when H_2 is added. The increased concentration of H atoms shifts the equilibrium of reaction (R4.15) to the left for C_4H_2 and correspondingly also for higher polyacetylenes to the left, resulting in a decreased concentration of the latter compared to pyrolysis of C_2H_2 in the absence of H_2. The inhibiting effect of H_2 is confirmed in the experiment for acetylene and the polyacetylenes. These results are in agreement with the experiments of Eremin et al. of [151] where a decrease of particle volume fraction and particle sizes was observed.

The addition of H_2 causes also the formation of higher concentrations of aliphatic hydrocarbons by the reaction of C_2H_2 with H_2:

$$C_2H_2 + H_2 \rightleftharpoons C_2H_3 + H \quad \text{(R4.24)}$$

$$C_2H_2 + H_2 (+M) \rightleftharpoons C_2H_4 (+M) \quad \text{(R4.25)}$$

This trend is also observed in the experiments where the formation of hydrocarbons such as C_2H_4 is enhanced with hydrogen addition.

The concentrations of the aromatic compounds (C_6H_5, C_6H_6 and C_8H_6) are below the detection limits of our experiment. This is in agreement with the simulations where the mole fraction of benzene is below 10^{-8}, the mole fractions of larger aromatic species are even smaller. Thus, regarding the influence of H_2 on the formation of polycyclic aromatic hydrocarbons (PAH) in C_2H_2 pyrolysis only modeling studies can be carried out. The simulations predict a decreasing concentration of these species by addition of H_2. This result is due to the important role of aromatic radicals ($PAH^{\bullet}$) for the build-up of large PAH structures. The concentration of these radicals is influenced by H_2 via reactions of the type:

$$PAH + H \rightleftharpoons PAH^{\bullet} + H_2 \quad \text{(R4.26)}$$

The availability of higher H_2 concentrations favors the reverse reaction (R4.26) and thus decreases the concentrations of the $PAH^{\bullet}$ radicals which consequently suppress PAH formation pathways by C_2H_2 addition through reactions of the type:

$$PAH^{\bullet} + C_2H_2 \rightleftharpoons PAHC_2H + H \quad \text{(R4.27)}$$

Compared to the pure pyrolysis case where H_2 and H atoms can also be formed from hydrocarbon-bonded hydrogen, the addition of molecular hydrogen leads to a faster availability of reactive species (H, radicals) which cause a depletion of building blocks of particle formation, such as polyacetylenes, aromatic species, and carbon clusters. The equilibrium (final) value of C_2H_2 seems to be reached faster when H_2 is added.

4.3.3. Conclusion

Thermal decomposition of C_2H_2 was studied behind reflected shock waves in the 1760–2565 K temperature range for pressures between 0.75 and 1.23 bar. Concentration-time profiles for C_2H_2 and polyacetylenes ($C_{2n}H_2$, n = 2–4) were measured by HRR-TOF-MS. Ben-

zene and higher polyacetylenes (n > 4) were not detected within the detection limits of the experiment. The experimental results were compared to simulations based on a model of this study and two models from literature [92, 147]. While the prediction was good for most detected species after longer test times with all three models, the developed model provided significantly improved simulations for the concentration-time profiles within the first 500 µs. The results were also compared with two additional models with large C_2H_2 submechanisms from the literature [164, 165]. Reaction rate analysis has shown that the reactions of H atoms have a significant impact on the kinetics of acetylene and polyacetylenes. The very good agreement of the experiments and the calculations show that these reactions are very well described in our mechanism.

The impact of H_2 on the formation of polyacetylenes was investigated. The presence of H_2 reduced the consumption of acetylene, and reduced the concentration of the respective polyacetylenes. This is attributed to an enhanced consumption of the crucial carbon-adding radicals C_2H, $PAH^{\bullet}$ especially required for the fast build-up of carbonaceous material of particle precursors by H_2, resulting in species of less reactivity. In fact the equilibrium shift (see reaction (R4.19)) according to H_2 addition results in decreased concentrations of C_2H.

5. Outlook

One important suggestion for the future work is to use HRR-TOF-MS with the gas chromatograph/mass spectrometer (GC/MS). HRR-TOF-MS enables the quasi-simultaneous time-resolved detection of multiple species. In addition, the use of GC/MS allows accurate, sensitive end-product analysis and the distinction between these end-products. For the use of a GC homogeneous conditions must prevail for several milliseconds followed by rapid quenching by rarefaction waves. In order to prevent reheating of the test gas, a dump-tank can be used to trap the reflected shock wave and to run the shock tube in single-pulse mode.

Combining time-resolved kinetics measurements of multiple species by HRR-TOF-MS with end-product analysis by GC combines the advantages of both techniques and is therefore a strong tool to study and understand the chemical kinetics of complex reaction systems at high temperature.

One challenging issue in TOF-MS studies is overlapping of the species with the same nominal masses (like CO and C_2H_4 with the same m/z = 28), which complicates the mass spectra analysis. The alternative solution to get rid of this problem is using laser absorption spectroscopy for some species. The measurement section of the tube has four quartz windows which enable using laser absorption spectroscopy measurements on the shock tube simultaneously with TOF-MS and GC-MS. For example, time-resolved CO measurements using a continuous-wave quantum cascade laser (cw-QCL) can be used to probe time-resolved CO absorption.

During the study of the decomposition of some precursor, the non-zero level at longer time in concentration-time profile of the precursor is observed which is not in an agreement with the simulation with complete conversion (zero level). This offset in the measurement stems off the stationary pressure in the mass spectrometer. The way to overcome this memory effect could be either using an expansion tank with much larger volume in the ionization section to eliminate the background pressure or by using the ultra-fast shutter in front of the nozzle that is opened just few microseconds before reflection of the shock wave. Another alternative to quantify the offset and subtract it from the post-shock signals.

6. Conclusions

Soot formation has always been an interesting issue for combustion researchers. On one hand soot is one of the most important combustion-generated pollutants, on the other hand soot (e.g. carbon black) is an important industrial product which is widely used in different industrial applications. Therefore modelling of soot formation pathways from different hydrocarbon fuels is of great importance both for decreasing the soot emission from combustion devices and for producing tailored carbonaceous material for industrial applications.

Soot formation in hydrocarbon combustion is to a large extent determined by reactions that include hydrogen. Models that describe the formation of soot therefore critically depend on a detailed understanding of the role of hydrogen. Also, the properties of soot are strongly influenced by the presence of hydrogen, most obviously seen by comparing “conventional” soot with soot formed in hydrogen-free systems. The influence of hydrogen and the variation of fuels on soot yield have been studied in several experiments. In several experimental and theoretical studies [23, 35-37], hydrogen was added to fuels to study the influence of hydrogen on the overall combustion or pyrolysis process; but the main aim was towards the influence of hydrogen on the soot yield. Glassman [38] studied the fuel sooting tendency in shock tubes and different types of flames with various chemical systems. From these studies, however, no details about the underlying mechanism of the impact of hydrogen on soot formation could be derived. Numerous studies have investigated the effect of hydrogen on soot formation with two different strategies:

- Addition a defined amount of H_2 to hydrocarbon fuel (C_mH_n) to study its effect on soot formation
- Hydrocarbon fuels with varying C/H ratios

Quantitative knowledge about the influence of hydrogen, however, is missing despite its crucial impact on soot formation pathways. Therefore, the purpose of this work was to investigate the complex role of hydrogen in the formation of soot particles from gas-phase reactions while systematically varying C/H ratios and temperature under non-oxidizing conditions in shock tubes using high-repetition-rate time-of-flight mass spectrometry (HRR-TOF-MS). For this purpose, the effect of bonded hydrogen and also addition of molecular hydrogen was investigated. Two different hydrogen-free precursors exhibiting different initial decomposition steps, chlorinated and oxygenated, were selected. As a hydrogen-free chlorinated hydrocarbon, the pyrolysis of CCl_4 and as a hydrogen-free oxygenated precursor the

pyrolysis of C_3O_2 was studied behind reflected shock waves using HRR-TOF-MS. Additionally, the pyrolysis of simple hydrocarbon fuel containing bonding hydrogen (C_2H_2) and also the effect of molecular hydrogen (H_2) addition in soot formation were investigated.

In CCl_4 pyrolysis, C_2Cl_2 and Cl_2 were detected as products of CCl_4 thermal decomposition and concentration-time profile of CCl_3 + CCl_4, C_2Cl_2, and Cl_2 derived using shock tube and HRR-TOF-MS. The experiments showed that the CCl_4 decomposition proceeds through the following reaction sequence:

$$CCl_4 \rightarrow CCl_3 \rightarrow CCl_2 \rightarrow CCl$$

Therefore, secondary reactions between decomposition products are important. A sensitivity analysis of the reactions involved in CCl_4 pyrolysis showed that the first Cl abstraction was only influential during the first 10 µs and the bimolecular reaction of $CCl_2 + CCl_2 \rightleftharpoons C_2Cl_2 + 2Cl$ played a highly important role. Additionally, the measurements revealed that the reaction sequence to carbonaceous material in CCl_4 pyrolysis proceeds via:

$$CCl_4 \rightarrow CCl_2 \rightarrow C_2Cl_2 \rightarrow \text{chlorinated polyynes} \rightarrow C_n$$

Whereas the further addition of C_2Cl_2 to C_n was found to be the key step in cluster formation at the reaction conditions investigated in this study.

In C_3O_2 pyrolysis, concentration-time profiles for C_3O_2 and CO were measured simultaneously by HRR-TOF-MS. The data served for validation for an improved kinetics model for C_3O_2 decomposition that incorporates the growth of carbon particles up to approximately 1 nm in diameter. The measurements were in reasonable agreement with the model predictions for temperatures up to 1800 K. Furthermore, the integrated concentration profiles of C atoms and C_2 molecules were detected and related to model predictions for these species and large clusters' concentrations. The experimental C/C_2 concentration ratio was compared with the simulation. The increasing trend in C/C_2 profile versus T_5 was observed which was according to relative decrease of C_2 concentration in comparison to concentration of C atoms. The resulting observations indicate that the C_2-addition channel is more important for carbon cluster growth compared to reactions with C-atom addition to the corresponding clusters.

Thermal decomposition of C_2H_2 was studied behind reflected shock waves in the 1760–2565 K temperature range for pressures between 0.75 and 1.23 bar. Concentration-time profiles for C_2H_2 and polyacetylenes ($C_{2n}H_2$, n = 2–4) were measured by HRR-TOF-MS. Benzene and higher polyacetylenes (n > 4) were not detected within the sensitivity of the experiment. Only in experiments with higher concentration of acetylene (5% C_2H_2), small traces of

C_4H_3 – which is an important radical to form the first aromatic ring – were detected. The signal intensities of polyacetylenes decreased with larger molecular weights ($C_4H_2 > C_6H_2 > C_8H_2$) and reached a plateau at longer time. The experimental results were compared to simulations based on a new model and two existing models from literature [92, 147]. While the prediction was good for most detected species after longer test times with all three models, the new model provided significantly improved simulations for the concentration-time profiles within the first 500 µs. A reaction-rate analysis showed that the reactions of H atoms have a significant impact on the kinetics of acetylene and polyacetylenes. The sensitivity analysis of the acetylene loss showed that acetylene is mainly consumed via two competing reactions:

$C_2H_2 + C_2H \rightleftharpoons C_4H_2 + H$

$C_2H_2 + H \rightleftharpoons C_2H + H_2$

Further formation of polyacetylenes showed less importance in C_2H_2 consumption.

The impact of H_2 on the formation of polyacetylenes was investigated. The presence of H_2 reduced the consumption of acetylene, and reduced the concentration of respective polyacetylenes. In fact H_2 acts as soot inhibitor by enhancing consumption of crucial carbon-adding radicals like C_2H, especially required for the fast build-up of carbonaceous material.

The present research work provides data and improved understanding of the gas-phase kinetic of various carbon-containing soot precursors and shows the effect of chemically bonded and molecular hydrogen on soot formation in the earlier stage of the initial cluster formation towards the formation of soot particles.

7. Own publications

Peer-reviewed publications:

- S.H. Dürrstein, M. Aghsaee, L. Jerig, M. Fikri, C. Schulz, A shock tube with a high-repetition-rate time-of-flight mass spectrometer for investigations of complex reaction systems, *Rev. Sci. Instrum.* **82** (2011) 084103 (1–7)
- M. Aghsaee, H. Böhm, S. Dürrstein, M. Fikri, C. Schulz, Experimental and modelling study of carbon suboxide decomposition behind reflected shock waves, *Phys. Chem. Chem. Phys.* **14** (2012) 1246–1252
- M. Aghsaee, A. Drakon, A. Eremin, S. Dürrstein, H. Böhm, H. Somnitz, M. Fikri, C. Schulz, Experimental investigation of kinetics of CCl_4 pyrolysis behind reflected shock waves using high-repetition-rate time-of-flight mass spectrometry, *Phys. Chem. Chem. Phys.* **15** (2013) 2821–2828
- M. Aghsaee, S. Dürrstein, J. Herzler, H. Böhm, M. Fikri, C. Schulz, Influence of molecular hydrogen on acetylene pyrolysis: Experiment and modeling, *Combust. Flame* **161** (2014) 2263–2269
- M. Aghsaee, D. Nativel, M. Bozkurt, M. Fikri, N. Chaumeix, C. Schulz, Experimental study of the kinetics of ethanol pyrolysis and oxidation behind reflected shock waves and in laminar flames, *Proc. Combust. Inst.* **35** (2014) 393–400
- S. Zabeti, M. Aghsaee, M. Fikri, O. Welz, C. Schulz, Optical properties and pyrolysis of shock-heated gas-phase anisole, *Proc. Combust. Inst.* **36**, in review (2017).

Conference contributions:

- M. Aghsaee, A. Drakon, S. H. Dürrstein, M. Fikri, C. Schulz, A shock-tube TOF-MS apparatus with modular sampling unit for investigations of complex kinetic reaction systems, 21st International Symposium on Gas Kinetics, 18th – 22nd July, 2010, Leuven, Belgium, Poster
- M. Aghsaee, S. H. Dürrstein, H. Böhm, C. Schulz, Pyrolysis of carbon suboxide (C_3O_2) behind reflected shock waves using a high-repetition-rate time-of-flight mass

spectrometer coupled to a shock tube, 5th European Combustion Meeting, 28th June – 1st July, 2011, Cardiff, Wales, Poster

- S.H. Dürrstein, M. Aghsaee, B. Lam, D.F. Davidson, C. Schulz, R.K. Hanson, A shock-tube with high-repetition-rate time-of-flight mass spectrometry study of 3-pentanone pyrolysis behind reflected shock waves, 7th International Conference on Chemical Kinetics, 10th – 14th July, 2011, MIT, Cambridge, MA, USA
- M. Aghsaee, A. Abdali, S.H. Dürrstein, C. Schulz, A shock-tube with high-repetition-rate time-of-flight mass spectrometry for the study of complex reaction systems, 28th International Symposium on Shock Waves, 17th – 22nd July, 2011, Manchester, England, Talk
- M. Aghsaee, B. Shu, M. Fikri, C. Schulz, A high-repetition-rate time-of-flight mass-spectrometry study of 3-pentanone pyrolysis and oxidation behind reflected shock waves, 6th European Combustion Meeting, 25th – 28th June, 2013, Lund, Sweden, Poster
- B. Shu, M. Aghsaee, M. Fikri, C. Schulz, Shock tube investigation of the decomposition of cyclohexene at high temperature, 6th European Combustion Meeting, 25th – 28th June, 2013, Lund, Sweden, Poster
- M. Aghsaee, D. Nativel, M. Bozkurt, M. Fikri, N. Chaumeix, C. Schulz, Experimental study of the kinetics of ethanol pyrolysis and oxidation behind reflected shock waves and in laminar flames, 35th International Symposium on Combustion, 3rd – 8th August, 2014, San Francisco, California, USA, Talk
- S. Zabeti, M. Aghsaee, M. Fikri, O. Welz, C. Schulz, A high-temperature shock-tube study on the optical properties and pyrolysis of anisole, 7th European Combustion Meeting, 30th March – 2nd April, 2015, Budapest, Hungary, Poster
- M. Aghsaee, B. Shu, O. Welz, M. Fikri, C. Schulz, Experimental study of 3-pentanone pyrolysis and oxidation, 9th International Conference on Chemical Kinetics, 28th June – 2nd July, 2015, Ghent, Belgium, Talk
- P. Sela, M. Aghsaee, J. Birkmann, B. Shu, J. Herzler, M. Fikri, C. Schulz, O. Welz, A single-pulse, shock tube coupled with high-repetition-rate time-of-flight mass spectrometry and gas chromatography for high-temperature kinetics studies, 9th International Conference on Chemical Kinetics, 28th June – 2nd July, 2015, Ghent, Belgium, Poster

8. Appendix

8.1. Excerpt of reaction mechanism of CCl_4 decomposition

Reaction	Rate constants			Reference
	A / cm^3, mol, s	n	E_a / kJ/mol	
CCl_4 and CCl_3 reactions				
$CCl_4 = CCl_3 + Cl$	2.60×10^{16}	0	286	[119]
$CCl_4 + Cl = CCl_3 + 2Cl$	5.75×10^{13}	0	65.7	[118]
$CCl_4 + C_1 = CCl_3 + CCl$	9.04×10^{12}	0	0	[118]
$CCl_2 + Cl = CCl_3$	1.58×10^{13}	0	0	[120]
$CCl_3 + Cl = CCl_2 + Cl_2$	1.00×10^{14}	0	0	[106]
CCl_2 and CCl reactions (C1 & C_2 formation)				
$CCl_2 + M = CCl + Cl + M$	4.4×10^{15}	0	283.1	[117]
$CCl + Cl = C_1 + Cl_2$	8.49×10^{13}	0	103.2	[121]
$CCl + CCl = C_2 + Cl + Cl$	2.2×10^{13}	0	0	[117]
$2CCl + M = C_2Cl_2 + M$	5.4×10^{14}	0	63.6	[117]
$CCl + M = C_1 + Cl + M$	4.32×10^{15}	0	291.4	[118]
C_2Cl_m reactions				
$CCl_3 + CCl_3 = C_2Cl_6$	4.55×10^{12}	–1.6	1.5	[118]
$C_2Cl_6 + CCl_3 = CCl_4 + C_2Cl_5$	7.94×10^{11}	0	59.9	[118]
$C_2Cl_5 + Cl_2 = C_2Cl_6 + Cl$	2.04×10^{11}	0	9.9	[122]
$C_2Cl_5 = C_2Cl_4 + Cl$	1.12×10^{16}	0	62.4	[118]
$C_2Cl_5 + Cl = C_2Cl_4 + Cl_2$	2.45×10^{13}	0	0	[123]
$C_2Cl_3 + Cl = C_2Cl_4$	2.45×10^{13}	0	0	[117]
$CCl_2 + CCl_2 + M = C_2Cl_4 + M$	5.7×10^{15}	0	24.9	[117]
$C_2Cl_2 + Cl + M = C_2Cl_3 + M$	3.55×10^{7}	0.9	46.5	[117]
$C_2Cl_3 + C_2Cl = 2\ C_2Cl_2$	1.00×10^{13}	0	0	[106]
$C_2Cl_3 + Cl = C_2Cl_2 + Cl_2$	1.00×10^{13}	0	0	[106]
C_2Cl_2 and C_2Cl reactions (C_2 formation)				
$CCl_2 + CCl_2 = C_2Cl_2 + 2Cl$	5.4×10^{14}	0	63.6	[117]
$C_2Cl_2 + Cl = C_2Cl + Cl_2$	2.00×10^{14}	0	219	[106]
$C_2Cl_2 = C_2Cl + Cl$	5.00×10^{15}	0	452	[106]
$C_2Cl_2 + M = C_2 + 2Cl + M$	9.29×10^{15}	0	283.9	[117]

$C_2Cl_2 + M = C_2 + 2Cl + M$	9.29×10^{15}	0		824.8	[116]
C_nCl_2 (polyynes) formation					
$C_2Cl_2 + C_2Cl = C_4Cl_2 + Cl$	4.47×10^{13}	0		0	[106]
$C_2Cl_2 + C_2Cl_2 = C_4Cl_2 + Cl_2$	1.00×10^{14}	0		0	[106]
$C_4Cl_2 + C_2Cl = C_6Cl_2 + Cl$	2.00×10^{13}	0		0	[106]
$C_4Cl_2 + C_2Cl_2 = C_6Cl_2 + Cl_2$	1.00×10^{14}	0		0	estimated on [106]
$C_6Cl_2 + C_2Cl = C_8Cl_2 + Cl$	2.00×10^{13}	0		0	[106]
$C_6Cl_2 + C_2Cl_2 = C_8Cl_2 + Cl_2$	1.00×10^{14}	0		0	estimated on [106]
$Cl_2 \leftrightarrow Cl$ reactions					
$Cl_2 + M \rightarrow 2Cl + M$	2.32×10^{13}	0		196.5	[127]
$2Cl + M \rightarrow Cl_2 + M$	2.23×10^{14}	0		–7.54	[127]
Carbon cluster growth					
$C_n + C_1 \rightarrow C_{n+1}$	4.5×10^{11}	0.5		0	[108]
$C_n + C_2 \rightarrow C_{n+2}$	4.5×10^{11}	0.5		0	[126]
$C_n + C_2Cl_2 \rightarrow C_{n+2} + Cl_2$	8.32×10^{9}	0.5		0	[106]
$C_n + C_2Cl \rightarrow C_{n+2} + Cl$	8.71×10^{9}	0.5		0	[106]
$C_n + C_m \rightarrow C_{n+m}$	4.5×10^{12}	0.5	0		[125]

8.2. Reaction mechanism of C_2H_2 decomposition

```
!*****************************************************************************
!k= A Tn exp (-Ea/RT)        A: cm3 mole-1 s-1          Ea: cal
!A          n               Ea
!Units: cm3, s^-1, mol, cal
!*****************************************************************************
ELEMENTS
C     H     KR    AR    NE
END
SPECIES
C1    C2    C3    C4    C6    C8    C10   C12
H     H2
CH    CH2   CH2S  CH3   CH4
C2H   C2H2  C2H3  C2H4  C2H5  C2H6
C3H   C3H2  C3H3  AC3H4 PC3H4 C3H5  C3H6
C4H   C4H2  C4H3S C4H3U C4H4  C4H5S C4H5U C4H6
```

```
C6H2   C6H    C8H2   C8H    C10H2 C10H   C12H2 C12H
AR      NE
END
REACTIONS
!****************************************************************************
!**************************C1system*****************************************
!****************************************************************************
C1 + CH3 = C2H2 + H                 5.00E+13      0.0      0.0
C1 + CH2 = C2H + H                  5.00E+13      0.0      0.0
!****************************************************************************
!**************************C2system*****************************************
!****************************************************************************
C1 + C1 = C2                        4.50E+11      0.5      0.0
C2 + H2 = C2H + H                   6.600E+13     0.0      7950.0
!****************************************************************************
!**************************Polyine******************************************
!****************************************************************************
C4H2 + C2H = C6H2 + H               3.000E+13     0.0      0.00
C2H2 + C4H = C6H2 + H               3.000E+13     0.0      0.00
C4H2 + C2 = C6H + H                 3.000E+13     0.0      0.0
C2H2 + C4 = C6H + H                 3.000E+13     0.0      0.0
C6H + C2 = C6 + C2H                 6.000E+13     0.0      0.0
C6H + C6H = C6 + C6H2               1.800E+12     0.0      0.0
C6H + C4H = C6 + C4H2               1.800E+12     0.0      0.0
C6H + C4H = C4 + C6H2               1.800E+12     0.0      0.0
C6H + H2 = C6H2 + H                 4.090E+05     2.39     200.00
C6H2 + C2H = C8H2 + H               3.000E+13     0.0      0.00
C2H2 + C6H = C8H2 + H               3.000E+13     0.0      0.00
C4H2 + C4H = C8H2 + H               3.000E+13     0.0      0.00
C6H2 + C2 = C8H + H                 3.000E+13     0.0      0.0
C2H2 + C6 = C8H + H                 3.000E+13     0.0      0.0
C4H2 + C4 = C8H + H                 3.000E+13     0.0      0.0
C8H + C2 = C8 + C2H                 6.000E+13     0.0      0.0
C8H + C8H = C8 + C8H2               1.800E+12     0.0      0.0
C8H + C6H = C8 + C6H2               1.800E+12     0.0      0.0
C8H + C6H = C6 + C8H2               1.800E+12     0.0      0.0
C8H + C4H = C8 + C4H2               1.800E+12     0.0      0.0
```

C8H + C4H = C4 + C8H2	1.800E+12	0.0	0.0
C8H + H2 = C8H2 + H	4.090E+05	2.39	200.0
C8H2 + C2H = C10H2 + H	3.000E+13	0.0	0.0
C2H2 + C8H = C10H2 + H	3.000E+13	0.0	0.0
C6H2 + C4H = C10H2 + H	3.000E+13	0.0	0.0
C4H2 + C6H = C10H2 + H	3.000E+13	0.0	0.0
C8H2 + C2 = C10H + H	3.000E+13	0.0	0.0
C2H2 + C8 = C10H + H	3.000E+13	0.0	0.0
C6H2 + C4 = C10H + H	3.000E+13	0.0	0.0
C4H2 + C6 = C10H + H	3.000E+13	0.0	0.0
C10H + C2 = C10 + C2H	6.000E+13	0.0	0.0
C10H + C10H = C10 + C10H2	1.800E+12	0.0	0.0
C10H + C8H = C10 + C8H2	1.800E+12	0.0	0.0
C10H + C8H = C8 + C10H2	1.800E+12	0.0	0.0
C10H + C6H = C10 + C6H2	1.800E+12	0.0	0.0
C10H + C6H = C6 + C10H2	1.800E+12	0.0	0.0
C10H + C4H = C10 + C4H2	1.800E+12	0.0	0.0
C10H + C4H = C4 + C10H2	1.800E+12	0.0	0.0
C10H + H2 = C10H2 + H	4.090E+05	2.39	200.0
C10H2 + C2H = C12H2 + H	3.000E+13	0.0	0.0
C2H2 + C10H = C12H2 + H	3.000E+13	0.0	0.0
C8H2 + C4H = C12H2 + H	3.000E+13	0.0	0.0
C4H2 + C8H = C12H2 + H	3.000E+13	0.0	0.0
C6H2 + C6H = C12H2 + H	3.000E+13	0.0	0.0
C12H + H2 = C12H2 + H	4.090E+05	2.39	200.0
C10H2 + C2 = C12H + H	3.000E+13	0.0	0.0
C2H2 + C10 = C12H + H	3.000E+13	0.0	0.0
C8H2 + C4 = C12H + H	3.000E+13	0.0	0.0
C4H2 + C8 = C12H + H	3.000E+13	0.0	0.0
C6H2 + C6 = C12H + H	3.000E+13	0.0	0.0
C12H + C2 = C12 + C2H	6.000E+13	0.0	0.0
C12H + C12H = C12 + C12H2	1.800E+12	0.0	0.0
C12H + C10H = C12 + C10H2	1.800E+12	0.0	0.0
C12H + C10H = C10 + C12H2	1.800E+12	0.0	0.0
C12H + C8H = C12 + C8H2	1.800E+12	0.0	0.0
C12H + C8H = C8 + C12H2	1.800E+12	0.0	0.0
C12H + C6H = C12 + C6H2	1.800E+12	0.0	0.0

```
C12H + C6H = C6 + C12H2              1.800E+12    0.0     0.0
C12H + C4H = C12 + C4H2              1.800E+12    0.0     0.0
C12H + C2H = C2 + C12H2              1.800E+12    0.0     0.0
C12H + C2H = C12 + C2H2              1.800E+12    0.0     0.0
!*************************************************************************
!************************H2system*****************************************
!*************************************************************************
H+H+M=H2+M                           0.18E+19     -1.00   0.0
H2/1.0/ AR/0.35/ NE/0.35/ C2H2/3.0/
!*************************************************************************
!************************CH/CH2system*************************************
!*************************************************************************
CH2+H=CH+H2                          0.60E+13     0.00    -1791.3
CH2+CH2=C2H2+H2                      0.12E+14     0.00    812.1
CH2+CH2=C2H2+H+H                     0.11E+15      0.00   812.1
CH2+CH3=C2H4+H                       0.42E+14     0.00    0.0
CH2S+M=CH2+M                         0.12E+14     0.00    0.0
H2/1.0/ AR/0.35/ NE/0.35/ C2H2/3.0/
CH3+H=CH2S+H2                        6.00E+00     0.00    15097.9
!*************************************************************************
!************************CH3/CH4system************************************
!*************************************************************************
CH3+M=CH2+H+M                        0.10E+17     0.00    90522.6
H2/1.0/ AR/0.35/ NE/0.35/ C2H2/3.0/
CH3+M=CH+H2+M                        0.69E+15     0.00    82423.3
H2/1.0/ AR/0.35/ NE/0.35/ C2H2/3.0/
CH2S+CH3=C2H4+H                      0.16E+14     0.00    -568.5
CH4(+M)=CH3+H(+M)                    2.40E+16     0.00    10487.3
        LOW/ 1.29E+18        0.00    90771.6/
        TROE/ 0.0 1350.0 1.00 7830.0/
H2/1.0/ AR/0.35/ NE/0.35/ C2H2/3.0/
CH3+CH3(+M)=C2H6(+M)                 3.61E+13     0.00    0.0
        LOW/ 3.63E+41        -7.00   2771.1/
        TROE/ 0.62 73.0 1180.0 0.0/
H2/1.0/ AR/0.35/ NE/0.35/ C2H2/3.0/
CH4+H=H2+CH3                         0.13E+05     3.00    8980.6
CH4+CH=C2H4+H                        0.30E+14     0.00    -406.0
```

```
CH4+CH2=CH3+CH3                 4.30E+12    0.00    10033.4
!*****************************************************************************
!********************C2H2system*************************************************
!*****************************************************************************
C2H+CH4=C2H2+CH3                2.17E+10    0.94    652.2
C2H2+M=C2H+H+M                  0.36E+17    0.00    106525.3
H2/1.0/ AR/0.35/ NE/0.35/ C2H2/3.0/
C2H2+H=C2H+H2                   2.01E+09    1.64    30289.1
C2H3(+M)=C2H2+H(+M)             7.80E+08    1.62    37042.5
        LOW/3.24E+27        -3.4    35790.7/
        TROE/ 0.35 000.0 0.0 0.0/
H2/1.0/ AR/0.35/ NE/0.35/ C2H2/3.0/
C2H3+H=C2H2+H2                  4.22E+13    0.00    0.0
C2H4+M=C2H2+H2+M                2.92E+17    1.00    78234.6
H2/1.0/ AR/0.35/ NE/0.35/ C2H2/3.0/
C2H4+M=C2H3+H+M                 7.40E+17    0.00    96526.5
H2/1.0/ AR/0.35/ NE/0.35/ C2H2/3.0/
C2H4+H=C2H3+H2                  2.35E+15    3.62    11261.3
C2H4+CH3=C2H3+CH4               6.02E+07    1.56    16626.9
C2H4+H(+M)=>C2H5(+M)            3.98E+09    1.28    1290.0
        LOW/ 1.18E+19       0.0     764.45/
        TROE/ 0.76 40.0 1025.0 0.0/
H2/1.0/ AR/0.35/ NE/0.35/ C2H2/3.0/
C2H5(+M)=>C2H4+H(+M)            4.10E+13    0.00    39847.1
        LOW/3.65E+18        0.0     33368.37/
        TROE/ 0.75 97.0 1379.0 0.0/
H2/1.0/ AR/0.35/ NE/0.35/ C2H2/3.0/
C2H5+H=CH3+CH3                  4.22E+13    0.00    0.0
C2H5+CH3=C2H4+CH4               9.03E+11    0.00    0.0
C2H5+C2H5=C2H4+C2H6             0.14E+13    0.00    0.0
C2H6+H=C2H5+H2                  9.82E+13    0.00    9216.4
C2H6+CH=C2H4+CH3                1.08E+14    0.00    262.8
!*****************************************************************************
!******************C3H6system*************************************************
!*****************************************************************************
C3H6 = C3H5 + H                 2.500E+15   0.0     86688.0
C3H6 = C2H3 + CH3               6.310E+15   0.0     85800.0
```

```
!************************************************************************
!*******************C3H5system*****************************************
!************************************************************************
C3H5 + H = AC3H4 + H2              3.333E+12    0.0     0.0
C3H5 + H2 = C3H6 + H               084E+05      2.4     18976.0
C3H5 + CH4 = C3H6 + CH3            3.975E+01    3.4     23188.0
!************************************************************************
!*******************C3H4system*****************************************
!************************************************************************
AC3H4 + M = C3H3 + H + M           2.000E+18    0.0     80000.0
H2/1.0/ AR/0.35/ NE/0.35/ C2H2/3.0/
AC3H4 + H = C3H5                   1.200E+11    0.69    3007.0
C3H3+H=PC3H4                       5.000E+13    0.0     0.0
PC3H4 + H = C3H5                   2.000E+13    0.0     2391.0
PC3H4 + H = C2H2 + CH3             1.300E+05    2.5     1000.0
PC3H4 + CH3 = C3H3 + CH4           2.000E+11    0.0     7700.0
PC3H4 + C2H3 = C3H3 + C2H4         1.000E+12    0.0     7700.0
C3H3+H=C3H2+H2                     5.000E+13    0.0     2980.0
CH + C2H2 = C3H2 + H               1.000E+14    0.0     0.0
C2 + CH3 = C3H2 + H                1.00E+14     0.0     0.0
C3H3=C3H2+H                        5.10E+12     0.0     78407.0
C3H + H2 = C3H2 + H                3.08E+14     0.0     3110.0
C3H + H = C3 + H2                  1.00E+14     0.0     0.0
!************************************************************************
!*******************C4H6system(1,3C4H6)********************************
!************************************************************************
C2H3 + C2H4 = C4H6 + H             3.000E+12    0.0     1000.0
C4H6 + H = C4H5U + H2              3.00E+07     2.0     13000.0
C4H6 + H = C4H5S + H2              3.00E+07     2.0     6000.0
!************************************************************************
!*******************C4H5system*****************************************
!************************************************************************
C4H5S + M = C4H4 + H + M           2.00E+15     0.0     45000.0
H2/1.0/ AR/0.35/ NE/0.35/ C2H2/3.0/
C4H5U + M = C4H4 + H + M           1.00E+14     0.      30000.0
H2/1.0/ AR/0.35/ NE/0.35/ C2H2/3.0/
C4H5U = C2H2 + C2H3                2.00E+14     0.0     44000.0
```

C4H5U + H = C4H4 + H2 3.00E+07 2.0 1000.0
C4H5U + H = C4H5S + H 1.00E+14 0.0 0.0
C2H2 + C2H3 = C4H5S 7.410E+43 -9.56 18270.0
C4H5U = C4H5S 1.310E+39 -8.11 51029.0
C4H5S + H = C2H2 + C2H4 1.000E+13 0.00 0.0
CH2S + AC3H4 = C4H5S + H 1.000E+13 0.00 0.0
C4H5U + H = C2H2 + C2H4 1.000E+13 0.00 0.0
C4H5U + H + M = C4H6 + M 1.000E+15 0.00 0.0
H2/1.0/ AR/0.35/ NE/0.35/ C2H2/3.0/
C4H5S + H + M = C4H6 + M 1.000E+15 0.00 0.0
H2/1.0/ AR/0.35/ NE/0.35/ C2H2/3.0/
C4H6 = C4H5S + H 3.300E+45 -8.95 115934.0
!**********
!**********C4H4,C4H3system**********
!**********
C4H5S + H = C4H4 + H2 3.000E+13 0.00 0.0
C4H4 + M = C4H3U + H + M 1.10E+20 0.0 99340.0
H2/1.0/ AR/0.35/ NE/0.35/ C2H2/3.0/
C4H3S+H = C4H4 3.40E+43 -9.01 12120.0
C4H4+H=C3H2+CH3 5.000E+12 0.00 0.0
C2H + C2H4 = C4H4 + H 1.200E+13 0.00 0.0
C4H4+H = C4H3U+H2 6.65E+05 2.53 12240.0
C4H4+H = C4H3S+H2 3.33E+05 2.53 9240.0
C4H2+H = C4H3U 1.10E+42 -8.72 15300.0
C4H2+H = C4H3S 1.10E+30 -4.92 10800.0
C4H3U = C4H3S 4.10E+43 -9.49 53000.0
C4H3U+H = C4H3S +H 2.50E+20 -1.67 10800.0
C2H2 + C2H2 = C4H3S + H 2.000E+13 0.00 44500.0
!**********
!**********C4H2system,C4Hsystem**********
!**********
C4H4 = C4H2 + H2 1.30E+15 0.00 94720.0
C4H3U +H = C4H2+H2 3.00E+13 0.00 0.0
C4H3S +H = C4H2+H2 6.00E+13 0.00 0.0
C2H2 + C2H = C4H2 + H 3.00E+13 0.00 0.0
C4H2 + M = C4H + H + M 3.500E+17 0.00 80065.0
H2/1.0/ AR/0.35/ NE/0.35/ C2H2/3.0/

C4H + H2 = C4H2 + H	4.10E+05	2.4	200.0
C4H + C4H = C4H2 + C4	1.20E+14	0.00	0.0
C2 + C2H2 = C4H + H	3.00E+13	0.00	0.0
C4H + H = C4 + H2	2.000E+13	0.00	116.5

!**********

9. References

1. G. L. Heller, "Vortex Reactor for Carbon Black Manufacture," US Patent: **US3490869 A**, (1970).
2. J. P. Longwell, "Polycyclic Aromatic Hydrocarbons and Soot from Practical Combustion Systems," in *Soot in Combustion Systems and Its Toxic Properties*, J. Lahaye, and G. Prado, 37–56 (1983).
3. H. Bockhorn, *Soot Formation in Combustion* (Springer-Verlag, Brklin, Heidelberg, 1994).
4. K. H. Homann, and H. G. Wagner, "Some New Aspects of the Mechanism of Carbon Formation in Premixed Flames," *Proc. Combust. Inst.* **11**, 371–379 (1967).
5. M. Frenklach, D. C. Clary, W. C. Gardiner, and S. E. Stein, "Detailed Kinetic Modeling of Soot Formation in Shock Tube Pyrolysis of Acetylene," *Proc. Combust. Inst.* **20**, 887–901 (1984).
6. J. H. Kiefer, and W. A. Von Drasek, "The Mechanism of the Homogeneous Pyrolysis of Acetylene," *Int. J. Chem. Kinet.* **22**, 747–786 (1990).
7. A. V. Krestinin, "Polyyne Model of Soot Formation Process," *Proc. Combust. Inst.* **27**, 1557–1563 (1998).
8. M. Frenklach, and H. Wang, "Detailed Modeling of Soot Particle Nucleation and Growth," *Proc. Combust. Inst.* **23**, 1559–1566 (1990).
9. J. Griesheimer, and K. H. Homann, "Large Molecules, Radicals, Ions, and Small Soot Particles in Fuel-Rich Hydrocarbon Flames. Part II: Aromatic Radicals and Intermediate PAHs in a Premixed Low-Pressure Naphthalene/Oxygen/Argon Flame," *Proc. Combust. Inst.* **27**, 1753–1759 (1998).
10. J. Apple, and H. Bockhorn, "Kinetic Modeling of Soot Formation with Detailed Chemistry and Physics: Laminar Premixed Flames of C_2 Hydrocarbons," *Combust. Flame* **121**, 122–136 (2000).
11. M. Frenklach, "Reaction Mechanism of Soot Formation in Flames," *Phys. Chem. Chem. Phys.* **4**, 2028–2037 (2002).
12. M. Frenklach, T. Yuan, and M. K. Ramachandra, "Soot Formation in Binary Hydrocarbon Mixtures," *Energ. Fuel* **2**, 462–480 (1988).
13. M. Frenklach, and H. Wang, "Aromatics Growth Beyond the First Ring and the Nucleation of Soot Particles," presented in *202nd ACS National Meeting*, 1509– 1517, (Washington, DC, 1991).
14. H. Wang, and M. Frenklach, "A Detailed Kinetic Modeling Study of Aromatics Formation in Laminar Premixed Acetylene and Ethylene Flame," *Combust. Flame* **110**, 173–221 (1997).
15. J. A. Miller, and C. F. Melius, "Kinetic and Thermodynamic Issues in the Formation of Aromatic Compounds in Flames of Aliphatic Fuels," *Combust. Flame* **91**, 21–39 (1992).

16. U. Alkemade, and K. H. Homann, "Formation of C_6H_6 Isomers by Recombination of Propynyl in the System Sodium Vapour/Propynylhalide," *Z. Phys. Chem.* **161**, 19–34 (1989).

17. R. D. Kern, and K. Xie, "Shock Tube Studies of Gas Phase Reactions Preceding the Soot Formation Process," *Prog. Energ. Combust. Sci.* **17**, 191–210 (1991).

18. S. E. Stein, J. A. Walker, M. M. Suryan, and A. Fahr, "A New Path to Benzene in Flames," *Proc. Combust. Symp.* 85–90 (1991).

19. J. Street, and A. Thomas, "Carbon Formation in Pre-mixed Flames," *Fuel* **34**, 4–36 (1955).

20. K. H. Homann, and H. G. Wagner, "Untersuchung des Reaktionsablaufs in fetten Kohlenwasserstoff-Sauerstoff-Flammen," *Ber. Bunsenges. Phys. Chem.* **69**, 20–35 (1965).

21. B. S. Haynes, H. Jander, M. Mätzing, and H. G. Wagner, "The Influence of Gaseous Additives on the Formation of Soot in Premixed Flames," *Proc. Combust. Inst.* **19**, 1379–1385 (1982).

22. I. Glassman, "Soot Formation in Combustion Processes," *Proc. Combust. Inst.* **22**, 295–311 (1988).

23. T. Thienel, "Rußbildung in der Pyrolyse hinter Stoßwellen," PhD Thesis, University of Göttingen, Göttingen, (1995).

24. D. Tanke, "Rußbildung in der Kohlenwasserstoffpyrolyse hinter Stoßwellen," PhD Thesis, University of Göttingen, Göttingen, (1996).

25. A. Emelianov, A. Eremin, E. Gurentsov, H. Jander, and H. G. Wagner, in *Proceeding of a German-Russian Workshop on Reactive Flow, Berlin, Germany* (2002).

26. A. Emelianov, A. Eremin, H. Jander, H. G. Wagner, and C. Borchers, "Spectral and Structural Properties of Carbon Nanoparticle Forming in C_3O_2 and C_2H_2 Pyrolysis behind Shock Waves," *Proc. Combust. Inst.* **29**, 2351–2357 (2002).

27. P. L. Houston, *Chemical Kinetics and Reaction Dynamics* (McGraw-Hill, New York, 2001).

28. J. Warnatz, U. Maas, and R. W. Dibble, *Verbrennung* (Springer, Heidelberg, 2001).

29. O. K. Rice, and H. C. Ramsperger, "Theories of Unimolecular Gas Reactions at Low Pressures," *J. Am. Chem. Soc.* **49**, 1617–1629 (1927).

30. L. S. Kassel, "Studies in Homogeneous Gas Reactions I," *J. Phys. Chem.* **32**, 225–242 (1928).

31. H. Eyring, "The Activated Complex in Chemical Reactions," *J. Chem. Kinet.* **3**, 107–115 (1935).

32. M. Quack, and J. Troe, "Specific Rate Constants of Unimolecular Processes II. Adiabatic Channel Model," *Ber. Bunsenges. Phys. Chem.* **78**, 240–252 (1974).

33. J. Troe, "Specific Rate Constants k(E,J) for Unimolecular Bond Fissions," *J. Chem. Phys.* **79**, 6017–6029 (1983).

34. F. A. Lindemann, "Discussion on “The Radiation Theory of Chemical Action”," *Trans. Faraday Soc.* **17**, 598–606 (1922).

35. P. J. Robinson, and K. A. Holbrook, *Unimolecular Reactions* (Wiley-Interscience, New York, 1972).

36. P. Atkins, and J. di Paula, *Atkins' Physical Chemistry* (Oxford University Press, Oxford, New York, 2010).

37. J. Warnatz, "The Mechanism of High Temperature Combustion of Propane and Butane," *Combust. Sci. Technol.* **34**, 177–200 (1983).

38. W. C. Gardiner, *Combustion Chemistry* (Springer-Verlag, Heidelberg, 1984).

39. R. Starke, and P. Roth, "Soot Particle Sizing by LII During Shock Tube Pyrolysis of C_6H_6," *Combust. Flame* **127**, 2278–2285 (2002).

40. A. V. Emelianov, A. V. Eremin, A. A. Makeich, H. Jander, H. G. Wagner, and R. Starke, "Heat Release of Carbon Particle Formation from Hydrogen Free Precursors behind Shock Waves," *Proc. Combust. Inst.* **31**, 649–656 (2007).

41. A. Emelianov, A. Eremin, and H. Jander, "Experimental Study of Carbon Particle Charging at Shock Wave Pyrolysis of C_3O_2," *Proc. Combust. Inst.* **32**, 721–728 (2009).

42. G. Ben-Dor, O. Igra, and T. Elperin, *Handbook on Shock Waves (3 Volumes)* (Academic Press, Boston, 2001).

43. A. Lifshitz, *Shock waves in chemistry* (Marcel Dekker Inc., New York, 1981).

44. K. A. Bhaskaran, and P. Roth, "The shock tube as wave reactor for kinetic studies and material systems," *Prog. Energ. Combust.* **28**, 151–192 (2002).

45. D. L. Baulch, C. J. Cobos, R. A. Cox, C. Esser, P. Frank, T. Just, J. A. Kerr, M. J. Pilling, J. Troe, R. W. Walker, and J. Warnatz, "Evaluated Kinetic Data for Combustion Modelling," *J. Phys. Chem. Ref. Data* **21**, 411–734 (1992).

46. W. Tsang, and R. F. Hampson, "Chemical Kinetic Data Base for Combustion Chemistry. Part I. Methane and Related Compounds " *J. Phys. Chem. Ref. Data* **15** (1986).

47. E. Rathakrishnan, *Applied Gas Dynamics* (John Wiley & Sons (Asia) Pte Ltd, Singapore, 2010).

48. J. B. Zel'dovich, and Y. P. Raizer, *Physics of Shock Waves and High-Temperature Hydrodynamic Phenomena* (Academic Press, New York, 1966).

49. A. Abdali, "Gas-phase Synthesis of Silica Nanoparticles: Reaction Kinetics, Synthesis and Characterization," Phd Thesis, University of Duisburg-Essen, Duisburg, (2014).

50. W. J. M. Rankine, "On the Thermodynamic Theory of Waves of Finite Longitudinal Disturbance " *Phil. Trans. R. Soc. Lond.* **160**, 277–288 (1870).

51. P. H. Hugoniot, "Sur la Propagation du Mouvement dans les Corps et Spécialement dans les Gaz Parfaits (première partie)," *J. Ecole Polytech.* **57**, 3–97 (1887).

52. P. H. Hugoniot, "Sur la Propagation du Mouvement dans les Corps et Spécialement dans les Gaz Parfaits (deuxième partie)," *J. Ecole Polytech.* **58**, 1–125 (1889).

53. H. Kienitz, *Massenspektrometrie* (Verlag Chemie GmbH, Weinheim/Bergstr., 1968).

54. E. Schröder, *Massenspektrometrie:Begriffe und Definitionen* (Heidelberger Taschenbücher, Berlin, 1991).

55. E. de Hoffmann, and V. Stroobant, *Mass Spectrometry Principles and Applications* (John Wiley and Sons, Chichester, 2007).

56. R. Ekman, *Mass Spectrometry:Instrumentation, Interpretation, and Applications* (Wiley, Hoboken, NJ, 2009).

57. H. Budzikiewicz, and M. Schäfer, *Massenspektrometrie : eine Einführung* (Wiley-VCH, Weinheim, 2012).

58. J. H. Gross, *Massenspektrometrie : ein Lehrbuch* (Springer Spektrum, Berlin, 2013).

59. A. J. Dempster, "A New Method of Positive Ray Analysis," *Phys. Rev.* **11**, 316–325 (1918).

60. T. W. Bentley, and R. A. W. Johnstone, "Mechanism and Structure in Mass Spectrometry: A Comparison with Other Chemical Processes," *Adv. Phys. Org. Chem.* **8**, 151–269 (1970).

61. W. E. Stephens, "A Pulsed Mass Spectrometer with Time Dispersion," *Phys. Rev.* **69**, 691–691 (1946).

62. W. C. Wiley, and I. H. McLaren, "Time-of-Flight Mass Spectrometer with Improved Resolution," *Rev. Sci. Instrum.* **26**, 1150–1157 (1955).

63. R. S. Tranter, B. R. Giri, and J. H. Kiefer, "Shock Tube/Time-of-Flight Mass Spectrometer for High Temperature Kinetic Studies," *Rev. Sci. Instrum.* **78**, 034101–034111 (2007).

64. B. R. Giri, and R. S. Tranter, "Dissociation of 1,1,1-Trifluoroethane Behind Reflected Shock Waves: Shock Tube/Time-of-Flight Mass Spectrometry Experiments," *J. Phys. Chem. A* **111**, 1585–1592 (2007).

65. S. H. Dürrstein, M. Olzmann, J. Aguilera-Iparraguirre, R. Barthel, and W. Klopper, "The phenyl + phenyl reaction as pathway to benzynes: An experimental and theoretical study," *Chem. Phys. Lett.* **513**, 20–26 (2011).

66. B. A. Mamyrin, V. I. Karataev, D. V. Shmikk, and V. A. Zagulin, "The Mass-Reflectron, a New Nonmagnetic Time-of-Flight Mass Spectrometer with High Resolution," *Soviet Phys. (J. Exp. Theor. Phys.)* **37**, 45–48 (1973).

67. R. J. Cotter, "Time-of-Flight Mass Spectrometry for the Structural Analysis of Biological Molecules," *Anal. Chem.* **64**, 1027A–1039A (1992).

68. G. J. Williams, and R. G. Wilkins, "An Investigation of the Chemical Structure of Perchloric Acid Flames, Part I—The Molecular Beam Sampling Apparatus," *Combust. Flame* **21**, 325–337 (1973).

69. D. J. Hucknall, and A. Morris, *Vacuum Technology Calculations in Chemistry* (The Royal Society of Chemistry, Cambridge, UK, 2003).

70. P. P. Wegener, *Molecular Beams and Low Density Gas Dynamics* (Marcel Decker Inc., New York, 1974).

71. G. Scoles, *Atomic and Molecular Beam Methods* (Oxford University Press, New York, 1988).

72. G. E. McMichael, and J. B. French, "Electron Beam Studies of Skimmer Interaction in a Free Jet," *Phys. Fluids* **9**, 1419–1420 (1966).

73. T. Dorfmüller, M. Faubel, P. Fischer, H. Grubmüller, H. Haberland, G. Hauck, G. Heppke, S. Hess, K. Kleinermanns, M. Kröger, K. Lüders, U. Riedel, C. Schulz, S. Seeger, H.-H. Strehblow, F. Träger, H. Tschesche, J. Uhlenbusch, J. Warantz, and J. Wolfrum, *Lehrbuch der Experimentalphysik Band 5 Gase, Nanosysteme, Flüssigkeiten* (Walter de Gruyter, Berlin, New York, 2006).

74. M. Knudsen, "Die Molekularströmung der Gase durch Offnungen und die Effusion," *Ann. Phys.* **333**, 999–1016 (1909).

75. C. Jousten, *Wutz Handbuch Vakuumtechnik* (Vieweg, Wiesbaden, 2010).

76. L. Davies, "The Interaction of the Reflected Shock with the Boundary Layer in a Shock Tube and its Influence on the Duration of Hot Flow in the Reflected-Shock Tunnel," (British Aeronautical Research Council, Londodn, 1967).

77. H. Ashkenas, and F. S. Sherman, "The Structure and Utilization of Supersonic Free Jets in Low Density Wind Tunnels," presented at the *Fourth International Symposium on Rarefied Gas Dynamics*, Toronto, 84–105, (J. H. deLeeuwe Academic, New York, 1966).

78. J. N. Bradley, and G. B. Kistiakowsky, "Shock Wave Studies by Mass Spectrometry. I. Thermal Decomposition of Nitrous Oxide," *J. Chem. Phys.* **35**, 256–263 (1961).

79. J. E. Dove, and D. M. Moulton, "Shock Wave Studies by Mass Spectrometry. III. Description of Apparatus; Data on theOxidation of Acetylene and of Methane," *Proc. Roy. Soc. Lond. A. Mat.* **283**, 216–228 (1965).

80. A. P. Modica, "Kinetics of the Nitrous Oxide Decomposition by Mass Spectrometry. A Study to Evaluate Gas-Sampling Methods behind Reflected Shock Waves," *J. Phys. Chem.* **69**, 2111–2116 (1965).

81. R. D. Kern, H. J. Singh, and Q. Jhang, *Handbook of Shock Waves* (Academic Press, New York, 1965).

82. I. Krizancic, M. Haluk, S. H. Cho, and O. Trass, "Shock Tube Coupled to the Time-of-Flight Mass Spectrometer via a Molecular Beam Sampling System," *Rev. Sci. Instrum.* **50**, 909–915 (1979).

83. E. C. Voldner, and O. Trass, "Evaluation of Thermal Boundary Layer Interaction in Shock Tube Sampling For Kinetic Studies," *J. Chem. Phys.* **73**, 1601–1611 (1980).

84. H. W. Liepmann, "Gaskinetics and Gasdynamics of Orifice Flow," *J. Fluid Mech.* **10**, 65–79 (1960).

85. W. M. A. Niessen, *Liquid Chromatography: Mass Spectrometry* (CRC Press, Boca Raton, Florida, 1999).

86. J. N. Bradley, and G. B. Kistiakowsky, "Shock Wave Studies by Mass Spectrometry. II. Polymerization and Oxidation of Acetylene," *J. Chem. Phys.* **35**, 264–270 (1961).

87. J. N. Bradley, "Shock-wave decomposition of nitroparaffins. Part 1. Mass-Spectrometric Study of Nitromethane Decomposition," *Trans. Faraday Soc.*, 1750–1756 (1961).

88. R. W. Diesen, and W. J. Felmlee, "Mass Spectral Studies of Kinetics behind Shock Waves. I. Thermal Dissociation of Chlorine," *J. Chem. Phys.* **39**, 2115–2120 (1963).

89. R. W. Diesen, "Mass Spectral Studies of Kinetics behind Shock Waves. II. Thermal Decomposition of Hydrazine," *J. Chem. Phys.* **39**, 2121–2128 (1963).

90. R. W. Diesen, "MassSpectral Studies of Kinetics behind Shock Waves. III. Thermal Dissociation of Fluorine," *J. Chem. Phys.* **44**, 3662–3666 (1966).

91. H. J. Singh, and R. D. Kern, "Pyrolysis of Benzene behind Reflected Shock Waves," *Combust. Flame* **54**, 49–59 (1983).

92. C. H. Wu, H. J. Singh, and R. D. Kern, "Pyrolysis of Acetylene behind Reflected Shock Waves," *Int. J. Chem. Kinet.* **19**, 975–996 (1987).

93. R. D. Kern, H. J. Singh, and C. H. Wu, "Thermal Decomposition of 1,2 Butadiene," *Int. J. Chem. Kinet.* **20**, 731–747 (1988).

94. J. H. Kiefer, P. S. Mudipalli, S. S. Sidhu, R. D. Kern, B. S. Jursic, K. Xie, and H. Chen, "Unimolecular Dissociation in Allene and Propyne: The Effect of Isomerization on the Low-Pressure Rate," *J. Phys. Chem. A* **101**, 4057–4071 (1997).

95. R. S. Tranter, and B. R. Giri, "A Diaphragmless Shock Tube for High Temperature Kinetic Studies," *Rev. Sci. Inst.* **79**, 094101–094106 (2008).

96. B. R. Giri, J. H. Kiefer, H. Xu, S. J. Klippenstein, and R. S. Tranter, "An Experimental and Theoretical High Temperature Kinetic Study of the Thermal Unimolecular Dissociation of Fluoroethane," *Phys. Chem. Chem. Phys.* **10**, (2008).

97. T. Bentz, "Stoßwellenuntersuchungen zur Reaktionskinetik ungesättigter und teiloxidierter Kohlenwassestoffe," (Karlsruhe Institute of Technology (KIT), 2008).

98. S. H. Dürrstein, "Untersuchung komplexer Reaktionsmechanismen durch zeitaufgelöste Massenspektrometrie hinter reflektrierten Stoßwellen," PhD Thesis, Karlsruhe Institute of Technology (KIT), Karlsruhe, (2009).

99. P. R. Ryason, "Shock TubeTOF Mass Spectrometer Apparatus with Cryosorption Pumping," *Rev. Sci. Instrum.* **38**, 607–611 (1967).

100. H. T. Nagamatsu, B. C. Graber, and R. E. Sheer, "Roughness, Bluntness, and Angle-of-Attack Effects on Hypersonic Boundary-Layer Transition," *J. Fluid Mech.* **24**, 1–31 (1966).

101. I. D. Gay, R. D. Kern, G. B. Kistiakowsky, and H. Niki, "Pyrolysis of Ethylene in Shock Waves," *J. Chem. Phys.* **45**, 2371–2377 (1966).

102. R. Rajoub, B. G. Lindsay, and R. F. Stebbings, "Determination of the Absolute Partial and Total Cross Sections for Electron-Impact Ionization of the Rare Gases," *Phys. Rev. A* **65**, 042711–042718, (2002).

103. R. J. Kee, F. M. Rupley, J. A. Miller, M. E. Coltrin, J. F. Grcar, E. Meeks, H. K. Moffat, A. E. Lutz, G. Dixon-Lewis, M. D. Smooke, J. Warnatz, G. H. Evans, R. S. Larson, R. E. Mitchell, L. R. Petzold, W. C. Reynolds, M. Carcotsios, W. E. Stewart, P. Glarborg, C. Wang, and O. Adigun, "CHEMKIN," (Reaction Design Inc., San Diego, CA, 1990).

104. A. Y. Starikovsky, T. Thienel, H. G. Wagner, and I. Zaslonko, "Soot formation in the pyrolysis of halogenated hydrocarbons. Part I, Binary Mixtures of Carbon Tetrachloride with Hhydrogen and Iron Pentacarbonyl," *Ber. Bunsenges. Phys. Chem.* **102**, 1815–1822 (1998).

105. R. Starke, B. Cock, P. Roth, A. Eremin, E. Gurentsov, V. Shumova, and V. Ziborov, "Shock Wave Induced Carbon Particle Formation From CCl_4 and C_3O_2 Observed by Laser Extinction and by Laser-Induced Incandescence (LII)," *Combust. Flame* **135**, 77–85 (2003).

106. I. Zhil'tsova, I. Zaslonko, Y. Karasevich, and H. G. Wagner, "Kinetics of Soot Formation in Tetrachloromethane Pyrolysis," *Kinet. Catal.* **41**, 366–376 (2000).

107. H. G. Wagner, P. A. Vlasov, K. J. Dörge, A. Eremin, I. S. Zaslonko, and D. Tanke, "Kinetics of carbon cluster formation during pyrolysis of C_3O_2," *Kinet. Catal.* **42**, 583–593 (2001).

108. G. Friedrichs, and H. G. Wagner, "Investigation of the Thermal Decay of Carbon Suboxide," *Z. Phys. Chem.* **203**, 1–14 (1998).

109. M. Frenklach, J. P. Hsu, D. L. Miller, and R. A. Matula, "Shock-Tube Pyrolysis of Chlorinated Hydrocarbons: Formation of Soot," *Combust. Flame* **64**, 141–155 (1986).

110. M. Frenklach, "Production of Polycyclic Aromatic Hydrocarbons in Chlorine Containing Environments," *Combust. Sci. Technol.* **74**, 283–296 (1990).

111. D. A. Tirey, P. H. Taylor, J. Kasner, and B. Dellinger, "Gas Phase Formation of Chlorinated Aromatic Compounds from the Pyrolysis of Tetrachloroethylene," *Combust. Sci. Technol.* **74**, 137–157 (1990).

112. J. Z. Wen, C. F. Goldsmith, R. W. Ashcraft, and W. H. Green, "Detailed Kinetic Modeling of Iron Nanoparticle Synthesis from the Decomposition of $Fe(CO)_5$," *J. Phys. Chem. C* **111**, 5677–5688 (2007).

113. J. B. Zel'dovich, "Theory of Formation of a New Phase," *Acta Physicochim URSS* **18**, 1–22 (1943).

114. H. Tachikawa, "Dynamics of Electron Attachment and Ionization Processes in the CCl_4 Molecule: An ab Initio MO and Direct Dynamics Study," *J. Phys. Chem. A* **101**, 7454–7459 (1997).

115. B. G. Lindsay, K. F. McDonald, W. S. Yu, R. F. Stebbings, and F. B. Yousif, "Electron-Impact Ionization of CCl_4 and CCl_2F_2," *J. Chem. Phys.* **121**, 1350–1356 (2004).

116. M. Aghsaee, A. V. Drakon, A. Eremin, S. H. Dürrstein, H. Böhm, H. Somnitz, M. Fikri, and C. Schulz, "Experimental Investigation and Modeling of the Kinetics of CCl_4 Pyrolysis behind Reflected Shock Waves Using High-Repetition-Rate Time-of-Flight Mass Spectrometry," *Phys. Chem. Chem. Phys.* **15**, 2821–2828 (2013).

117. S. S. Kumaran, M.-C. Su, K. P. Lim, J. V. Michael, S. J. Klippenstein, J. DiFelice, P. S. Mudipalli, J. H. Kiefer, D. A. Dixon, and K. A. Peterson, "Experiments and Theory on the Thermal Decomposition of $CHCl_3$ and the Reactions of CCl_2," *J. Phys. Chem. A* **101**, 8653–8661 (1997).

118. T. Kovacs, T. Turanyi, K. Foeglein, and J. Szepvoelgyi, "Kinetic Modeling of the Decomposition of Carbon Tetrachloride in Thermal Plasma," *Plasma Chem. and Plasma Process.* **25**, 109–119 (2005).

119. Y.-S. Won, "Thermal Stability and Reaction Mechanism of Chloromethanes in Excess Hydrogen Atmosphere," *J. Ind. Eng. Chem.* **13**, 400–405 (2007).

120. Y.-S. Won, and J. W. Bozzelli, "Chloroform Pyrolysis: Experiment and Detailed Reaction Model," *Combust. Sci. Technol.* **85**, 345–373 (1992).

121. B. C. Garrett, and D. G. Truhlar, "Generalized Transition State Theory. Canonical Variational Calculations Using the Bond Energy-Bond Order Method for Bimolecular Reactions of Combustion Products," *J. Am. Chem. Soc.* **101**, 5207–5217 (1979).

122. S. Dusoleil, P. Goldfinger, A. M. Mahieu-Van der Auwera, G. Martens, and D. Van der Auwera, "Elementary Rate Constants in Atomic Chlorination Reactions, Part 1. Expefumences in Intermittent Light," *Trans. Faraday Soc.* **57**, 2197–2209 (1961).

123. G. Huybrechts, I. Theys, and B. Van Meele, "Pyrolysis of Hexachloroethane in the Gas Phase: Computer Aided Kinetic Study," *Int. J. Chem. Kinet.* **28**, 755–761 (1996).

124. S. S. Kumaran, M.-C. Su, K. P. Lim, J. V. Michael, A. F. Wagner, and L. B. Harding, "*Ab Initio* Calculations and Three Different Applications of Unimolecular Rate Theory for the Dissociations of CCl_4, $CFCl_3$, CF_2Cl_2, and CF_3Cl," *J. Phys. Chem.* **100**, 7541–7549 (1996).

125. J. Warnatz, F. Behrendt, J. Sojka, H. G. Wagner, I. S. Zaslonko, P. A. Vlasov, Y. K. Karasevich, V. N. Smirnov, and A. Y. Starikovsky, *Computer Modeling of Iron Cluster Growth and Decomposition behind Shock Waves in: Modeling of Chemical Reaction Systems*, IWR, University of Heidelberg, Heidelberg, (1997).

126. J. Sojka, "Simulation der Rußbildung unter homogenen Verbrennungsbedingungen," PhD Thesis, University of Heidelberg, Heidelberg, (2001).

127. D. L. Baulch, J. Duxbury, S. J. Grant, and D. C. Montague,"Evaluated Kinetic Data for High-Temperature Reactions, Vol 4, Homogeneous Gas-Phase Reactions of Halogen- and Cyanide-Containing Species," *J. Phys. Chem. Ref. Data* **10**, 1–721 (1981).

128. M. W. Chase, *NIST-JANAF thermochemical tables* (American Chemical Society, Washington, DC, 1998).

129. J. V. Michael, K. P. Lim, S. S. Kumaran, and J. H. Kiefer, "Thermal Decomposition of Carbon Tetrachloride," *J. Phys. Chem.* **97**, 1914–1919 (1993).

130. A. Burcat, and B. McBride, "Technion Report No. TAE 804," (Haifa, 1997).

131. M. Aghsaee, H. Bohm, S. H. Durrstein, M. Fikri, and C. Schulz, "Experimental and Modeling Study of Carbon Suboxide Decomposition behind Reflected Shock Waves," *Phys. Chem. Chem. Phys.* **14**, 1246–1252 (2012).

132. A. Emelianov, A. Eremin, E. Gurentsov, H. Jander, and H. G. Wagner, Abstracts of work-in-progress poster presentation *29th Int. Symp. Combust.*, 32 (2002).

133. A. Katzakov, and M. Frenklach, "Dynamic Modeling of Soot Particle Coagulation and Aggregation: Implementation With the Method of Moments and Application to High-Pressure Laminar Premixed Flames," *Combust. Flame* **114**, 484–501 (1998).

134. N. Demchuk, and H. D. Gesser, "Reaction of Hydrogen Atoms with Carbon Suboxide," *Can. J. Chem.* **49**, 803–806 (1971).

135. K. J. Dörge, D. Tanke, and H. G. Wagner, "Particle Formation in Carbon Suboxide Pyrolysis behind Shock Waves," *Z. Phys. Chem.* **212**, 219–229 (1999).

136. J. Sojka, J. Warantz, P. A. Vlasov, and I. S. Zaslonko, "Kinetic Modeling of Carbon Suboxide Thermal Decomposition and Formation of Soot-Like Particles Behind Shock Waves," *Combust. Sci. Technol.* **158**, 439–460 (2000).

137. J. Z. Wen, M. J. Thomson, and M. F. Lightstone, "Numerical Study of Carbonaceous Nanoparticle Formation Behind Shock Waves," *Combust. Theor. Model.* **10**, 257–272 (2006).

138. P. Deuflhard, and M. Wulkow, "Computational Treatment of Polyreaction Kinetics by Orthogonal Polynomials of a Discrete Variable," *IMPACT Comp. Sci. Eng.* **1**, 269–301 (1989).

139. A. Emelianov, A. Eremin, E. Gurentsov, A. Makeich, H. Jander, H. G. H. G. Wagner, P. Roth, and R. Starke, "Time and Temperature Dependence of Carbon Particle Growth in Various Shock Wave Pyrolysis Processes," *Proc. Combust. Inst.* **30**, 1433–1440 (2005).

140. H. G. Wagner, A. V. Emelianov, A. V. Eremin, and H. Jander, "Comparison of Properties of Carbon Particles Formed by Pyrolysis of C_3O_2 and C_2H_2 Behind Shock Waves," *Kinet. Catal.* **44**, 463–470 (2003).

141. A. Stock, and H. Stolzenberg, "Über die Darstellung des Kohlensuboxydes aus Malonsäure und Phosphorpentoxyd," *Ber. Dtsch. Chem. Ges.* **50**, 498–502 (1917).

142. A. Klemenc, *Die Behandlung und Reindarstellung von Gasen* (Springer, Vienna, 1948).

143. H. Böhm, A. Emelianov, A. Eremin, C. Schulz, and H. Jander, "On the Effect of Molecular and Hydrocarbon-Bonded Hydrogen on Carbon Particle Formation in C_3O_2 Pyrolysis behind Shock Waves," *Combust. Flame* **159**, 932–939 (2012).

144. G. Friedrichs, "Thermischer Zerfall und Photolyse von Kohlensuboxid," PhD Thesis, University of Göttingen, Göttingen, (1996).

145. R. J. Kee, F. M. Rupley, and J. A. Miller, *The Chemkin Thermodynamic Data Base, SAND87-8215B* (Sandia, Livermore, CA, 1990).

146. J. M. L. Martin, J. P. François, and R. Gijbels, "On the Heat of Formation of C_5 and Higher Carbon Clusters," *J. Chem. Phys.* **95**, 9420–9421 (1991).

147. P. Frank, and T. H. Just, "High Temperature Thermal Decomposition of Acetylene and Diacetylene at Low Relative Concentrations," *Combust. Flame* **38**, 231–248 (1980).

148. M. P. Ruiz, A. Callejas, A. Millera, M. U. Alzueta, and R. Bilbao, "Soot Formation from C_2H_2 and C_2H_4 Pyrolysis at Different Temperatures," *J. Anal. Appl. Pyrol.* **79**, 244–251 (2007).

149. M. P. Ruiz, R. Guzmán de Villoria, A. Millera, M. U. Alzueta, and R. Bilbao, "Influence of the Temperature on the Properties of the Soot Formed from C_2H_2 Pyrolysis," *Chem. Eng. J.* **127**, 1–9 (2007).

150. M. P. Ruiz, R. Guzmán de Villoria, A. Millera, M. U. Alzueta, and R. Bilbao, "Influence of Different Operation Conditions on Soot Formation from C_2H_2 Pyrolysis," *Ind. Eng. Chem. Res.* **46**, 7550–7560 (2007).

151. A. Eremin, E. Gurentsov, and E. Mikheyeva, "Experimental Study of Molecular Hydrogen Influence on Carbon Particle Growth in Acetylene Pyrolysis behind Shock Waves," *Combust. Flame* **159**, 3607–3615 (2012).

152. Y.-K. Kim, K. K. Irikura, M. E. Rudd, M. A. Ali, P. M. Stone, J. Chang, J. S. Coursey, R. A. Dragoset, A. R. Kishore, K. J. Olsen, A. M. Sansonetti, G. G. Wiersma, D. S. Zucker, and M. A. Zucker, "Electron-Impact Ionization Cross Section for Ionization and Excitation Database (version 3.0), National Institute of Standards and Technology, Gaithersburg, MD., (2004).

153. M. Aghsaee, S. H. Dürrstein, J. Herzler, H. Böhm, M. Fikri, and C. Schulz, "Influence of Molecular Hydrogen on Acetylene Pyrolysis: Experiment and Modeling," *Combust. Flame* **161**, 2263–2269 (2014).

154. V. Brinzea, M. Mitu, D. Razus, and D. Oancea, "Propane Oxidation in Flames," *Rev. Roum. Chim.* **55**, 55–61 (2010).

155. G. Baldea, L. Maier, M. Hartmann, U. Riedel, and O. Deutschmann, "Automated Mechanism Generation and Kinetic Modeling for Partial Oxidation of Iso-Octane," in *Proceedings of the 4th European Combustion Meeting* (Vienna, Austria, 2009).

156. C. I. Heghes, N. Morgan, U. Riedel, J. Warnatz, R. Quiceno, and R. Cracknell, "Development and Validation of a Gasoline Fuel Kinetic Mechanism," SAE **2009-1-0934** (2009).

157. C. I. Heghes, "C1-C4 Hydrocarbon Oxidation Mechanism.," PhD Thesis, University of Heidelberg, Heidelberg, (2006).

158. H. Böhm, M. Braun-Unkhoff, and P. Frank, "Investigations on Initial Soot Formation at High Pressures," *Prog. Comput. Fluid Dynam.* **3**, 145–150 (2003).

159. H. Böhm, and H. Jander, "PAH Formation in Acetylene Benzene Pyrolysis," *Phys. Chem. Chem. Phys.* **1**, 3775–3781 (1999).

160. I. Naydenova, "Soot Formation Modeling during Hydrocarbon Pyrolysis and Oxidation behind Shock Waves," PhD Thesis, University of Heidelberg, Heidelberg, (2007).

161. X. Gu, Y. Guo, F. Zhang, M. Mebel, and R. I. Kaiser, "A Crossed Molecular Beams Study of the Reaction of Dicarbon Molecules with Benzene," *Chem. Phys. Lett.* **436**, 7–14 (2007).

162. K. H. Becker, B. Donner, C. M. Dinis, H. Geiger, F. Schmidt, and P. Wiesen, "Kinetics of the $C_2(a^3II_u)$ Radical Reacting with Selected Molecules and Atoms," *Z. Phys. Chem.* **214**, 503–517 (2000).

163. F. Cozzi, and A. Coghe, "Behavior of Hydrogen-Enriched Non-Premixed Swirled Natural Gas Flame," *Int. J. Hydrogen Energ.* **31**, 669–677 (2006).

164. V. Chernov, M. J. Thomson, S. B. Dworkin, N. A. Slavinskaya, and U. Riedel, "Soot Formation with C_1 and C_2 Fuels Using an Improved Chemical Mechanism for PAH Growth," *Combust. Flame* **161**, 592–601 (2014).

165. E. Ranzi, "Hierarchical and Comparative Kinetic Modeling of Laminar Flame Speeds of Hydrocarbon and Oxygenated Fuels," *Prog. Energ. Combust.* **38**, 592–601 (2012).

166. M. Braun-Unkhoff, A. Kurz, and P. Frank, "High Temperature Pyrolysis of Vinylacetylene," in *Proceedings of the 17th International Symposium on Shock Waves*, 493–498 (1989).